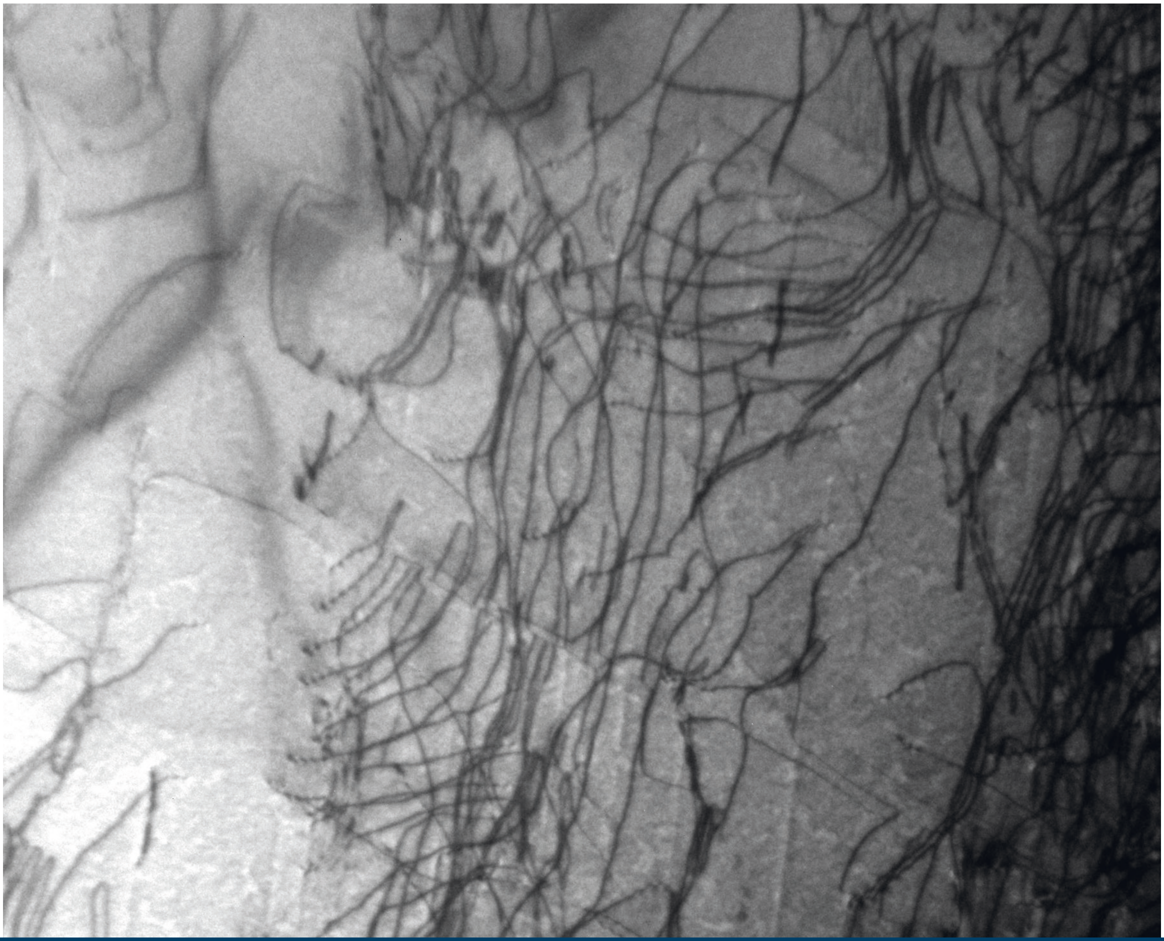

Characteristics of plastically deformed *fcc* and *bcc* High-Entropy Alloys

Tim Meenen

Information
Band / Volume 111
ISBN 978-3-95806-820-9

Mitglied der Helmholtz-Gemeinschaft

JÜLICH
Forschungszentrum

Schriften des Forschungszentrums Jülich
Reihe Information / Information Band / Volume 111

Forschungszentrum Jülich GmbH
Ernst Ruska-Centrum für Mikroskopie und Spektroskopie mit Elektronen (ER-C)
Physik Nanoskaliger Systeme (ER-C-1)

Characteristics of plastically deformed *fcc* and *bcc* High-Entropy Alloys

Tim Meenen

Schriften des Forschungszentrums Jülich
Reihe Information / Information Band / Volume 111

ISSN 1866-1777 ISBN 978-3-95806-820-9

Bibliografische Information der Deutschen Nationalbibliothek.
Die Deutsche Nationalbibliothek verzeichnet diese Publikation in der
Deutschen Nationalbibliografie; detaillierte Bibliografische Daten
sind im Internet über http://dnb.d-nb.de abrufbar.

Herausgeber und Vertrieb: Forschungszentrum Jülich GmbH
Zentralbibliothek, Verlag
52425 Jülich
Tel.: +49 2461 61-5368
Fax: +49 2461 61-6103
zb-publikation@fz-juelich.de
www.fz-juelich.de/zb

Umschlaggestaltung: Grafische Medien, Forschungszentrum Jülich GmbH

Druck: Grafische Medien, Forschungszentrum Jülich GmbH

Schriften des Forschungszentrums Jülich
Reihe Information / Information, Band / Volume 111

D 82 (Diss. RWTH Aachen University, 2025)

ISSN 1866-1777
ISBN 978-3-95806-820-9

Abstract

High-Entropy Alloys (HEAs) are alloys with at least four principal elements in (near-)equiatomic proportion, which crystallize on simple crystal lattices, such as face-centred cubic, body-centred cubic, or hexagonal close-packed. These alloys have a stoichiometrically random distribution of constituent elements on all available lattice sites, and they form single-phase solid solutions with perfect topological order and complete chemical disorder. The structural simplicity of HEAs makes them well-suited to address fundamental scientific issues related to structure-property relationships.

In this work, the plasticity of two HEAs, face-centred cubic CrMnFeCoNi and body-centred cubic TiVZrNbHf, was investigated through uniaxial deformation experiments on single crystalline CrMnFeCoNi and polycrystalline TiVZrNbHf samples. The thermodynamic activation parameters of the deformation process were determined, and microstructural investigations were carried out on both alloys using transmission electron microscopy. These investigations revealed the underlying deformation mechanisms of both alloys. Although both alloys deform through the slip of dislocations on characteristic slip systems, CrMnFeCoNi behaves like a conventional face-centred cubic alloy with exceptional strength, while TiVZrNbHf exhibits a yield stress anomaly that is unique to HEAs.

Kurzfassung

High-Entropy Alloys (HEAs) bestehen aus mindestens vier Elementen in (nahezu) equiatomarem Verhältnis, die auf einfachen Kristallgittern kristallisieren, wie z. B. kubisch-flächenzentriert, kubisch-raumzentriert oder hexagonal dicht gepackt. Diese Legierungen weisen eine stöchiometrisch zufällige Verteilung der Elemente auf alle verfügbaren Gitterplätze auf und bilden einphasige Mischkristalle mit perfekter topologischer Ordnung und vollständiger chemischer Unordnung. Die strukturelle Simplizität von HEAs macht sie gut geeignet, um fundamentale Fragen im Zusammenhang mit Struktur-Eigenschafts-Beziehungen zu untersuchen.

In dieser Arbeit wurde die Plastizität von zwei HEAs, kubisch flächenzentriertes CrMnFeCoNi und kubisch raumzentriertes TiVZrNbHf, durch einachsige Verformungsexperimente an einkristallinen CrMnFeCoNi- und polykristallinen TiVZrNbHf-Proben untersucht. Die thermodynamischen Aktivierungsparameter des Verformungsprozesses wurden bestimmt, und an beiden Legierungen wurden mikrostrukturelle Untersuchungen mittels Transmissionselektronenmikroskopie durchgeführt. Diese Untersuchungen enthüllten die zugrundeliegenden Verformungsmechanismen der beiden Legierungen. Obwohl sich beide Legierungen durch das Gleiten von Versetzungen auf charakteristischen Gleitsystemen verformen, verhält sich CrMnFeCoNi wie eine herkömmliche kubisch-flächenzentrierte Legierung mit außergewöhnlicher Festigkeit, während TiVZrNbHf eine Anomalie der Fließspannung aufweist, die einzigartig für HEAs ist.

Table of contents

Chapter 1

Introduction

Since the dawn of civilisation, mankind has sought to harness the natural materials that surround it for their most advantageous properties, leading to continuous development. Early humans utilised materials such as stone, wood, leather, bone and native metals like gold, silver, and copper. With the progression of the Bronze, Iron, and Steel ages, techniques for extracting copper, tin, lead, mercury, and iron from their respective ores were developed alongside the technology to produce these materials in large quantities. While pure metals already had advantages over other natural materials, alloying, for example, copper with lead or tin and iron with carbon from combustion fuels, created superior alloys such as bronze, cast iron, and steel. These alloys, with their beneficial combination of strength and toughness compared to ancient materials like ceramics and natural polymers, became attractive for use in daily life, transportation, construction, and weaponry.

Until the first industrial revolution the discovery of new elements and metals was difficult due to poor deposits or difficulties in reduction or extraction. Newly developed technologies supported the discovery and production of new elements, and new alloys were continuously developed and applied for general and specialised purposes. Several alloy systems, each based on one principal element, were introduced over time, some of which are meticulously tailored to specific applications [1]. Through the times, alloying usually followed the principle of adding small amounts of secondary elements to a primary element to confer desirable properties to a material. This principle exists for a good reason, as already early experiments show that alloys of multiple principal elements have diverse but rarely desirable properties [2, 3]. Even in modern times, multicomponent alloys with several principal elements were rarely investigated due to the information available from binary and ternary phase diagrams [4]. Most of these phase diagrams show intermetallic compounds, ordered structures with compositions in stoichiometric or near-stoichiometric ratio, or intermediate phases, which are compound-type solid solutions with a relatively wide composition range, also called intermetallic phases [5]. The Al-Cu-Zn alloy system, which comprises more than 20 equilibrium intermetallic compounds or intermediate phases [6], exemplifies the dilemma. Given the existing knowledge, the exploration of multicomponent alloys with multiple principal elements, with the aim of identifying solid solution alloys, has been deemed untimely with limited value gained, confining alloy development to the conventional concept.

This is until the two independent publications from 2004 by Jien-Wei Yeh in Taiwan [7] and Brian Cantor in the United Kingdom [8] ignited the research on the vast compositional space of multicomponent alloys. Both investigated multicomponent alloys with different intentions but chose similar routes, which ultimately led them to the discovery of the first multicomponent single-phase alloys of equiatomic composition. These alloys are characterised by the simultaneous presence of topological order and chemical disorder, placing them in between conventional crystals, which possess both topological and chemical order, and metallic glasses, which are disordered in all regards. A prerequisite for the fundamental understanding of the consequences of these salient structural features for the physical properties is the development of high-quality materials and their meaningful characterisation, which is the aim of this work.

With the present work, a description of selected mechanical properties of two High-Entropy Alloys (HEAs) with different crystal structures shall be achieved, and insights into the salient structure-property relationships gained. This work stands out through its utilisation of high-quality, in one case, single-crystalline materials, excluding or minimising the effects of impurities, secondary phases or grain boundaries, allowing the determination of the intrinsic mechanical properties. With the successful production of CrMnFeCoNi single crystals, the critical-resolved shear stress, a basic measure of the mechanical strength of a crystal, could be investigated with respect to different crystal orientations, an important step to model and understand the plasticity of this alloy. The mechanical investigation of the TiVZrNbHf alloy revealed a yield stress anomaly at intermediate temperatures, unprecedented for any HEA to this date. Furthermore, thermodynamic activation parameters of the plastic deformation mechanisms of both alloys were determined, revealing the characteristics of their plastic deformation. The results of the mechanical investigation of the materials are accompanied by a thorough analysis of the microstructure using transmission electron microscopy to identify the governing deformation mechanisms and dislocation properties.

Chapter 2 introduces the material class of HEAs, giving an introduction to the fundamentals of multi-component alloys and their formation. These fundamentals are specified for the application to HEAs, and the specifics and limitations of the entropy hypothesis are presented. The two investigated alloys, CrMnFeCoNi and TiVZrNbHf, with their specific properties and the current state of literature, are further detailed.

In chapter 3 the fabrication of single and polycrystals of the two materials is described.

Fabrication routes, including their advantages and disadvantages, are detailed, and the respective routes that were developed for the production of CrMnFeCoNi single crystals and TiVZrNbHf polycrystals are presented. Crystals of both alloys are thoroughly characterised, and comments about the reproducibility of each fabrication route made.

The main body of the present work is enclosed in chapters 4 and 5. The plastic deformation properties of CrMnFeCoNi and TiVZrNbHf are described in two parts, with a focus on the macroscopic and the microscopic aspects. Both chapters comprise an introduction to theory and experimental methods.

Chapter 4 addresses the thermodynamics of plastic deformation of both alloys. Through dynamic compression experiments and incremental tests, thermodynamic activation parameters are determined. The results of these experiments are interpreted and discussed with respect to the current literature.

The analysis of the microstructure of deformed samples is detailed in chapter 5. Important parameters of the plastic deformation, e.g. dislocation density and Burgers vectors of dislocations, are detailed with respect to the deformation temperature and for CrMnFeCoNi, additionally with respect to the crystal orientation.

In chapter 6 a conclusive discussion with regard to both macroscopic and microscopic observations of the plastically deformed HEAs is presented. Concluding remarks about the findings of this work are given, and open questions addressed.

Chapter 2

High-Entropy Alloys

2.1 Fundamentals of Multi-Component Alloys

In a commonly accepted, narrower sense the term "High-Entropy Alloy" (HEA) refers to an alloy composed of at least four principal elements with (near-)equiatomic composition and crystallise on a simple crystal lattice, such as face-centred cubic (*fcc*), body-centred cubic (*bcc*) or hexagonal close-packed (*hcp*), with all constituent elements distributed stoichiometrically randomly on all available lattice sites [7, 9, 10]. These alloys form a single-phase solid solution with perfect topological order and complete chemical disorder as illustrated in figure 2.1(a).

Contrary to classical alloying theory, which typically focuses on the corners of phase diagrams (except selected intermetallics), HEAs originate in the middle of the compositional space in ternary, quaternary, quinary or higher-order phase diagrams as shown in figure 2.1(b) [11]. The formation of HEA can be explained by the following principles.

Thermodynamics of Solutions

In a given state, a material possesses a characteristic value of Gibbs' free energy represented by

$$G = H - TS. \tag{2.1}$$

Here, H represents the enthalpy or total energy, S the entropy, and T the temperature of the material. The change of free energy accompanying a change in the material represents a driving force given by

$$dG = dH - TdS. \tag{2.2}$$

All spontaneous changes taking place in the material must be accompanied by a reduction of the total free energy of the material. Therefore, for a change to occur, the free energy

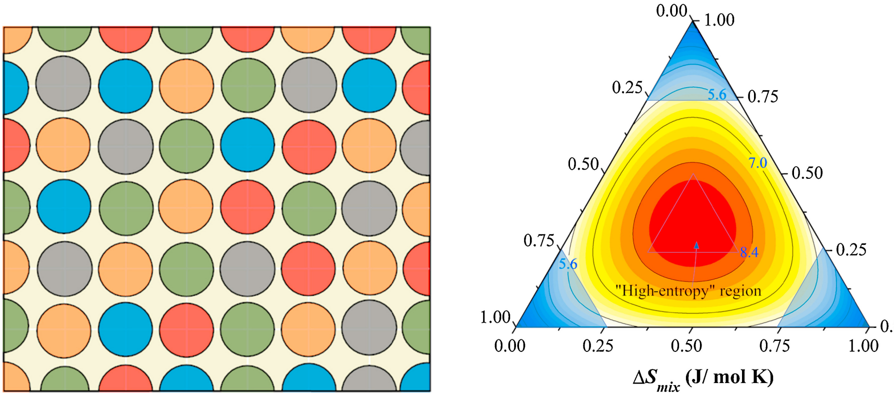

(a) **(b)**

Fig. 2.1: ***(a)*** *Schematic representation of the concept of random mixing of elements in a HEA.* ***(b)*** *A contour plot of* ΔS_{mix} *on a schematic ternary alloy system. The blue corner regions indicate the conventional alloys based on one or two principal elements, whereas the red centre region indicates the 'high-entropy' region [11].*

change ΔG must be negative. If kinetic factors are disregarded, this consideration holds true for the formation of metallic solutions, or alloys, where the mixing of elemental components is governed by the Gibbs free energy of mixing ΔG_{mix} as given in

$$\Delta G_{mix} = \Delta H_{mix} - T\Delta S_{mix}. \tag{2.3}$$

In this equation ΔH_{mix} denotes the enthalpy of mixing and ΔS_{mix} the entropy of mixing (including all entropy sources such as configurational, vibrational, electronic, and magnetic contributions). From this equation, it is evident that the phases present in a solution of elements at thermodynamic equilibrium depend on which phase exhibits a more negative ΔG_{mix}.

A mixture of two elements A and B may form a solid solution or one or more intermetallic phases when cooled from the liquid state. Within their compositional space, A and B do not necessarily need to transform entirely into an A_iB_j-type intermetallic. Rather, precipitation of intermetallics in an A- or B-rich matrix or a solid solution is possible. Additionally, if a solid solution is favoured, it may not be ideal or fully random, i.e. ΔH_{mix} is strongly negative, but also clusters of atoms can form on the lattice when ΔH_{mix} is positive or only slightly negative. It is also possible for two solid solutions to form side-by-side with differing compositions, crystal structures and/or lattice parameters.

The complexity increases for alloys consisting of three or more elements as the number of possible phases increases according to the Gibbs phase rule [12]

$$P + F = C + 2, \tag{2.4}$$

where P refers to the number of phases present at equilibrium, F the degrees of freedom (independently variable physical parameters such as temperature or pressure), and C the number of components or substances with independently variable composition in the system. It is well known that binary (e.g. Al-Cu [13] or Cu-Zn [14]) or higher-order alloys exhibit intermetallic phases that may have unfavourable (mechanical) properties.

The Entropy Hypothesis

The problem of miscibility can be simplified, as argued by Yeh et al. [7] in their first report about single-phase multi-component alloys, i.e. HEAs. The ideal mixing entropy is given by [15]

$$\Delta S_{mix} = -R \sum_{i=1}^{N} x_i ln x_i. \tag{2.5}$$

Here R denotes the universal gas constant and x_i the mole fraction of the i^{th} element. In case the alloy is equimolar, or equiatomic, with $x_1 = x_2 = x_3 = ...$ equation 2.5 can be simplified as

$$\Delta S_{mix} = R ln n. \tag{2.6}$$

Here n refers to the number of elements in the alloy. Employing this simplification, it can be observed that in alloys with multiple principal elements of equimolar composition, the mixing entropy, with values of $1.39R$, $1.61R$ and $1.79R$ for 4-,5- and 6-element alloys, respectively, predominates over the Gibbs' free energy in equation 2.3. The dominance of solid solution formation can be expressed by a factor, denoted as Ω, which is given by

$$\Omega = \frac{T_m \Delta S_{mix}}{|\Delta H_{mix}|}. \tag{2.7}$$

When the entropy effect dominates the enthalpy effect, i.e. $\Omega \gg 1$, the formation of solid solutions is likely to occur, suppressing the compound formation and resulting in random single-phase solid solutions during solidification. To estimate the likelihood of multi-component solid solution formation, the mixing enthalpy of a multi-component solid solution can be calculated using [16]

$$\Delta H_{mix} = \sum_{i,j=1;i\neq j}^{N} 4\Delta H_{AB}^{mix} x_i x_j. \tag{2.8}$$

Here ΔH_{AB}^{mix} represents the mixing enthalpy of binary alloys of the i^{th} and j^{th} component. Values for ΔH_{AB}^{mix} can be obtained from the literature, for example, here [17]. With reference to the mixing enthalpy and the estimated melting temperature

$$T_m = \sum_{i=1}^{N} x_i (T_m)_i, \tag{2.9}$$

where $(T_m)_i$ gives the melting temperature of the i^{th} component, Yeh et al. [7] introduced the concept of High-Entropy Alloys (HEAs). According to the significant role that the high mixing entropy plays in the formation of multi-principle element disordered single-phase solid solutions, they proposed the term "High-Entropy Alloys".

In addition to the high entropy of mixing, which Yeh et al. [7] regarded as essential for the formation of HEAs, another criterion has been proposed. This criterion is derived from the Hume-Rothery rules for the formation of binary solid solutions, and it is related to the atomic size difference of the alloy components. This difference can be computed using [18, 19]

$$\delta = \sqrt{\sum_{i=1}^{N} x_i \left(1 - \frac{d_i}{\sum_{j=1}^{N} x_j d_j}\right)^2}, \tag{2.10}$$

where N represents the number of elements in an alloy, x_i or x_j describes the mole fraction of the i^{th} or j^{th} element and d_i or d_j denotes the atomic diameter of the i^{th} or j^{th} element. Empirical data for several HEAs suggest that the atomic size difference for successful solid solution formation in multi-component alloys should be $\delta \leq 6.6\%$ [20].

Limitations of the Entropy Hypothesis

Although the simplification leading to equation 2.6 is valid only for equiatomic multi-component alloys, Yeh et al. [7] extended the compositional range for each constituent element to between 5 and 35 at.-%, allowing flexibility in the use of the term HEA. This greatly expanded the compositional and combinatorial range for the design of HEAs. However, the entropy hypothesis itself may only serve as an orientation for the expected formation of single-phase solid solutions in multi-component alloys, as demonstrated by Otto et.al [21]. In their investigation of equimolar five-component alloys, they found that only one alloy, apart from a model alloy, was a single-phase solid solution at room temperature. Additionally, the entropy hypothesis formulated by Yeh et al. [7] was based on temperatures near the melting point of an alloy. Nevertheless, the microstructure of an alloy can change during solidification and subsequent cooling depending on diffusion rates, phase transformation kinetics, and cooling rates [9]. Predicting compositions for potentially single-phase HEAs extends beyond the scope of this work, and interested readers are directed elsewhere for further information, such as [9, 22], and so on.

2.2 The equiatomic CrMnFeCoNi High-Entropy Alloy

The quinary equiatomic HEA with a face-centred cubic crystal structure comprising Cr, Mn, Fe, Co, and Ni was first discovered by Cantor et al. [8]. Among all reported HEAs containing five or more constituent elements, it is one of the very few single-phase solid solutions [23–25]. The solid solution formed upon cooling is, however, only stable at temperatures above 800°C, below which it decomposes into metallic (*bcc*-Cr) and intermetallic ($L1_0$-NiMn and B2-FeCo) phases [26]. This decomposition occurs over a prolonged period and has been shown to decrease with decreasing grain size [27–29]. The solid solution can be maintained through heat treatments above 800°C and standard cooling rates. The microstructure of CrMnFeCoNi has been investigated using various techniques, including X-ray diffraction [21, 30–32], scanning electron microscopy [26, 31, 33, 34], transmission electron microscopy [33–35], electron backscatter diffraction [33, 34], and atom probe tomography [27, 36]. These studies have revealed that the alloy is indeed a single-phase solid solution without any indication of local atomic clustering or short-range ordering. The presence of such local ordering would have a significant impact on the mechanical properties, as predicted by density-functional-theory calculations, which would affect critical properties such as stacking-fault energy and dislocation mobility, ultimately controlling the mechanical properties [37].
Investigation of the mechanical properties of CrMnFeCoNi began a decade after its initial discovery, unveiling several significant characteristics of the alloy [31]:

1. CrMnFeCoNi displays a notable temperature-dependent change in strength below 473 K while weakening at elevated temperatures up to 1273 K and showing a modest strain-rate dependence at low homologous temperatures.

2. Both strength and ductility increase with decreasing temperature, reaching values in excess of 1 GPa ultimate strength and 60% elongation at a cryogenic temperature of 77 K.

3. With decreasing temperature, the work-hardening rate strongly increases, postponing the onset of necking and enhancing the tensile ductility.

4. The fracture of CrMnFeCoNi occurs transgranularly, with ductile microvoid coalescence, which is consistent with the observed high ductilities.

Subsequent investigations examined the dislocation structures and microstructure evolution of CrMnFeCoNi single and polycrystals under strain. These studies revealed that slip initially occurs through planar glide of $1/2\langle 110\rangle$ dislocations on $\{111\}$ planes [35, 38–45]. Perfect dislocations tend to split into $1/6\langle 112\rangle$ partials, which bind a stacking fault with average splitting distances ranging from 3.5-4.5 nm for edge dislocations to 5-8 nm for screw dislocations, resulting in a stacking fault energy of $30\pm 5\,\mathrm{mJ/m^2}$ [39]. The large partial separations, particularly when normalized to the Burgers vector, suggest that cross-slip is less favoured in CrMnFeCoNi, which is consistent with the planar slip and long dislocation pile-ups observed in deformed CrMnFeCoNi [35, 40, 42]. Long and smoothly curved dislocations on $\{111\}$ planes without preferred line directions observed in single crystals [43] and deformed micropillars [39] indicate similar mobilities of screw and edge segments.

With increasing strain at room temperature multiple slip systems are activated and dislocations moving on inclined slip planes interact at their junctions. The dislocation density can increase substantially and eventually from well-developed cell structures at strains above 20 % [38, 35]. Twinning at room temperature has only been reported for high strains [40] or stresses close to fracture [38].

The values for the critical resolved shear stress (CRSS) for the activation of $\{111\}\langle 110\rangle$ slip at room temperature, obtained through deformation of single crystals shows values of 42-45 MPa [43] and 70 MPa [45], both in compression, and 53-60 MPa [44], 80-82 MPa [40, 46] and 44 MPa [47], all in tension. In comparison, the CRSS from polycrystals was estimated to be 55 MPa [35], while micropillar deformation yielded values of 33-43 MPa [39]. It is noteworthy that the CRSS was found to be independent of the crystal orientation in all cases.

The mechanical properties of CrMnFeCoNi at cryogenic temperatures, particularly its increased strength and ductility with decreasing temperature [35], have attracted significant attention. Although the initial deformation mechanisms are similar at room and cryogenic temperatures [38], the onset of twinning has been reported for samples deformed at cryogenic temperatures, depending on strain, crystal orientation, and whether single or polycrystalline materials were used [40, 42–45, 48]. Twinning in combination with the dynamic Hall-Petch effect provides additional hardening mechanisms that allow for a constant, steady work hardening rate at strains where dislocation hardening weakens or even fades, resulting in remarkably high strains at failure. The critical stress for the onset of twinning has been reported to vary depending on the experimental conditions, with values ranging from 153 MPa for (111)-oriented single crystals [45], 210 MPa for (001)-oriented single crystals [44], and 378 MPa for $(\bar{1}23)$-oriented single crystals [43] to 235 MPa for polycrystals [38]. The origin of the spread in values remains a subject of ongoing debate.

2.3 The equiatomic TiVZrNbHf High-Entropy Alloy

In contrast to extensively studied face-centred cubic HEAs, such as the Cantor alloy CrMnFeCoNi and its derivatives, there is a scarcity of information on the fundamental structure-property relationships of body-centred cubic HEAs, particularly refractory HEAs. Refractory HEAs were first introduced in 2010 by Senkov et al. [49] and gained interest due to their ability to maintain high strength at high temperatures up to 1600°C [50]. The initial refractory HEAs contained five elements (V, Zr, Mo, Ta, W), but subsequent alloys have been derived from a wider range of group IV, V, and VI elements. However, many of these alloys do not meet all criteria of a HEA as previously defined (cf. 2.1), and only a few five-component equiatomic refractory HEAs that form a single-phase solid solution have been reported to date [25]. One such alloy that forms a single-phase solid solution and has been more extensively studied is the "Senkov alloy" TiZrNbHfTa, which is named after Oleg Senkov due to his pioneering role in its identification and development. In its as-cast and annealed state, it exhibits a good combination of strength and ductility, with yield stresses ranging from 800 to 1000 MPa and compressive strains exceeding 50 % [51–54]. At elevated temperatures, the yield stress decreases with increasing temperature, reaching 535 MPa at 800 °C and 92 MPa at 1200 °C, respectively [51]. Tensile tests of the as-cast Senkov-alloy indicated a room temperature yield strength of 790 to 805 MPa [55], with tensile ductilities ranging from 6 to 9 %. Microstructure analysis revealed that the deformation was localized in narrow dislocation bands within large dislocation-free regions, with the number of bands and dislocation density increasing with increasing strain [53, 56, 57]. The dislocations had a Burgers vector with b=1/2⟨111⟩. The activation energy for plastic deformation, determined through stress relaxation at room temperature, was approx. 50 b^3 at yield and decreased to approx. 30 b^3 at 20 % strain [53].
The TiVZrNbHf alloy was initially investigated by Fazakas et al. [58] who reported on its mechanical properties, including a high ductility of up to 40 % for specimen heat treated at 1173 K and a yield stress of 1400 MPa. Two additional studies related to TiVZrNbHf, one calculating the mechanical properties of TiVZrNbHf through ab initio alloy theory [59] and the other describing a six-component alloy in the Zr-Nb-Ti-Ta-Hf-V system without investigating or discussing TiVZrNbHf [60], have been published. Feuerbacher et al. [61] reported on the successful production of TiVZrNbHf polycrystals through arc and levitation melting and motivated their investigation of an alternative single-phase *bcc* HEA closely related to TiZrNbHfTa as an opportunity for comparative studies. By substituting Ta with V, the melting point was calculated to be reduced from 2249 °C [51] to 2025 °C [61]. However, the inclusion of V in this alloy system may result in the formation of competing C15 Laves phases V_2Zr and V_2Hf. From thermodynamic considerations, Feuerbacher et al. [61] concluded that the formation of a single-phase solid solution is energetically favourable

compared to an alloy where either the V_2Zr or the V_2Hf Laves phase forms. The Gibbs free energy of mixing of the solid solution was determined to be -30.58 kJ/mol, compared to -27.40 kJ/mol for an alloy where the Laves phase with the lower mixing enthalpy, V2Zr, forms [61]. Transmission electron microscopy and X-ray diffraction Feuerbacher et al. [61] revealed that the TiVZrNbHf ingots indeed exhibit a single-phase bcc solid solution with a lattice parameter of 0.336(5) nm. The melting point of TiVZrNbHf was also found to be much lower (1590±20 °C) than the calculated value of 2025°C [61].

The phase stability of TiVZrNbHf was examined by Pacheco et al. [62] through CALPHAD calculations, which showed that the solid solution phase is only stable at temperatures above 830 °C, at which point it decomposes into a mixture of *bcc, hcp,* and a cubic C15 Laves phase. Through extensive annealing experiments, they demonstrated that a C14 Laves phase forms below 830 °C instead of a C15 phase and that the solid-solution phase is metastable at room temperature due to slow kinetics during cooling.

Chapter 3

Crystal Growth and Characterisation

This chapter delves into the synthesis of single and polycrystalline samples of the two HEAs investigated in the present work. Details regarding the determination of critical synthesis parameters, such as the melting temperature of the examined alloys, are provided. An optimised growth route for large-volume CrMnFeCoNi single crystals was developed through iterative adjustment of the growth parameters, and several CrMnFeCoNi single crystals were successfully produced. Furthermore, a synthesis route for TiVZrNbHf samples with two distinct grain sizes is outlined. Regrettably, the search for a growth route for single-crystalline TiVZrNbHf was unsuccessful. Additionally, the growth techniques employed in this study, including Bridgman growth, Czochralski growth, and zone melting, are discussed in detail.

3.1 Crystal Growth Methods and Materials Preparation

3.1.1 Liquid-Solid Phase Transition in Crystal Growth

A liquid that is cooled beyond its equilibrium melting temperature, i.e. under- or super-cooled, experiences a driving force for solidification. This process begins with the formation of tiny particles or nuclei, which are phase areas created by thermal fluctuation that are in a critical state. In order for the entire melt to solidify, the nucleus must grow at the expense of nucleation work. Once the nucleus reaches a minimal radius, it is stable, can grow and form a solid phase. The process of solidification can be illustrated by a simple phase diagram, such as the one shown in figure 3.1. This phase diagram shows a binary alloy exhibiting a perfect solid solution. If a melt with a composition C is cooled below its melting temperature (point 1), nucleus formation is initiated in the phase region where liquid and solid phase coexist. If the melt is cooled further, the nuclei grow in size until the entire melt solidifies at point 2. In

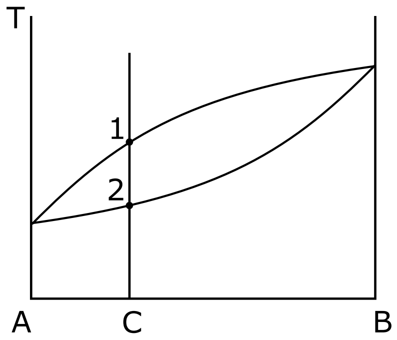

Fig. 3.1: *Phase-diagram representation of the solidification of an alloy exhibiting perfect solid solution*

more complex phase diagrams, the melt may undergo further reactions during solidification, depending on its composition and the stability of the solid phases at temperatures below the melting point. Crystal growth, as it is used in the present work to produce single crystals, is a near-equilibrium process similar to the formation of nuclei in a liquid. Single crystals are thus synthesised by setting the external conditions for the desired equilibrium state, as described through the phase diagram, and allowing the system to move towards this state in a controlled fashion by setting temperature gradients, cooling rates and withdrawal rates, all of which influence the growth rate of the crystal. For a more detailed description of the thermodynamics involved in solidification and crystal growth, the interested reader is directed to sources such as [63].

In this work three growth methods have been utilised for the synthesis of high-quality HEA crystals: Czochralski growth, Bridgman growth and Zone melting. These techniques were employed with the aim of producing single-phase, and in the best case, single-crystalline HEAs. Master alloys for each of these growth techniques were produced using cold crucible levitation melting.

3.1.2 Cold Crucible Levitation Melting

In cold crucible levitation, metals are melted through inductive coupling to a high-frequency current. The high-frequency current, applied via a coil, induces electromagnetic forces in the melt, leading to levitation and strong stirring and resulting in the melt's alloying without contamination from a crucible. The schematic principle of cold crucible levitation melting as employed in the present work is illustrated in figure 3.2.

The ingot is placed in a water-cooled crucible made from oxygen-free high-purity copper segments, and a coil wrapped around the crucible is connected to a high-frequency power supply. The high-frequency current running through the coil induces eddy currents in the

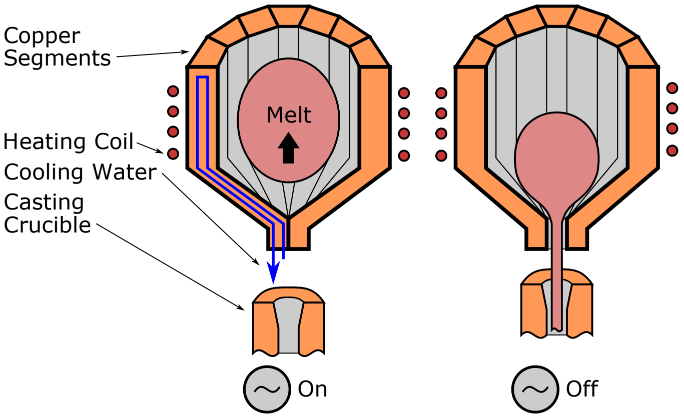

Fig. 3.2: *Schematic principle of a cold crucible levitation melting with (left) the current switched on and melt levitating and (right) the current switched off and gravitational casting in progress*

ingot and the crucible, generating Joule heat and causing the ingot to levitate as a result of the current-induced electromagnetic field. Once the ingots is melted, it is held in this state for some time to improve its homogenisation. Subsequently, the high-frequency current can be shut off, and the levitation of the melt is terminated. The melt then rapidly solidifies when making contact with the copper crucible.

In the present work, the melt was gravity-cast into a rod-shaped copper crucible by creating a slit in the copper crucible segments in the instant the current was turned off. Both CrMnFeCoNi and TiVZrNbHf rods, which were used throughout this work, were cast in this manner.

3.1.3 Czochralski Growth

In Czochralski growth [64], a crystal is formed through the solidification of a melt around a seed crystal. Figure 3.3 depicts the general setup of the Czochralski apparatus employed in the present work. The melt is heated in a cylindrical crucible via an induction coil. The seed crystal utilised in the process can be made of the same phase or crystal structure as the desired crystal (homogeneous seeding) or made from a different material with a sufficiently high melting point (heterogeneous seeding). Homogeneous seeding is beneficial when the melt should crystallise along a predetermined direction, which is defined by appropriately orientating the seed crystal.

The seed crystal is suspended from a pulling rod and, once the melt reaches the desired temperature for growth, is dipped into the melt. When the seed crystal is pulled out of the melt at an appropriate velocity, a stable meniscus can form at the solid-liquid interface.

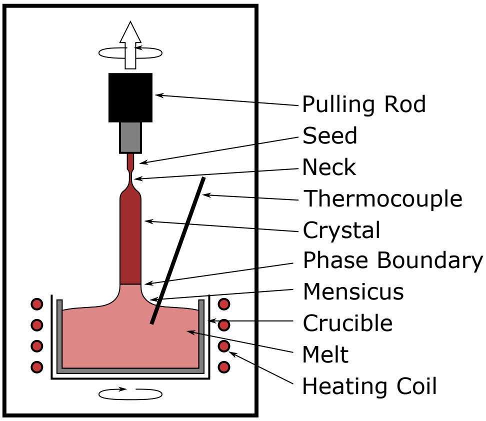

Fig. 3.3: *Schematic setup for the growth of single-crystals using the Czochralski technique*

By continuously pulling the rod, the crystal grows, with the diameter of the meniscus determining the crystal diameter and being influenced by the melt temperature and/or pulling velocity. A good homogenisation of the crystal can be achieved by rotating the pulling rod and the crucible relative to one another.

The neck, as shown in figure 3.3, is an area of the crystal where its diameter is temporarily reduced to attempt the selection of one grain that fills the entire volume of the crystal once the diameter is increased again. Introducing a neck during pulling enhances the chances of growing large-volume single crystals. The temperature of the melt is continuously monitored with a thermocouple, and the growth process can be conducted under a vacuum or a gas atmosphere.

In the present work Czochralski growth was employed to attempt the production of single-crystalline CrMnFeCoNi initially.

3.1.4 Bridgman Growth

The Bridgman technique [64], similar to the Czochralski method, is a melt-based crystal growth technique that involves growing a crystal by moving a crucible filled with the desired material across a steep temperature gradient in a controlled fashion. In a furnace, two regions of different temperatures are separated, and a crystal is grown by moving the crucible from the part above the melting temperature to the one below the melting temperature .

A schematic setup of the configuration used in the present work is shown in figure 3.4. The crucible, which has a double-conical pointed-tip shape, is placed inside a furnace on a retractable water-cooled pulling rod under a vacuum or an inert gas. The temperature of the crucible is controlled through a thermocouple placed inside the furnace, and ideally, the heater creates an isothermal hot zone enclosing the full volume of the crucible. The solidification is initiated by pulling the crucible downwards out of the hot zone. A water-cooled baffle creates a steep temperature gradient through which the crucible is pulled, and when moving through the cooling baffle, a sharp and distinct solid-liquid interface is created in the crucible, along which the melt solidifies. By design, the melt will first solidify at the lowest end of the crucible, and the solidification will continue as the crucible is pulled through the cooling baffle. The pointed tip of the crucible will provide a very small first solidification volume, aiding the selection of a single nucleus in the reduced volume of the lower cone.

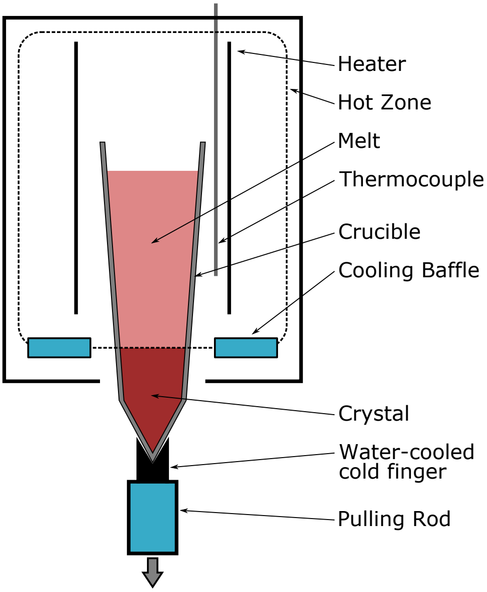

Fig. 3.4: *Schematic setup for the growth of single-crystals using the Bridgman technique*

The Bridgman technique was extensively utilized in the present study for the synthesis of single-crystalline CrMnFeCoNi and in attempts to grow single-crystalline TiVZrNbHf.

3.1.5 Zone Melting

Zone melting or zone refining [65] is a technique based on initially solid materials. Figure 3.5 shows the schematic setup as used in the present work. In this technique, a cylindrical ingot is placed in a vacuum or inert gas-filled chamber and suspended from a rotatable pulling rod that is clamped at the lower end into a rotatable feeding rod. The ingot is heated in a localized volume using an induction coil, and as the liquid-solid interface continuously moves through the ingot, a single-crystalline volume is created. This technique is particularly advantageous for materials with high vapour pressures, as it involves a small liquid volume, thereby minimizing the risk of excessive evaporation that can occur with other methods such as the Czochralski and Bridgman techniques. In the present work, zone melting was employed to produce single-crystalline TiVZrNbHf.

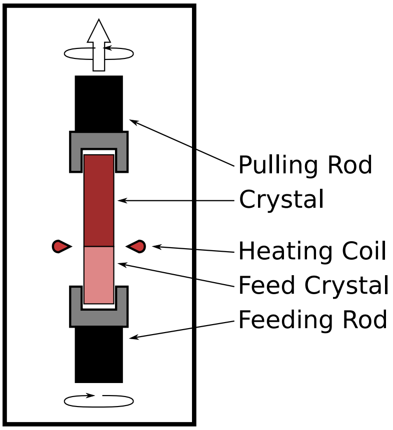

Fig. 3.5: *Schematic setup for the growth of single-crystals using the Zone Melting technique*

3.2 Fabrication of equiatomic CrMnFeCoNi

In the initial stage of the crystal growth experiments on CrMnFeCoNi, a master alloy was produced using high-purity elements that were weighed to achieve an equiatomic composition. The elements were charged into a cold crucible levitation melting device and subjected to multiple melting cycles to ensure a high degree of homogenization. Subsequently, the melt was cast into a rod shape with a 10 mm diameter for easier handling along the subsequent process.

The determination of the melting temperature of the CrMnFeCoNi HEA is crucial for a well-designed crystal growth process. The melting temperature was determined using differential scanning calorimetry (DSC) on a Setaram SetSys Evolution DSC system [66]. Three consecutive heating cycles at a heating rate of 10 K/min were conducted, and the results are shown in figure 3.6. In all three cycles, a distinct melting event was observed. The melting temperature was determined at the point of the energy minimum, which corresponds to the endothermic melting reaction at 1354±5 °C. The slight variation in the melting temperature between the three cycles may be attributed to the continuous homogenization of the sample during the experiment and the annihilation of mechanical stresses during the first

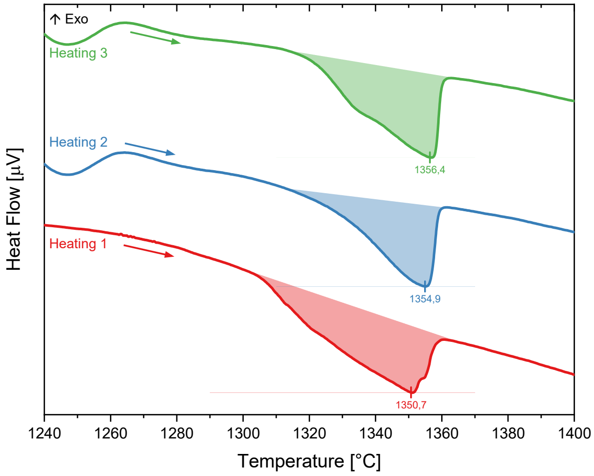

Fig. 3.6: *DSC heating cycles of the CrMnFeCoNi master alloy with the melting temperature indicated for each cycle*

cycle, which may lower the melting point [67]. The measured melting temperature is in good agreement with values predicted by CALPHAD and Thermo-Calc calculations, which estimate the melting temperature of the CrMnFeCoNi alloy at 1300±50 °C [68–70]. It should be noted that these values differ significantly from the melting temperature calculated using Vergard's law [71], which predicts a melting temperature of 1516°C based on the weighted average of the individual elements' melting temperatures.

3.2.1 Growth of Single Crystals

Preliminary experiments were conducted to design a growth route using the Czochralski and Bridgman techniques with full-volume initial ingots. The knowledge gained from these experiments was utilised to develop an optimised growth route.

The master alloy ingot produced by cold crucible levitation melting was cut into several pieces of approx. 1-1.5 cm^3. About 70 g of these pieces were charged into a pointed-tip double-conical shaped alumina crucible, which was placed in a Bridgman apparatus under a 300 mbar Argon atmosphere. The Bridgman furnace was heated to 1360 °C, slightly overheating the material to guarantee a fully molten ingot and further increase the homogenisation of the melt while avoiding excessive evaporation of Mn.

The melt was homogenised for 1 h before the crucible was withdrawn from the furnace through the cooling baffle. All samples investigated in the scope of this work were withdrawn from the hot zone at a rate of 100 mm/h. The influence of the withdrawal rate on the morphology of the CrMnFeCoNi crystals was also investigated within this work, and the results are described in 3.2.2. The general crystal growth process is illustrated in figure 3.7,

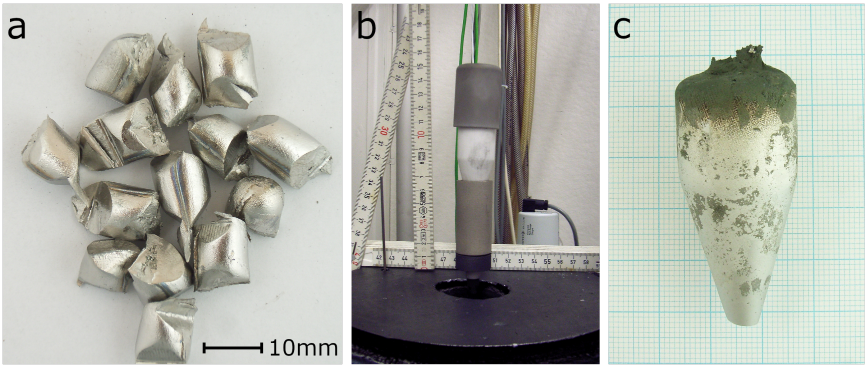

Fig. 3.7: *Generalised process for the synthesis of high-quality CrMnFeCoNi single-crystals using the Bridgman technique: (a) charge, (b) Bridgman set up in the laboratory and (c) as-grown single-crystal*

where figure 3.7(a) shows the ingot pieces used as charge, 3.7(b) the crucible on top of the water-cooled pulling rod in the Bridgman apparatus, and 3.7(c) an as-grown single-crystal. It is notable that all single crystals produced through the process described here have a rounded tip and did not fully fill the crucible tip.

3.2.2 Influence of the Withdrawal Rate

Within this work, the influence of the withdrawal rate during Bridgman growth on the microstructure of CrMnFeCoNi was investigated. This is of interest as lower withdrawal rates may lead to the evaporation of Mn due to prolonged times at elevated temperatures. Furthermore, the withdrawal rate influences the final microstructure of the crystal and can determine whether a single crystal is produced during growth.

Figure 3.8(a) depicts the microstructure of a crystal grown at a rate of 100 mm/h, as observed in phase-contrast light microscopy [72]. Figures 3.8(b) and 3.8(c) show the microstructure of crystals grown at rates of 50 mm/h and 20 mm/h, respectively. For comparison, figure 3.8(d) shows the microstructure of a crystal grown using the Czochralski technique at a withdrawal rate of 5 mm/h. The crystals were oriented so that the $(0\bar{1}1)$ plane was parallel to the polished surface, where possible. Reducing the withdrawal rate from 100 mm/h to 50 mm/h still resulted in a large single-crystalline volume with a consistent dendrite structure. The secondary dendrite arm spacing increased slightly, and the length of the secondary dendrites was reduced with the decreased withdrawal rate. Reducing the withdrawal rate further to

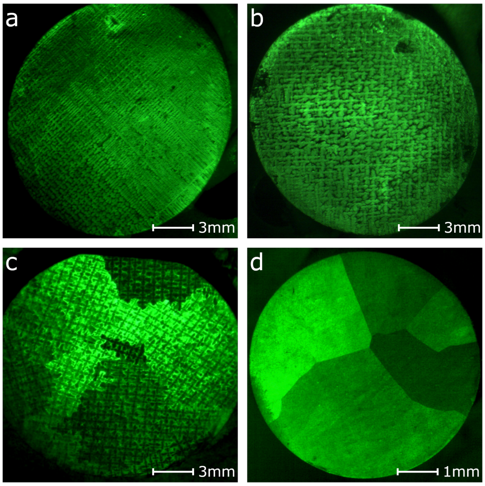

Fig. 3.8: *Phase-contrast light microscope micrographs of crystals grown at withdrawal rates of (a) 100 mm/h, (b) 50 mm/h and (c) 20 mm/h using the Bridgman technique and (d) 5 mm/h using the Czochralski technique*

20 mm/h and 5 mm/h, respectively, led to the formation of grain boundaries. The crystal produced at a withdrawal rate of 20 mm/h (figure 3.8(c)) exhibits large grains with a dendritic microstructure. Secondary dendrite arm spacing and length are comparable to the 50 mm/h Bridgman sample. The crystal produced by Czochralski growth was polycrystalline, with a grain size comparable to that of the 20 mm/h Bridgman sample, but exhibited no dendrites. The morphology of the liquid-solid interface or the growth front is influenced by the velocity at which it moves through the melt, the solute concentration and the temperature gradient at the interface [65]. When the temperature gradient at the interface and the flow of latent heat into the liquid are high, the growth front is not flat but can form cells or dendrites [63]. At high withdrawal rates, the solidification plane moves quickly through the liquid, hindering diffusion processes, which can result in a wide impurity layer at the interface. Models developed for the solidification superalloys predict that increasing the withdrawal rate refines the dendritic microstructure [73–76]. This has been confirmed in experiments for a range of Ni-based superalloys [77–82] and withdrawal rates of up to 350 mm/h [82]. A refinement of the dendritic microstructure by a factor of 10 when increasing the withdrawal rate by a factor of 10 has also been reported for directionally solidified HEAs in the Al-Cr-Fe-Co-Ni [83, 84] and Cr-Fe-Co-Ni-Cu [83] systems. The observations made in this work are therefore consistent with previous experiments.

The absence of dendrites in the crystal grown using the Czochralski technique (cf. figure 3.8(d)) is likely due to the slow withdrawal rate that was used, which results in an extended exposure of the crystal to high temperatures, similar to a heat treatment. The effects of this on the microstructure of a CrMnFeCoNi crystal are described later in this chapter. It has not been reported before that single crystals could only be grown using high withdrawal rates and that slow withdrawal rates do not yield single-crystalline results. In two prior studies, single crystals of two variations of the Al-Cr-Mn-Fe-Co alloy were successfully synthesised using the Bridgman technique and the floating zone approach, respectively, at a withdrawal rate of 5 mm/h [85, 86]. This finding supports the general consensus that slower withdrawal rates lead to higher quality crystals [65]. This evidence also calls into question the notion that the high chemical complexity of high-entropy alloys (HEAs) necessitates high withdrawal rates for promoting single-crystalline solidification. Therefore, it is essential to further investigate the influence of the withdrawal rate on the solidification and crystallinity of CrMnFeCoNi and other single-phase HEAs.

3.2.3 Characterisation and Reproducibility

Any CrMnFeCoNi crystal that was grown was initially immersed in Kalling's reagent II [87] solution for approximately two hours. Afterwards, the crystal was mounted on a goniometer and examined using a Laue X-ray apparatus with a back-reflection geometry [88]. With this method, the back-reflection patterns obtained across the external surface of the as-grown crystal can be verified for their consistency, meaning that when distinct rotations relative to the initial spot yield an expected pattern, there is a high probability for a single crystalline volume.

Figure 3.9 displays a sequence of Laue X-ray backscatter images captured at an intermediate height of an as-grown crystal. The goniometer was used to rotate the crystal so that a low-index crystallographic axis was revealed in the Laue pattern. Subsequent patterns were recorded after rotating the crystal. The Laue patterns displayed sharp, singular spots and are mutually consistent regarding their relative tilting angles. Figure 3.9(a) displays the fourfold axis of the (100) plane, figure 3.9(b) the (111) plane and figure 3.9(c) the twofold pattern of

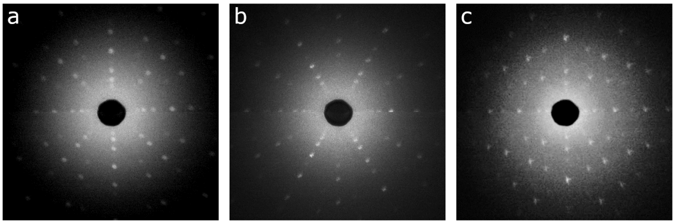

Fig. 3.9: *Laue backscatter patterns at intermediate height of a 100 mm/h Bridgman as-grown CrMnFeCoNi single-crystal: (a) fourfold (100) plane, (b) threefold (111) plane and (c) twofold (011) plane*

the (011) plane which is tilted 55° and 90° away from the (100) plane and by 35° with respect to each other. The $(0\bar{1}1)$ plane is tilted about 15° away from the growth direction. A series of Laue patterns recorded on either side of the crystal perpendicular to the $(100)/(\bar{1}00)$ was used to estimate the size of the single grain. It extends from approximately 1 cm above the lower end of the crystal to just below the wide end, amounting to a volume of approximately 7 cm^3 (cf. figure 3.7(c)).

Figure 3.10 depicts the microstructure of a sample slice from the as-grown crystal, captured through phase-contrast light microscopy and backscattered-electron mode in a scanning electron microscope at an approximate distance of 2 cm from the tip. The $(0\bar{1}1)$ plane of the crystal is aligned parallel to the polished surface, and the crystal exhibits a low porosity with only a few pores of dark contrast visible in the SEM micrograph. Energy-dispersive X-ray spectroscopy [89] was used to determine the overall composition of the crystal, which was found to be $\mathrm{Cr}_{20.33}\mathrm{Mn}_{20.10}\mathrm{Fe}_{20.00}\mathrm{Co}_{19.64}\mathrm{Ni}_{19.94}$. The phase-contrast micrograph reveals the dendritic microstructure of the as-grown crystal, as previously described. A slight inhomogeneity in the elemental composition across the sample is visible in the backscattered-electron image, indicating that the formation of dendrites is accompanied by segregation of the constituent elements of the alloy. Laue X-ray backscatter patterns taken across the surface of the sample show tilts of up to approx. 5° between individual regions of the crystal, as illustrated in figure 3.11. These tilts are continuous across the sample surface and may suggest the presence of sub-boundaries within the as-grown crystal. The presence of tilt boundaries within a single crystal is attributed to an imperfect growth process, which disrupts the perfect three-dimensional translation symmetry. This phenomenon is commonly referred to as crystal mosaicity [90–92].

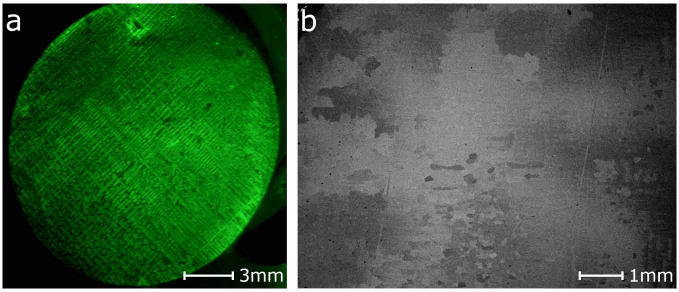

Fig. 3.10: *(a) Phase Contrast and (b) SEM back-scattered electron micrograph of a 100 mm/h Bridgman as-grown CrMnFeCoNi single-crystal*

Figure 3.12 depicts Electron Backscatter Diffraction (EBSD) measurements for slices taken from the crystal's foremost tip, extending approximately 8 mm along the growth direction. Panel A-D displays the band contrast image, which is a secondary electron image capturing

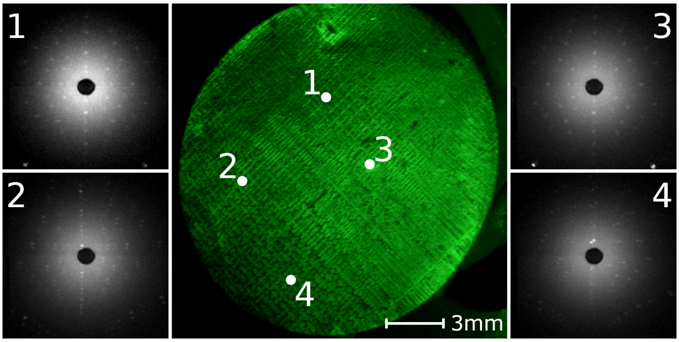

Fig. 3.11: *Representative micrograph of tilts between individual regions in a 100 mm/h Bridgman as-grown CrMnFeCoNi single-crystal observed using the Laue X-Ray backscatter patterns. The initial pattern was taken at spot 1, depicted in image 1, with patterns from spots 2-4 taken without rotation of the sample. This reveals a tilt of the pattern in spots 2 and 4.*

the analysed region for the EBSD orientation determination. The in-plane x component represents the crystal orientation in the image plane, pointing upward, while the out-of-plane z component indicates the orientation of the crystal away from the image plane and towards the viewer. The Laue X-ray back-reflection revealed an absence of a consistent orientation for the foremost tip of the crystal, with indistinct or unidentifiable patterns. In the inverse pole figures, particularly in the in-plane x and out-of-plane z components shown in figure 3.12, the polycrystalline nature of the first 8 mm of the crystal volume is evident. The individual crystallites are largely oriented in close proximity to similar crystallographic directions, namely the in-plane x direction (001) and the out-of-plane z direction (101), as indicated by the colour-coding of the inverse pole figure in the bottom left corner. The crystallite size increases along the growth direction (Slice A to C), with the crystallites predominantly oriented along (001) in the x-direction (fire-red areas) and (101) in the z-direction (neon-green areas), respectively. At the height of slice D, individual crystallites are difficult to distinguish, with a significant portion of the volume aligned along the (101) direction in the z-direction and close to the (001) direction in the x-direction. The microstructure observed in slice D is representative of the entire volume of the as-grown single crystal as shown in figure 3.10 and 3.11. The distortion from the (101) plane (light blue areas) observed in slice D may be attributed to the effect of crystal mosaicity, which is also observed in the single-crystal volume in figure 3.10 and 3.11. This indicates that although the tip of the alumina crucible was not fully filled during the Bridgman growth, a single crystal was still successfully grown through the process of self-selection of a dominant grain. The microstructure presented here was reproducible in two additional crystals grown using the same parameters.

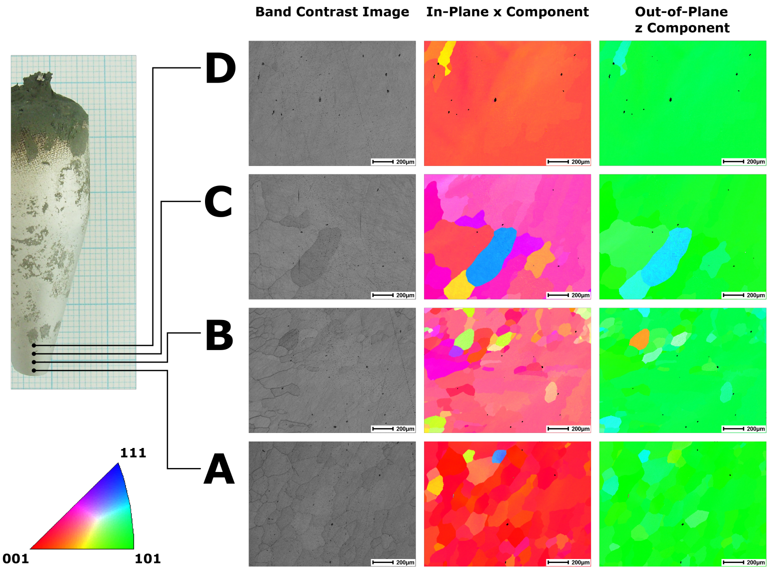

Fig. 3.12: *SEM band contrast micrographs and EBSD inverse pole figures of the foremost tip area of a 100 mm/h Bridgman as-grown CrMnFeCoNi single-crystal*

3.2.4 Heat Treatment of as-grown CrMnFeCoNi Single Crystals

Figure 3.13(a) displays the distribution of the constituent elements in a specimen grown at a withdrawal rate of 100 mm/h using the Bridgman technique in the as-grown state. As seen in the EDX element maps, there is a slight segregation of Mn and Ni present. From the scale of the inhomogeneities, it is inferred that they correspond to the dendrites observed in figure 3.10. The interdendritic areas, which are enriched in Mn and Ni, are depleted of Cr, Fe, and Co.

Figure 3.13(b) illustrates the elemental distribution after subjecting the sample to a heat treatment at 1200 ° for 72 h in vacuum using Ti as an oxygen getter. The constituent elements are now uniformly distributed throughout the crystal's volume. An EDX line-scan, depicted in figure 3.14, performed across the surface of the specimen before and after the heat treatment shows that in the as-grown state, the concentration of the constituent elements can vary by up to ±5 at-% from the nominal 20 at-%. After the heat treatment, the concentration of the constituent elements only varies by approx. ±0.5 at-%, which is within the relative error of common EDX systems. This finding is consistent with earlier reports on heat treatments of CrMnFeCoNi, which indicate that exposure to 1200 °C in a vacuum for an extended period of time yields a homogeneous single-phase material [21, 26]. Therefore, a heat treatment subsequent to crystal growth should be beneficial for future investigations.

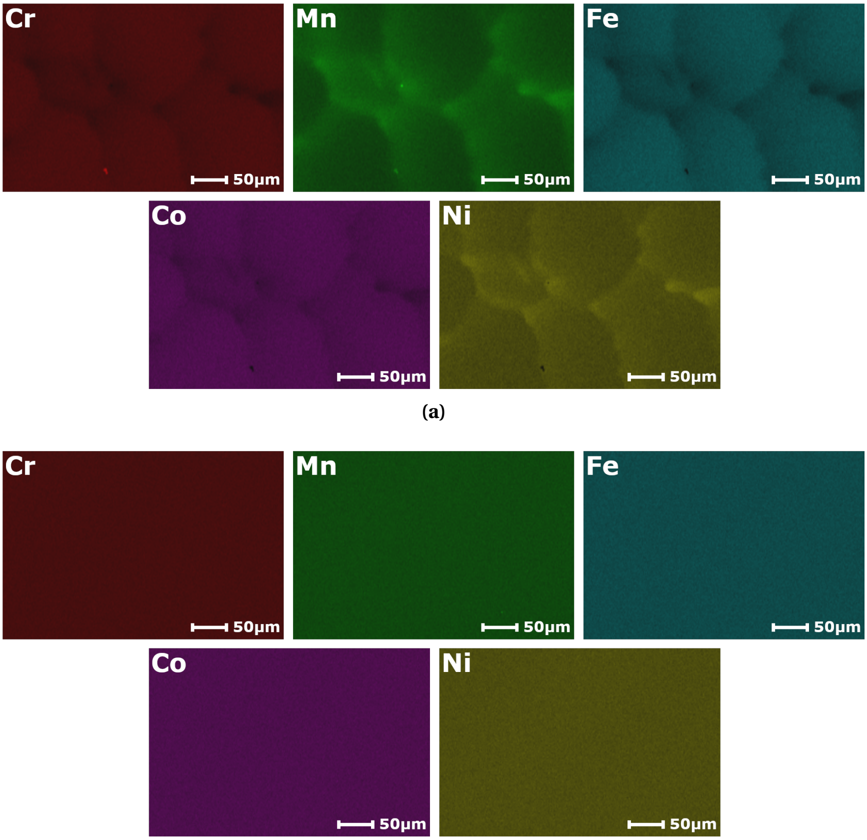

(a)

(b)

Fig. 3.13: *EDX maps of the constituent elements in the (a) as-grown 100 mm/h Bridgman crystal and (b) after a heat treatment at 1200 °C for 72 h*

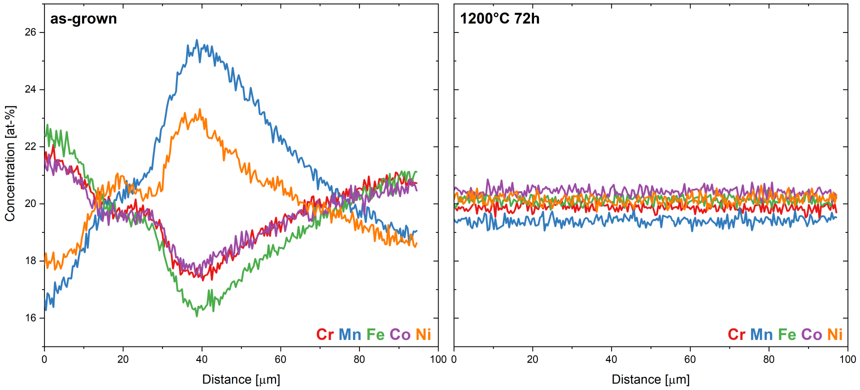

Fig. 3.14: *EDX line scans of the constituent elements in the as-grown and heat-treated 100 mm/h Bridgman crystal*

Due to time constraints and concurrent investigations, all CrMnFeCoNi samples in this work are in the as-grown state.

3.3 Fabrication of equiatomic TiVZrNbHf

The initial stage in the production of the equiatomic TiVZrNbHf alloy involves the synthesis of a master alloy from high-purity elements. Due to the significant variation in the melting points of some of the constituent elements, such as Hf at 2227 °C, an additional step was introduced in the fabrication process compared to the CrMnFeCoNi alloy. To achieve high homogeneity of the material, platelets containing the constituent elements in equiatomic proportion were remelted several times in an arc-melter. Approximately 70 g of these platelets were then charged into a cold crucible levitation melter, similar to the CrMnFeCoNi alloy, and remelted at least twice for further homogenization. Finally, the melt was cast into a rod shape with a diameter of 10mm.

DSC measurements did not provide reliable data for the melting point of the TiVZrNbHf alloy. Unlike the CrMnFeCoNi alloy, no distinct melting event could be detected in the DSC measurement curves (cf. figure 3.15). The melting point of the alloy was estimated through a series of melting experiments. Small amounts of the alloy were heated at a low rate to temperatures above and below the estimated melting point (±100 °C), and the presence of molten samples was observed. The melting event was narrowed down to a range of 1550-1650 °C. The melting temperature was then approximated by scanning this temperature range in 10 °C-steps and was found to be 1590±20 °C [61]. This value is consistent with

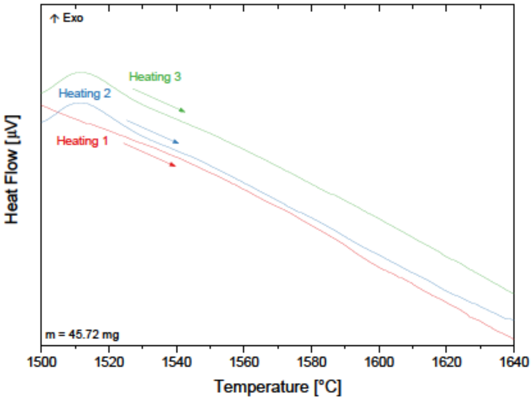

Fig. 3.15: *DSC heating cycles of the TiVZrNbHf master alloy revealing no distinct melting event*

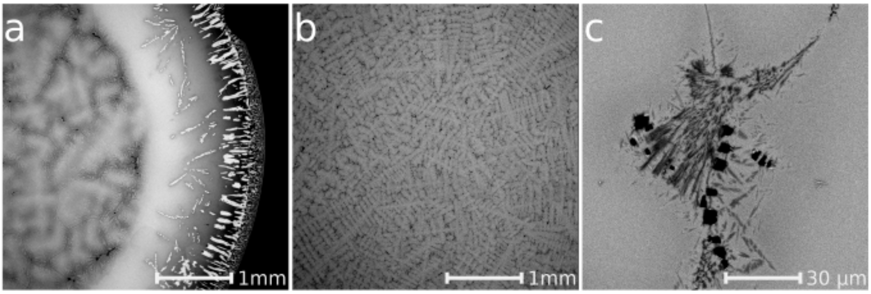

Fig. 3.16: *SEM Micrographs (BSE-detector) of as-grown Bridgman samples of the TiVZrNbHf alloy: (a) crystal grown in an alumina crucible showing strong crucible interaction, (b) crystal grown in glassy carbon crucible with (c) an enlarged view of the microstructure with a V-Nb-Ti -rich phase appearing darker and a Zr-Hf-rich needle-shaped phase*

CALPHAD calculations, which estimated the melting temperature to be 1490,°C [62], but is lower than the melting point calculated from the weighted average at 2025 °C.

3.3.1 Fabrication of Polycrystals

The development of a single crystal production route for TiVZrNbHf commenced with the straightforward process of producing single-crystalline CrMnFeCoNi. Nevertheless, the application of the Bridgman technique with various crucible materials, ranging withdrawal rates from 5 to 500 mm/h, and improved cooling at the baffle proved unsuccessful in yielding single crystals. The material showed strong interaction with alumina crucibles, as demonstrated in figure 3.16(a). Secondary and ternary phases, as illustrated in figure 3.16(b) and (c), were observed in crystals grown using zirconia, pyrolytic boron nitride, or glassy carbon

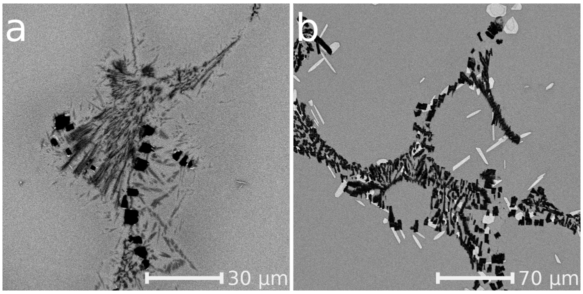

Fig. 3.17: *V-Ti-Nb-rich phase appearing dark and Zr-Hf-rich needle-shaped phase appearing bright in TiVZrNbHf crystals in (a) the as-grown state and (b) after 48 h at 1200 °C*

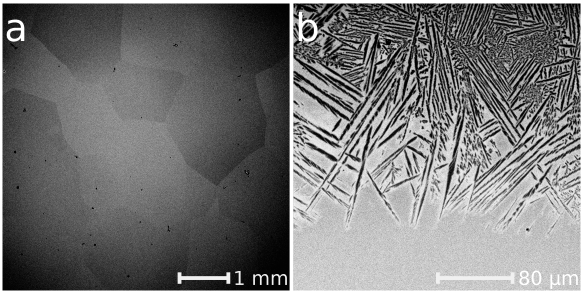

Fig. 3.18: *SEM Micrographs (BSE-detector) of TiVZrNbHf crystals produced by zone melting in (a) the as-grown state and (b)details of V-rich needles at the outer edge of the as-grown crystal*

crucibles. However, a heat treatment within the solid solution region of the TiVZrNbHf phase diagram, as presented by Pacheco et al. [62] at 1200 °C for 48 h did not remove these phases, as depicted in figure 3.17. The use of zone melting to produce TiVZrNbHf crystals resulted in a polycrystalline product, as shown in figure 3.18(a). The formation of multiple grains in the crystal may have been due to problems with stabilizing the molten zone and continuously feeding the rod through the heating coil, potentially preventing the synthesis of single crystals. Furthermore, the crystals produced by zone melting exhibited V-rich needles along the outer edge of the crystal, making them unsuitable for the purposes of this work.

Another issue that arose during the search for a single crystal growth method was the phase stability of TiVZrNbHf, as described by Pacheco et al. [62]. The solid solution of TiVZrNbHf is only stable at temperatures above 830 °C, and decomposes at lower temperatures. However, the high-temperature solid solution can be frozen in its state through moderate cooling rates. If these cooling rates cannot be achieved, a decomposition of the solid-solution phase will take place as most likely happened during Bridgman growth as depicted in figure 3.16 and 3.17. This is due to the fact that the cooling rate of the crystal cannot be sufficiently controlled once it has passed through the cooling baffle of the Bridgman apparatus, and the temperature of the crystal may be high enough for decomposition to occur, as predicted by Pacheco et al. [62]. Unfortunately, a higher cooling rate could not be achieved with the given experimental setup. Therefore, the search for a method to synthesize single crystals of the TiVZrNbHf alloy was limited to the available techniques, which ultimately proved unsuccessful.

The investigation of the TiVZrNbHf alloy was subsequently concentrated on polycrystalline samples. In preparation for the mechanical experiments, the master alloy rods underwent a heat treatment. This treatment was used to first remove any inhomogeneities that resulted from the rapid cooling during casting. Additionally, the grain size of the material was controlled by varying the length of the heat treatment. The Bridgman apparatus was utilized for the heat treatments as it is capable of achieving the necessary temperatures and atmosphere for the process. Specifically, two heat treatments in an Argon atmosphere were conducted at 1200 °C for 2 h and 48 h, respectively. Following the heat treatments, the samples were cooled in the Bridgman machine at a rate of 600 K/h until 500 °C and afterwards at 200 K/h until room temperature.

3.3.2 Characterisation and Reproducibility

In the as-cast state, the TiVZrNbHf rods exhibit an inhomogeneous microstructure as depicted in figure 3.19(b). The microstructure is dense with a few pores and shows few larger inhomogeneities. The overall composition was determined to be $Ti_{19.29}Zr_{20.87}Nb_{20.30}V_{19.89}Hf_{19.66}$ through EDX analysis. The composition of the larger inhomogeneity, identified by its bright contrast in figure 3.19(a)) was found to differ only slightly from the overall composition, with an approximate 1 at-% increase in Zr content and equal decreases of 0.2 at-% each in the other elements. EBSD measurements, shown in figure 3.20, revealed a grain size of 10-50 μm

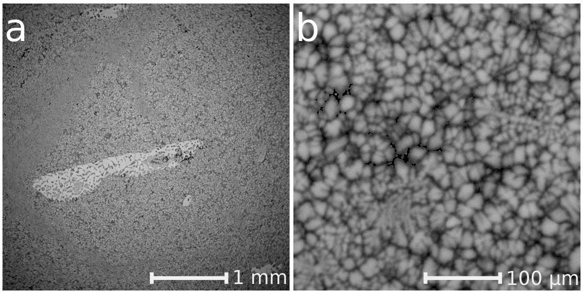

Fig. 3.19: *Microstructure (SEM BSE-contrast) of an as-cast TiVZrNbHf rod, (a) overview image and (b) detail of the microstructure displaying inhomogeneous element distribution*

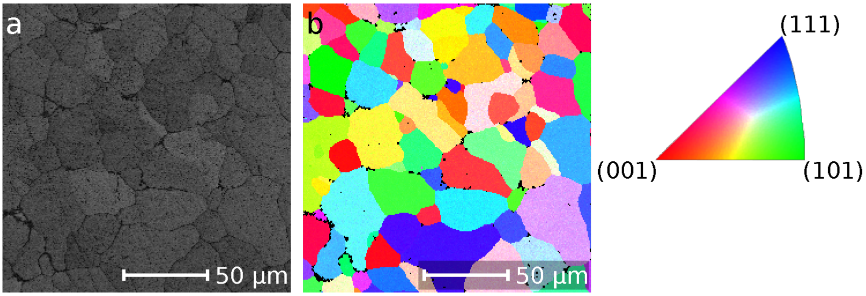

Fig. 3.20: *SEM secondary electron contrast micrograph (a) and inverse pole figure (b) of the as-cast TiVZrNbHf master alloy*

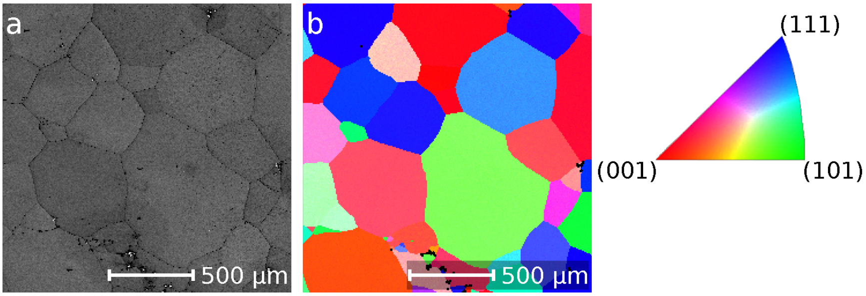

Fig. 3.21: *SEM band contrast micrograph (a) and inverse pole figure (b) of the TiVZrNbHf master alloy annealed for 2 h at 1200 °C*

in the centre of the rod. No preferential orientation of the individual grains was observed. To eliminate the non-homogeneous microstructure, the as-cast samples were subjected to two heat treatments at 1200 °C for 2h and 48 h, which were followed by cooling in the furnace at cooling rates of 500 K/h until approx. 600 K and at 200 K/h thereafter until room temperature.

The microstructure of a sample annealed at 1200 °C for 2 h is depicted in figure 3.21(a). The most significant observation is the increase in grain size after heat treatment compared to the as-cast state, where individual grains are clearly visible. The estimated grain size is approximately 300-500 μm. The microstructure is homogeneous, and no segregations or secondary phases were observed. The overall composition of the sample, determined by EDX to be $Ti_{19.55}Zr_{19.43}Nb_{21.61}V_{19.27}Hf_{20.14}$, is, similar to the as-cast sample, close to equiatomic. The inverse pole figure of an EBSD measurement performed after the heat treatment, shown in figure 3.21(b), confirms the grain size of 300-500 μm. The random orientation of the individual grains is clearly visible.

Figure 3.22 displays the microstructure of a sample annealed at 1200 °C for 48 h. The inhomogeneities present in the as-cast sample have been dissolved, and individual grains

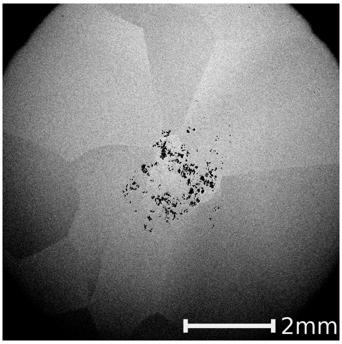

Fig. 3.22: *SEM micrograph of the TiVZrNbHf master alloy annealed for 48 h at 1200 C*

are clearly visible. The grain size has increased significantly compared to the as-cast state, with some measuring up to 1 mm in size. The sample exhibits a dense and homogeneous microstructure. The dark spots in the centre of the sample were identified as residual pores or shrinkage cavities from the casting process. The deformation samples for this material were machined from areas that show no shrinkage cavities. EDX measurements indicate that the composition is close to equiatomic at $Ti_{19.10}Zr_{19.58}Nb_{22.21}V_{19.22}Hf_{19.89}$.

Both heat treatments were performed on two different master alloy rods each time, resulting in comparable microstructures and grain sizes as described here. It was demonstrated that the selected cooling rates effectively prevent the decomposition of the alloy, as described in paragraph 2.3 [62]. Samples that underwent either heat treatment were deformed and investigated in the scope of this work. Throughout this work, samples that were annealed for 2 h will be referred to as fine-grained, and those annealed for 48 h as coarse-grained, respectively.

Chapter 4

Mechanical Properties of plastically deformed High-Entropy Alloys

This chapter provides a comprehensive overview of the fundamental principles of crystal plasticity. It discusses the physical concepts of dislocation motion and the theoretical underpinnings of thermal activation processes. Additionally, the experimental techniques utilized to determine thermodynamic activation parameters are explained in detail, as well as the general procedure for conducting deformation experiments. These experimental methods were employed simultaneously for the study of CrMnFeCoNi and TiVZrNbHf, with the primary difference between the two materials being the maximum deformation temperature. The strength of CrMnFeCoNi diminishes significantly above 500 K, falling within the resolution limit of the deformation machine employed. Conversely, the maximum deformation temperature for TiVZrNbHf was limited to 1150 K due to the alloy's significant softening above this temperature, as well as the potential formation of toxic Vanadium-(V)-oxide [93]. The chapter concludes with a presentation and discussion of the results obtained from the mechanical deformation experiments, with a particular focus on the determination of the thermal activation parameters for the deformation process.

4.1 Fundamentals of Plastic Deformation

4.1.1 Dislocations and Plasticity

The external shape of a solid-state body is only modifiable through the application of an external force. The process of deformation is characterised by the amount of external force F applied to the sample, the dimensions of the sample, the time t and the temperature T at which the force is applied. In uniaxial deformation, A is considered as the cross-sectional area of a solid body, and the stress that is acting on the body can be calculated as

$$\tau = \frac{F}{A}. \tag{4.1}$$

Any amount of stress applied to the body results in strain, given by the relation between the initial length l_0 and the length variation Δl due to the external force

$$\epsilon = \frac{\Delta l}{l_0}. \tag{4.2}$$

The strain consists of an elastic and a plastic contribution, according to

$$\epsilon = \epsilon_{el} + \epsilon_{plast}. \tag{4.3}$$

For small strains, the deformation process is purely elastic, and the stress that is acting on the body as a result of the applied external force is proportional to the elastic strain through the material-specific elastic or Young's modulus E yielding

$$\tau = E \cdot \epsilon_{el}. \tag{4.4}$$

In the elastic regime, the body will return to its original shape almost instantly once the external stress is removed. However, if the strain exceeds a certain value, the behaviour of stress and strain deviates from the linear regime, marking the transition to the plastic regime of deformation. Plastic deformation is non-reversible and results in a permanent shape change of the body even after the external stress is removed.

Plastic deformation of a crystalline body is carried by the displacement of neighbouring lattice planes against each other [94]. This is usually achieved through the movement of individual dislocations, which move through the body and break only individual bonds along their path. Dislocations are line defects characterised by their line direction $\vec{l}$ and Burgers vector $\vec{b}$. The Burgers vector describes the magnitude and direction of lattice distortion. Dislocations are classified as screw dislocations if the Burgers vector and line direction are parallel and as edge dislocations if they are perpendicular [95]. Mixed dislocations, where the Burgers vector is inclined with respect to the line direction, also exist.

The formation of an edge dislocation through the Volterra process is illustrated in figure 4.1. Removing an atomic half-plane from an ideal crystal lattice produces a gap in the lattice. Closing the gap and relaxing the lattice creates an edge dislocation. At the dislocation core, the lattice atoms are displaced from their original positions, resulting in a strain field that remains constant along the direction of the line.

The Burgers vector $\vec{b}$ is defined by tracing a Burgers circuit around a dislocation, as illustrated

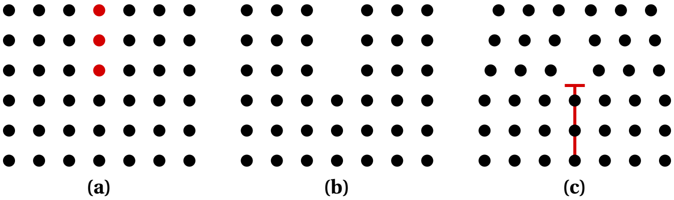

Fig. 4.1: *The Volterra Process: (a) An atomic half plane indicated in red in an ideal crystal lattice. (b) The half-plane is removed. (c) The lattice is closed, and relaxed and an edge dislocation is indicated.*

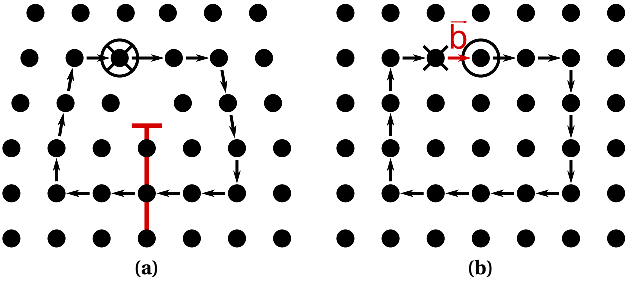

Fig. 4.2: *Definition of the Burgers vector $\vec{b}$ by means of a Burgers circuit: (a) A Burgers circuit performed around an edge dislocation with start (o) and finish (x) on the identical lattice point. (b) Burgers circuit transferred to an undistorted lattice, defining the Burgers vector as the vector required to complete the circuit.*

in figure 4.2. Connecting the lattice sites around the dislocation forms a loop with start and finish on the same lattice site. When the Burgers circuit is transferred to an undistorted lattice, as depicted in figure 4.2(b), the starting and finishing points do not coincide. The vector required to close the circuit is referred to as the Burgers vector.

The Burgers vector can be unambiguously defined through two conventions established in literature [95]:

1. The Burgers vector is taken in a clockwise direction when looking along the positive line sense or direction of the dislocation.
2. The Burgers vector runs from the finish to the start point of the reference circuit in the perfect crystal.

It is important to note that when a Burgers circuit is performed around other crystal defects, such as vacancies or interstitials, it will always form a closed loop [95].

A dislocation moving through a material causes a permanent shape change in the material through its strain field. Conversely, an external force applied to the material results in a force acting on the dislocation. The Peach-Köhler force, $\vec{K}$, acts perpendicular to the dislocation line

$$\vec{K} = \left(\vec{\sigma} \cdot \vec{b}\right) \times \vec{l}, \tag{4.5}$$

where $\vec{\sigma}$ denotes the stress tensor [94]. When a dislocation propagates along a specific plane, characterised by the Burgers vector $\vec{b}$ and the dislocation line $\vec{l}$, this is referred to as slip. The normal to this slip plane is given by the vector product of the Burgers vector $\vec{b}$ and the line direction $\vec{l}$

$$\vec{n} = \vec{b} \times \vec{l}. \tag{4.6}$$

A second type of dislocation motion is known as dislocation climb, where the dislocation moves out of its slip plane. This motion is always accompanied by a local volume change around the dislocation core, in contrast to dislocation slip. As a result, atomic movement through diffusion is required for dislocation climb, which is typically observed at elevated temperatures.

The slip plane (cf. 4.6) and slip direction, which determine the dislocation and its contribution to the plastic deformation of a material, combine to form the slip system. The shear stress acting on a dislocation of this slip system is related to the external stress through a geometric factor, the Schmid factor m_S,

$$\tau = m_S \sigma. \tag{4.7}$$

The Schmid factor is directly determined by the geometry of the slip system, as shown in figure 4.3. It is calculated using the cosines of the angles between the compression direction

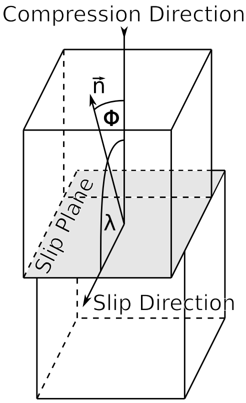

Fig. 4.3: *Relation between slip plane, slip direction and compression direction, defining the Schmid factor*

and slip plane Φ, and the angle between compression direction and slip direction λ as

$$m_S = \cos\Phi\cos\lambda. \tag{4.8}$$

As a result of this equation, the Schmid factor ranges from 0 to 0.5.
Dislocations which propagate through a material contribute to the overall shearing and straining of the material, depending on the orientation of the slip system. The strain resulting from a given dislocation density ρ of mobile dislocations in the material is given by

$$\epsilon = \rho b x, \tag{4.9}$$

where x represents the average distance travelled by a dislocation. The time derivative of this equation yields the Orowan equation,

$$\dot{\epsilon}_{plast} = \rho b v. \tag{4.10}$$

The Orowan equation describes the dynamics of the deformation process, where v represents the velocity of a dislocation. It thereby connects the important macroscopic value of the plastic strain rate $\dot{\epsilon}_{plast}$ and the microscopic entity v. The assumption of constant structure, i.e. constant dislocation density $\dot{\rho} = 0$ during deformation, is made in this equation.

4.1.2 Thermal Activation

Dislocations in a given material at a specific temperature encounter energetic obstacles that hinder their movement. These obstacles are either intrinsic, such as stress fields from other dislocations, or extrinsic, such as precipitates, point defects, or lattice friction. These obstacles limit the average velocity of the dislocations. In addition to the externally applied stress and the resulting shear stress τ, a second stress field acts on a dislocation which results from the microstructure of the material. The sum of all internal stresses τ_i, primarily the stress fields of other dislocations, impedes the movement of a dislocation and reduces the effective stress that acts on it

$$\tau_{eff} = \tau - |\tau_i|. \tag{4.11}$$

According to equation 4.5, the force acting on a dislocation line with the length $l = |\vec{l}|$ and the Burgers vector $\vec{b}$ is given by

$$K = \tau_{eff} l b. \tag{4.12}$$

If the friction stress τ_f caused by energetic obstacles is lower than the effective stress acting on the dislocation, it can propagate through the material. However, if the effective stress is

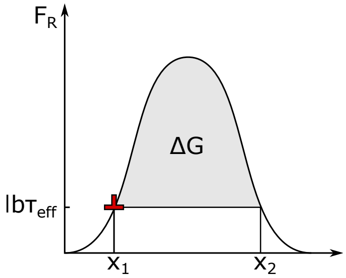

Fig. 4.4: *Schematic illustration of thermal activation with a dislocation (red) resting in a stable position x_1 in front of an energetic obstacle*

smaller than the friction stress of an obstacle in its path, the dislocation cannot overcome this obstacle and will remain in a stable position x_1 in front of the obstacle, as illustrated in figure 4.4. For temperatures above 0 K, there exists a finite probability for overcoming obstacles due to thermal fluctuations. To do so, an energy barrier, represented by the Gibbs free energy

$$\Delta G = \int_{x_1}^{x_2} dx \left(\tau_f - \tau_{eff}\right) lb \tag{4.13}$$

must be surpassed isothermally and at constant stress [96, 97]. The probability of overcoming the obstacle through thermal fluctuation is given by [98]

$$P = exp \frac{-\Delta G}{kT}. \tag{4.14}$$

If the dislocation velocity is governed by the thermal overcoming of obstacles, the process is referred to as thermally activated. The dislocation velocity is then given as

$$v = v_0 x P, \tag{4.15}$$

with the attempt frequency v_0 [99] and the distance x travelled by the dislocation when overcoming the obstacle. Using equations,4.14 and 4.15, the temperature dependence of the plastic strain rate can be expressed with the Orowan equation (4.10) as

$$\dot{\epsilon}_{plast} = \dot{\epsilon}_0 exp \frac{-\Delta G}{kT}. \tag{4.16}$$

Here, the factor $\dot{\epsilon}_0 = \rho b x v_0$ is specific to a given material and is assumed constant. The temperature dependence of ΔG at a constant strain rate is then given by

$$\Delta G = \alpha k T, \text{ with } \alpha = \ln \frac{\dot{\epsilon}_0}{\dot{\epsilon}_{plast}}. \tag{4.17}$$

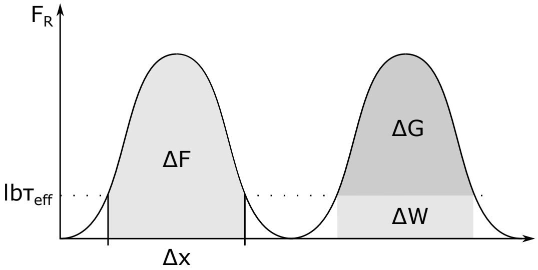

Fig. 4.5: *Schematic illustration of the relation between* ΔF*,* ΔG*,* ΔW *and* Δx

Thus, the Gibbs free energy is linearly dependent on temperature, and specifically, $\Delta G(T = 0) = 0$.

4.1.3 Thermodynamics

The contribution of thermal fluctuations to the energy required for a dislocation to overcome an obstacle is represented by the Gibbs free energy, which constitutes a portion of the total energy needed to surmount the obstacle. The total energy needed to overcome an obstacle is represented by the Helmholtz free energy

$$\Delta F = \int_{x_1}^{x_2} dx\tau_f lb = \Delta G + \Delta W. \tag{4.18}$$

ΔW represents the work term resulting from the energy supplied by the effective stress

$$\Delta W = \int_{x_1}^{x_2} dx\tau_{eff} lb. \tag{4.19}$$

Integration of this equation under the assumption of a constant effective stress ($\tau_{eff} =$ const.) yields

$$\Delta W = \tau_{eff} lb\Delta x, \tag{4.20}$$

where $\Delta x = x_2 - x_1$ represents the distance covered by the dislocation when overcoming an obstacle. The relation between all these values is depicted in a force-over-distance graph in figure 4.5.

The Gibbs free energy is determined by the temperature and effective stress. Its differential is defined as [100]

$$d(\Delta G) = -\Delta S dT - V^* d\tau_{eff}, \tag{4.21}$$

where

$$\Delta S \equiv -\left.\frac{\delta(\Delta G)}{\delta T}\right|_{\tau_{eff}} \tag{4.22}$$

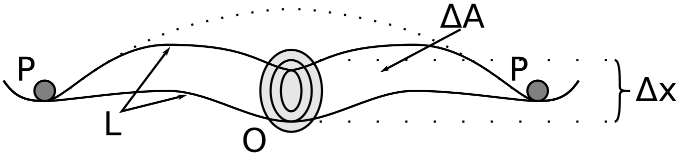

Fig. 4.6: *Schematic illustration of the area a dislocation covers during a thermal activation event*

and

$$V^* \equiv - \left.\frac{\delta\left(\Delta G\right)}{\delta\tau_{eff}}\right|_T . \tag{4.23}$$

ΔS denotes the activation entropy, which is related to the Gibbs free energy through the activation enthalpy [15]

$$\Delta G = \Delta H - T\Delta S. \tag{4.24}$$

The most significant contribution to the activation entropy arises from elastic sources, although other contributions stem from thermal expansion [101] and the formation of point defects during activation [102]. All of these contributions ultimately accumulate [103].
The geometric interpretation of V^* is shown in figure 4.6. A dislocation with line element L (l in equation 4.25), which is locked between two points P, may overcome an obstacle O via thermal activation. In this event, the dislocation moves a distance of Δx and covers a surface area ΔA. The activation volume is represented by

$$V^* = lb\Delta x = b\Delta A. \tag{4.25}$$

The comparison with equation 4.20 yields

$$\Delta W = \tau_{eff} V^*. \tag{4.26}$$

Together with equation 4.18 an important relation between the Helmholtz free energy and Gibbs free energy is revealed

$$\Delta G = \Delta F - \tau_{eff} V^*. \tag{4.27}$$

If entered into equation 4.16, the stress dependence of the strain rate is found as

$$\dot{\epsilon}_{plast} \propto exp\left(\tau_{eff} V^*\right), \tag{4.28}$$

with the activation volume itself being dependent on the stress.

4.1.4 Incremental Testing

Undertaking a deformation experiment necessitates the direct measurement of strain, strain rate, applied stress, and temperature. However, the thermodynamic parameters introduced in the preceding section cannot be directly obtained. Rather, they must be determined through the accessible values and their interdependencies. This involves making assumptions that may only hold true to a certain extent. Particularly, the assumption of constant structure in the derivatives assumed in the previous section is of critical importance. This assumption can be made when suitable experimental procedures are employed.
The experimental activation volume can be considered as

$$V = \frac{kT}{m_S} \frac{\delta \ln \dot{\epsilon}_{plast}}{\delta \sigma}\bigg|_T \tag{4.29}$$

where all values are accessible through experiments. The relationship between V and V^* (cf. 4.23) is represented by

$$V = V^* \left(1 + \frac{\delta \tau_i}{\delta \tau}\bigg|_T\right). \tag{4.30}$$

If τ_i is independent of τ, V and V^* are equivalent [104, 105]. The activation volume offers insights into the characteristics of dislocation obstacles. For thermally activated processes, obstacles and activation volume are roughly equivalent [106].
The strain rate dependence of the stress can be determined through

$$I \equiv \frac{\delta \sigma}{\delta \ln \dot{\epsilon}_{plast}}\bigg|_T. \tag{4.31}$$

With equation 4.30 it yields

$$V = \frac{ktT}{m_S I}. \tag{4.32}$$

With the relation $\dot{\epsilon}_{plast} \propto \sigma^m$ [107, 108] the stress exponent

$$m = \frac{\delta \ln \dot{\epsilon}_{plast}}{\delta \ln \sigma}\bigg|_T \tag{4.33}$$

can be determined. The stress exponent m is a creep parameter that is associated with the applied stress and depends on the microstructure and mechanical state at minimum creep rate, which are different for each starting stress. From its empirical nature, the stress exponent allows a categorisation and modelling of the deformation processes [107, 108].
The Gibbs free energy is another value that cannot be directly obtained through experimental

measurements. Only the activation enthalpy

$$\Delta H = \Delta G + T\Delta S = \Delta G - T\,\frac{\delta(\Delta G)}{\delta T}\bigg|_{\tau_{eff}} = kT^2\,\frac{\delta \ln \dot{\epsilon}_{plast}}{\delta T}\bigg|_{\sigma} \tag{4.34}$$

can be determined for $\tau_i = \text{const}$. Furthermore

$$\Delta H = kT\,\frac{\delta \ln \dot{\epsilon}_{plast}}{\delta(1/T)}\bigg|_{\sigma} \tag{4.35}$$

which then yields

$$\Delta H = -kT^2 \cdot \frac{\delta \ln \dot{\epsilon}_{plast}}{\delta\sigma}\bigg|_{T} \cdot \frac{\delta\sigma}{\delta T}\bigg|_{\dot{\epsilon}_{plast}}. \tag{4.36}$$

These equations can be employed to determine the activation enthalpy from measurement data.

4.2 Macroscopic Phenomena in Plastic Deformation

In this section, the emphasis is placed on specific aspects of plastic deformation that can be observed during the deformation of a material. The stress-strain curve and the role of dislocations in carrying deformation are central to this discussion. Building upon the fundamentals of plastic deformation, thermal activation, and incremental testing outlined in the previous section, this section delves deeper into the phenomena associated with plastic deformation.

4.2.1 Yield Strength and Anomaly

The yield point signifies the juncture on the stress-strain curve of a material at which its elastic behaviour ceases and deformation becomes non-reversible or plastic. Prior to this point, all deformation is elastic, and the material will recover its original shape upon removal of the applied stress.

Beyond the yield point, a portion of the deformation will be permanent, resulting in a non-reversible shape change. The yield point and its corresponding yield strength are material properties that depend on the crystal orientation, as specified by the Peach-Köhler equation (cf. equation 4.5) [94]. Additionally, the temperature has a significant impact on the yield strength. In most metallic materials, yield strength generally increases with decreasing temperature as the motion of dislocation is thermally activated. Dislocations can overcome obstacles with the aid of the thermal vibration of atoms and applied stress. With decreasing temperature, thermal energy decreases, leading to an increase in yield stress [109].

If a material's yield strength does not exhibit the aforementioned behaviour, and instead increases with increasing temperature, such behavior is referred to as a yield strength anomaly (YSA). This anomaly never persists across the entire temperature range from 0 K to the melting temperature, but rather occurs in a specific temperature range.

4.2.2 Serrated Flow

When a sample is subjected to deformation at a constant nominal strain rate, the total strain at any given instant in time can be expressed as the sum of elastic and plastic strain, as illustrated in equation 4.3, and in terms of the strain rate

$$\dot{\epsilon} = \dot{\epsilon}_{elast} + \dot{\epsilon}_{plast}. \tag{4.37}$$

Equation 4.37 can be rewritten as

$$\dot{\epsilon} = \frac{1}{E}\dot{\sigma} + \dot{\epsilon}_{plast}. \tag{4.38}$$

The observation of serrated flow occurs when the plastic strain rate $\dot{\epsilon}_{plast}$ surpasses the imposed strain rate $\dot{\epsilon}$. This results in a sudden increase in $\dot{\epsilon}_{plast}$ and a corresponding decrease in load. Several physical processes can give rise to serrations in the flow curve, as outlined in the following list [110]:

(i) Instantaneous increases of ρ and/or v resulting in an increase of the plastic strain rate, as expressed in equation 4.10.

(ii) Dynamic strain ageing [1] [111–114] resulting in sudden increases in both ρ and/or v.

(iii) Order-disorder transformations, as well as gradients or modulations of order in alloys that are induced by moving dislocations [115–117].

(iv) The phenomenon of continuous mechanical twinning, which is characterized by a positive temperature dependence and a negative strain rate sensitivity of the flow stress, is also observed in dynamic strain ageing. [118–120].

(v) Sudden increase in specimen temperature due to adiabatic heating usually observed in deformation at cryogenic temperatures [121–123].

(vi) Stress- or strain-induced phase transformations [124].

---

[1] Dynamic Strain Ageing is a phenomenon in which the energy barrier presented by an obstacle to a locked dislocation is augmented by the diffusion of solutes during the period of locking.

(vii) Yielding across the fracture surface as observed in brittle materials deformed under hydrostatic or triaxial non-hydrostatic pressure [125].

All of the aforementioned causes for serrations have been reported and investigated in the past. However, dynamic strain ageing, as mentioned in (ii), is the most prominent. In particular, the Portevin-LeChatelier (PLC) effect, which arises from the interaction of diffusing solute atoms and mobile dislocations, has been well-documented [111–114]. The interpretation of the stress drops in the PLC effect is based on the occurrence of a negative strain-rate sensitivity (SRS) of stress in a certain strain-rate interval, resulting in a N-shaped $\sigma(\dot{\epsilon})$ dependence [126–130]. This dependence is illustrated in figure 4.7, where the resulting deformation curves are shown alongside. When the strain rate falls within the negative SRS region (case b in figure 4.7), the deformation will oscillate between the left (slow) branch and the right (fast) branch of the N-curve, resulting in a serrated $\sigma(\epsilon)$-curve. If the strain rate is outside of the negative SRS interval, the deformation curve will appear smooth. The properties of the stress–strain rate (σ-ln$\dot{\epsilon}$) function determine the strain-rate domain of instability for a given temperature.

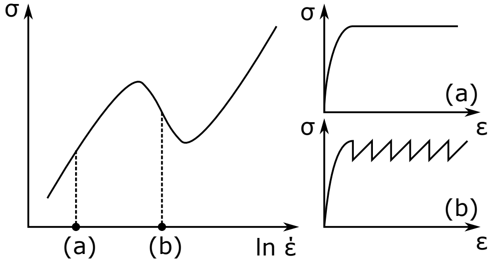

Fig. 4.7: *Schematic of the N-shaped stress–strain rate (σ-ln$\dot{\epsilon}$) function of alloys showing the PLC effect with the resulting stress-strain-curves*

The appearance of the PLC effect in a stress-strain diagram is complex due to the inherently heterogeneous behaviour of dislocations in real materials. However, several generic types of serrations have been identified [110, 131–138] for polycrystals deformed under tension, including those shown in figure 4.8. These serrations occur when the strain rate is located between the upper and lower limit of the flow stress instability. Three types of serrations can be distinguished in this regime:

- **Type A** [139] serrations exhibit periodic stress increases followed by backward drops to or even below the nominal level accompanied by quasi-continuous propagation of deformation bands along the specimen's tensile axis. Preceding a stress rise is the formation of a dislocation band at one end of the specimen, which will move through the specimen at a lower stress, which is usually accompanied by irregular stress fluctuations.

- **Type B** [140] serrations appear as more regular stress oscillations with an apparent characteristic scale and are related to the nucleation of deformation bands in neighbouring regions of the specimen with each stress drop being related to one individual band. Although these stress bands are either immobile or move only over short distances, their correlated occurrence is commonly referred to as "relay-race" or "hopping" propagation.

- **Type C** [141] serrations are characterised by deep drops below the nominal stress level (higher stress values) caused by a deformation band that are, unlike in Type B serrations, not correlated with a previous band formation. The lower the strain rate, the more random the band formation becomes.

Figure 4.8 depicts all three types of serrations as described above. The categorisation into

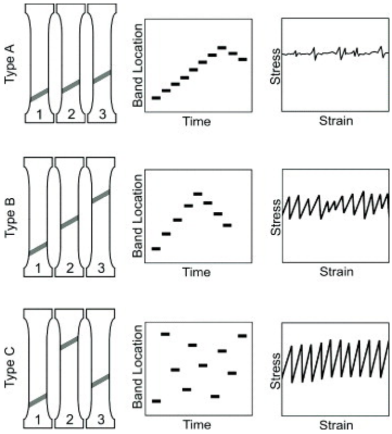

Fig. 4.8: *Schematics of motion, orientation, spatiotemporal appearances and strain-controlled tensile curve characteristics of the PLC bands [138] with 1, 2 and 3 referring to the time evolution of the sample*

three distinct types indicates the non-random nature of dislocation dynamics. However, phenomenological models based on figure 4.7 that do not take into account intrinsic strain heterogeneity are unable to explain the diverse range of deformation curves or the variations in band kinematics that occur under different experimental conditions. The complexity of irregular flow curves extends beyond a simple classification of types, and in some cases, D and E-type serrations are used to account for specific patterns observed in commercial alloys [110].

4.3 Experimental Methods

4.3.1 Sample Preparation

The deformation experiments utilized samples prepared from oriented single crystals of the CrMnFeCoNi alloy and poly-crystals of two distinct grain sizes, coarse and fine, as detailed in section 3.3.2, of the TiVZrNbHf alloy. These samples were processed via electro-discharge machining (EDM) and measured approximately 2 x 2 x 5 mm^3. The long axis of a set of CrMnFeCoNi samples was oriented in two specific directions, $[53\bar{1}]$ and [210], which were selected to promote either single-slip in the $[53\bar{1}]$ orientation or dual slip in the [210] orientation. However, such precise orientation was not achievable for the polycrystalline TiVZrNbHf samples. After being cut, each side of a sample was ground to remove the surface area affected by the EDM and finished with a 1200-grid SiC paper. Special attention was paid to ensure the perpendicularity of the cross-section and the long axis of the samples.

4.3.2 Uniaxial Deformation Machine

All deformation experiments conducted within the scope of this work were carried out utilizing a modified Zwick Z050 uniaxial deformation machine, as depicted schematically in figure 4.9. In this configuration, the deformation sample (S) is positioned between two silicon-carbide compression anvils (A). These anvils are affixed to the moveable upper and lower crosshead and the frame through alumina compression rods (F). A load cell (L) in series with the lower compression rod allows load measurements up to 10 kN with an accuracy of

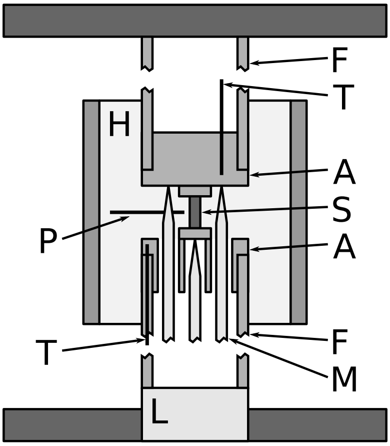

Fig. 4.9: *Schematic setup of the modified Zwick Z050 uniaxial deformation machine; detailed explanation in text.*

1 N. The current strain is measured through a linear inductive differential transducer (M) by directly measuring the length variation of the sample at the anvils using alumina rods with an accuracy of ±10 nm. For measurements at elevated temperatures, the setup can be enclosed by a cylindrical furnace (H). By means of a thermocouple (P), the temperature is directly controlled at the sample, while two additional thermocouples (T) monitor the temperature gradient within the compression anvils. Constant strain-rate experiments are computer-operated in a closed-loop control. During an ongoing experiment, incremental test procedures, as explained in the following paragraph, can be conducted.

4.3.3 Measurement Procedures

In the context of deformation experiments, strain and stress are typically defined as $\epsilon_{tech} \equiv (l_0 - l/l_0)$ and $\sigma_{tech} = F/A_0$, respectively. However, in order to obtain true values that correspond to the current dimensions of the sample being deformed, these raw values must be transferred [94]. The relationship between the true values and the current dimensions of the sample can be expressed as

$$\epsilon = \ln \frac{1}{1-\epsilon_{tech}} \tag{4.39}$$

and

$$\sigma = \frac{\sigma_{tech}}{1-\epsilon_{tech}}. \tag{4.40}$$

Stress-Strain-Curves

The stress-strain curve obtained at a constant strain rate and temperature can be analyzed for its overall form. From this curve, the yield strength and the elastic and plastic deformation portions of the entire strain range can be identified. Additionally, during the loading and unloading of the sample, the combined elastic modulus of the sample and deformation machine can be determined from the linear elastic region. In the case of a stiff machine, this value is typically quite close to the elastic modulus of the sample.

Stress Relaxation Experiments

A stress relaxation is a deformation experiment that is conducted at constant strain. In this experiment, the deformation is stopped abruptly at a constant total strain, and the stress decrease is measured as a function of time. All the relaxations that were conducted in this work have a duration of 120 s. During the experiment the total strain rate is constant, i.e. $\dot{\epsilon} = \dot{\epsilon}_{el} + \dot{\epsilon}_{plast}$, meaning that elastic strain is transferred into plastic strain ($\dot{\epsilon}_{el} = -\dot{\epsilon}_{plast}$).

According to Hooke's law, $\epsilon_{el} \propto \sigma$, and therefore, $\dot{\epsilon} \propto -\dot{\sigma}$. Using equations 4.29 and 4.33, the activation volume and stress exponent can be determined from stress relaxation experiments by

$$V = \frac{kT}{m_S} \frac{\delta \ln(-\dot{\sigma})}{\delta \sigma}\bigg|_T \tag{4.41}$$

and

$$m = \frac{\delta \ln(-\dot{\sigma})}{\delta \ln \sigma}\bigg|_T . \tag{4.42}$$

From the slope of a $\ln(-\dot{\sigma})$ over σ plot the activation volume and the slope of a $\ln(-\dot{\sigma})$ over $\ln \sigma$ plot the stress exponent can be determined, respectively.

Strain-Rate Changes

The sample is being subjected to a constant strain-rate and temperature, and it is undergoing deformation. If the strain-rate is altered by $\Delta\dot{\epsilon}$, a corresponding stress change $\Delta\sigma$ can be measured. This difference in stress is evaluated at points in the flow curve that have the same slope before and after the strain-rate change. Through this method, the differentials $\delta\left(\ln \dot{\epsilon}_{plast}\right) / \delta\sigma|_T$ and $\delta\left(\ln \dot{\epsilon}_{plast}\right) / \delta \ln \sigma|_T$ can be approximated, which allows for the determination of the activation volume and stress exponent according to equations 4.29 and 4.33.

Temperature Changes

At a constant strain rate, the sample is deformed at a temperature T_1 until a defined strain value is reached. Due to technical reasons and in accordance with equation4.34, a stress relaxation is performed, followed by unloading of the sample. The temperature is then slightly adjusted by ΔT, and the sample is reloaded at the initial strain-rate. The stress difference $\Delta\sigma$ is measured in the flow curve at points of identical slope prior to and after the temperature change. With this measurement, the temperature dependence of the flow stress $\delta\sigma / \delta T|_{\dot{\epsilon}_{plast}}$ can be determined, which, in conjunction with a stress relaxation experiment, allows for the determination of the activation enthalpy ΔH from equation 4.35. This method is based on the assumption of constant structure for small temperature changes.

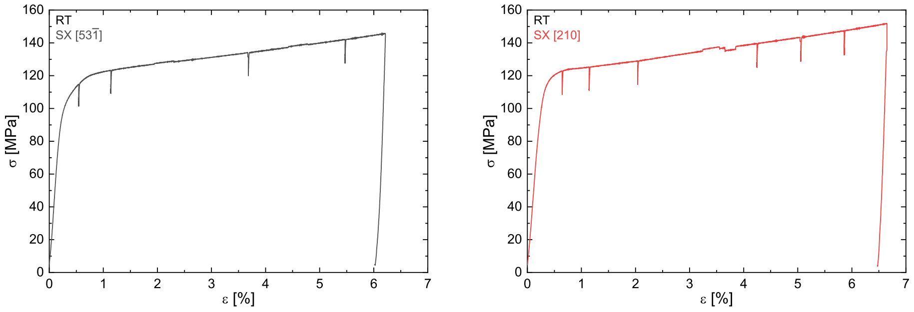

(a) **(b)**

Fig. 4.10: *Stress-strain-curves of CrMnFeCoNi deformed at room temperature along (a) [53$\bar{1}$] and (b) [210]*

4.4 Results

4.4.1 Deformation of CrMnFeCoNi

CrMnFeCoNi samples were subjected to deformation along two different crystallographic orientations, [53$\bar{1}$] and [210]. The purpose of selecting these orientations was to encourage either single-slip in the [53$\bar{1}$] samples or dual slip in the [210] samples. According to Schmid's law (cf. equation 4.8), only one slip system with a high Schmid factor of 0.49 is available in [53$\bar{1}$]-oriented fcc-crystals, namely $[10\bar{1}](111)$, and two such slip systems in [210]-oriented fcc-crystals, namely $[101](11\bar{1})$ and $[10\bar{1}](111)$, respectively.

Stress-Strain-Curves

The stress-strain curves for CrMnFeCoNi samples deformed along both orientations at temperatures ranging from room temperature to 500 K with a strain rate of $10^{-4}\,\mathrm{s}^{-1}$ have been recorded. Figure 4.10 depicts the stress-strain curves of a [53$\bar{1}$]- and a [210]-oriented sample deformed at room temperature up to approx. 6.5 % total strain.

Additionally, figure 4.11 shows a comparison of representative stress-strain curves of [53$\bar{1}$]- and [210]-oriented samples deformed at room temperature, 350 K, 400 K, 450 K and 500 K. The curves in figure 4.10 and Figure 4.11 include features of stress relaxation experiments (stress drops followed by a return to the initial stress level), strain-rate changes (stress drops or jumps to lower or higher stress levels) and temperature changes (large stress drops to $\sigma \approx 0$ MPa followed by an increase to approx. the nominal stress level before the drop), which will be further analysed in this chapter with respect to deformation orientation and temperature. The temperature dependence of the yield stress, which decreases as the

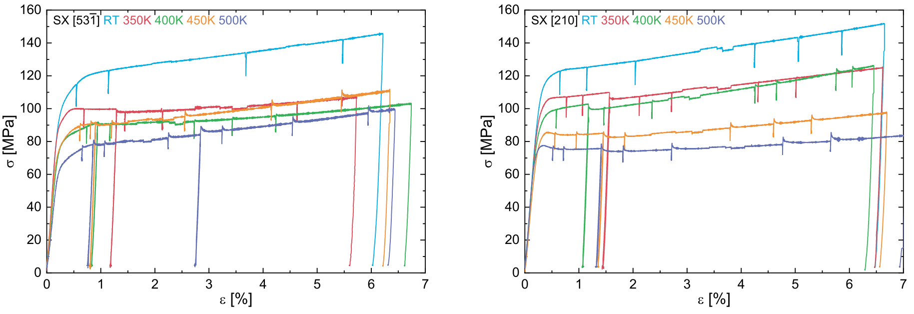

(a)

(b)

Fig. 4.11: *Stress-strain-curves of CrMnFeCoNi deformed between room temperature and 500 K along (a) [53$\bar{1}$] and (b) [210]*

temperature increases, is evident for both deformation directions. The yield stress in the [53$\bar{1}$] specimen is reduced from approx. 110 MPa at room temperature to approx. 70 MPa at 500 K and from around 120 MPa to 75 MPa, respectively, in the [210] specimen. The nearly linear decrease of the yield stress with temperature in both [53$\bar{1}$] and [210] specimens can be observed in figure 4.12. In this temperature range, the yield stress is reduced by approx. 1.5. For the [210] specimen, a minor, yet not significant, decrease in the flow stress can be observed in the attainment of the yield stress at temperatures of 450 K and 500 K.

The progression of stress values was monitored at the conclusion of each deformation as the specimen was relieved from the externally applied load. From these unloading curves, the combined Young's modulus of the CrMnFeCoNi specimen and the deformation machine was determined to be approx. 100 GPa. It is widely recognised that unloading curves provide a more precise measurement of Young's modulus than loading curves in the elastic range based on past experiences.

Stress Relaxation Experiments

Two exemplary stress relaxation experiments are shown in figure 4.13. The stress was recorded as a function of time for a [53$\bar{1}$] specimen at room temperature and 400 K, respectively, that were relaxed out of a strain rate of $10^{-4}\,\mathrm{s}^{-1}$. The stress relaxation was interrupted after two minutes, and the measurement data were plotted in the form of ln(-$\dot{\sigma}$) as a function of stress or of the logarithm of stress, respectively. The activation volume and stress exponent can be determined from the slope of the respective graphs (cf. paragraph 4.3.3). Figure 4.14 depicts the ln(-$\dot{\sigma}$) plot of a stress relaxation experiment of a [53$\bar{1}$] specimen at room temperature. For this example, the slopes were determined as I=0.47 MPa and m=58. To calculate the experimental activation volume from the stress value I, a Schmid factor of

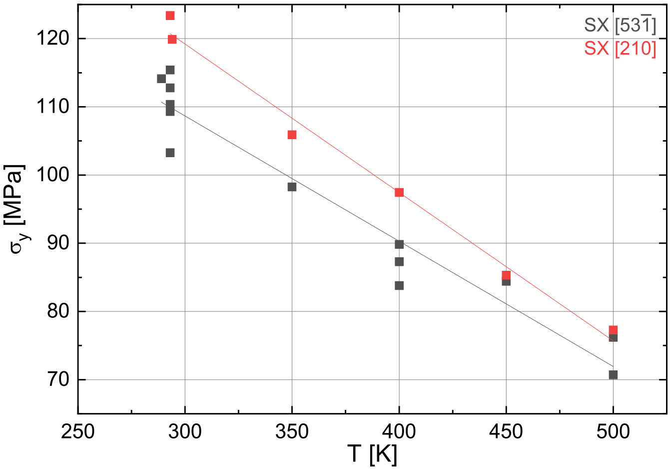

Fig. 4.12: *Yield strength over temperature for CrMnFeCoNi specimen deformed along [53$\bar{1}$] and [210]*

m_s=0.49 was used, which corresponds to the primary slip system found in the [53$\bar{1}$] and [210] specimen (cf. chapter 5.2.1). Equation 4.41 is utilized to determine the activation volume, resulting in a value of 3.68 nm^3.

Additionally, the activation volume can be determined through strain-rate changes, as described in paragraph 4.3.3, and the stress-strain curve of such a strain-rate change at 420 K in a [210] specimen is illustrated in figure 4.15. By increasing the strain rate by a factor of 1.5, the stress is increased by $\Delta\sigma$=0.8 MPa and decreased by $\Delta\sigma$=1 MPa if the strain rate is decreased by a factor of 2, respectively. Using equation 4.41, an activation volume of V=5.77 nm^3 and V=6.1 nm^3 is calculated for the individual strain-rate changes.

The experimental activation volume as a function of stress, as measured through relaxation experiments and strain-rate changes in the [53$\bar{1}$] and [210] specimen is shown in figure 4.16(a). In the [53$\bar{1}$] specimen, the activation volume ranges from 3.3 nm^3 up to 29.1 nm^3. The activation volume of the [210] specimen ranges from 3.5 nm^3 up to 30 nm^3. A distinctive stress dependency of the activation volume is clearly visible, following a hyperbolic shape. Figure 4.16(a) also displays the results of the strain-rate changes (open circles), which are in remarkable agreement with the results of the relaxation experiments.

Temperature Changes

Temperature change experiments were routinely conducted in conjunction with stress relaxation experiments. Figure 4.17 illustrates a temperature change experiment on a [210] specimen. The specimen was subjected to a constant strain rate until a steady hardening rate

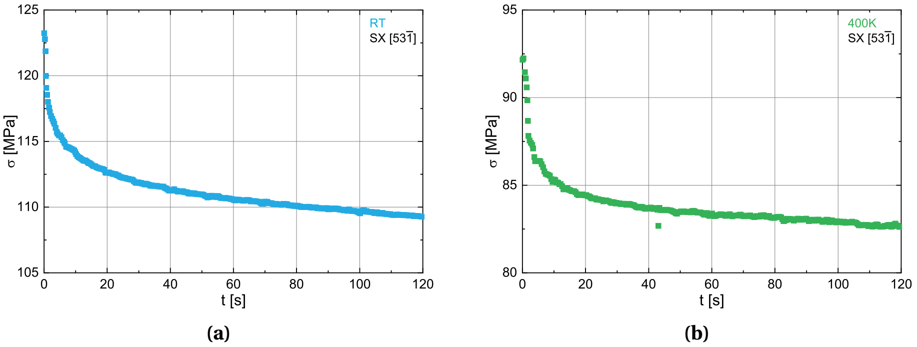

Fig. 4.13: *Stress relaxation in deformation experiments of [53$\bar{1}$] specimen at (a) room temperature and (b) 400 K*

was achieved. At this point, a stress relaxation (perpendicular curve progression at ϵ=1.17 %) was performed, after which the specimen was immediately unloaded. The temperature was then elevated by 20 K, resulting in a decrease in flow stress. A second relaxation was conducted at the point similar slope on the stress-strain curve, which corresponded to a strain of ϵ=1.46 %.

In figure 4.18, the temperature change results ($\Delta\sigma/\Delta T$) are depicted as a function of the temperature. The values of $\Delta\sigma/\Delta T$ are related to the geometric mean temperature of the individual temperature changes [142]. With equation 4.36, the activation enthalpy of the plastic deformation process can be calculated from $\Delta\sigma/\Delta T$. The factor $\frac{\delta \ln \dot{\epsilon}_{plast}}{-\dot{\sigma}}$ was calculated from the average values of the stress relaxations conducted before and after a temperature change. The activation enthalpy for both the [53$\bar{1}$] and [210] specimen is depicted in figure 4.19. For both deformation directions, comparable values for the activation enthalpy ranging from approx. 1.4 eV at 360 K to approx. 3.4 eV at 560 K were observed. The activation enthalpy exhibits a linear dependence on the temperature with a slope of $4.8 \cdot 10^{-3}$ eV/K for the [53$\bar{1}$] orientation and $6.5 \cdot 10^{-3}$ eV/K for the [210] orientation, respectively, and zero intercept at T=0 K. This linear relationship is illustrated in figure 4.19 as a solid line originating from E=0 and T=0.

An additional value is presented in figure 4.19 in ΔW, the work term. By neglecting the internal stresses, the work term can be determined by $\Delta W = \tau_{eff} V^* \approx \tau V = kT\sigma \cdot \delta \ln(-\dot{\sigma})/\delta\sigma$. In the investigated temperature range, the work term displays similar values and a comparable linear behaviour as the activation enthalpy for both the [53$\bar{1}$] and [210] specimens, respectively.

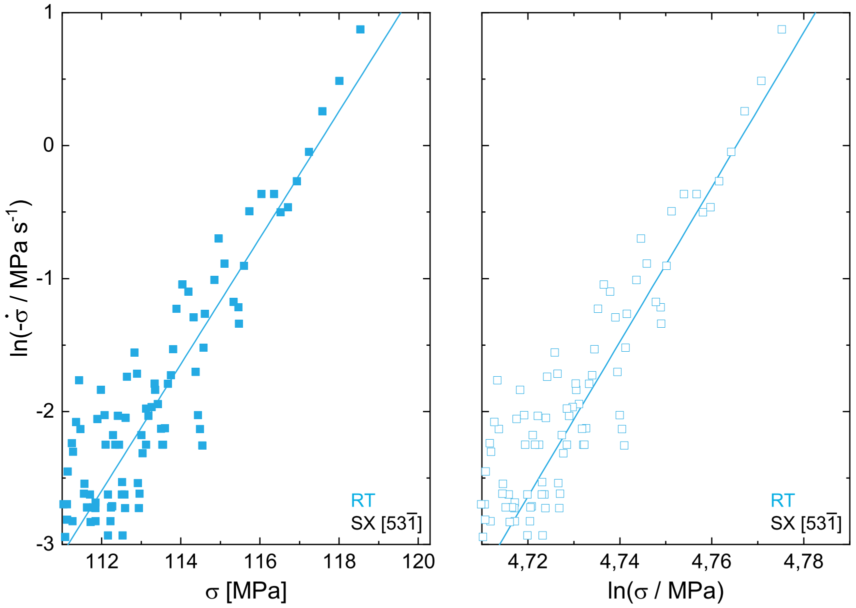

Fig. 4.14: *Determination of (a) the activation volume and (b) the stress exponent of a* $[53\bar{1}]$ *specimen at room temperature*

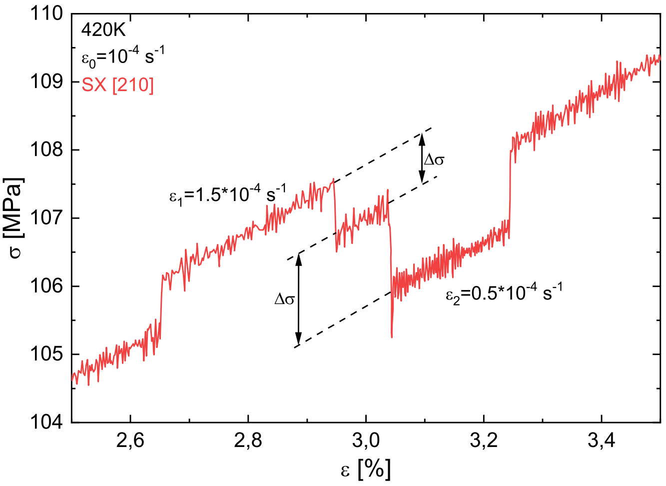

Fig. 4.15: *Strain-rate changes in [210] specimen at 420 K. The strain rate is increased and decreased by a factor of 2*

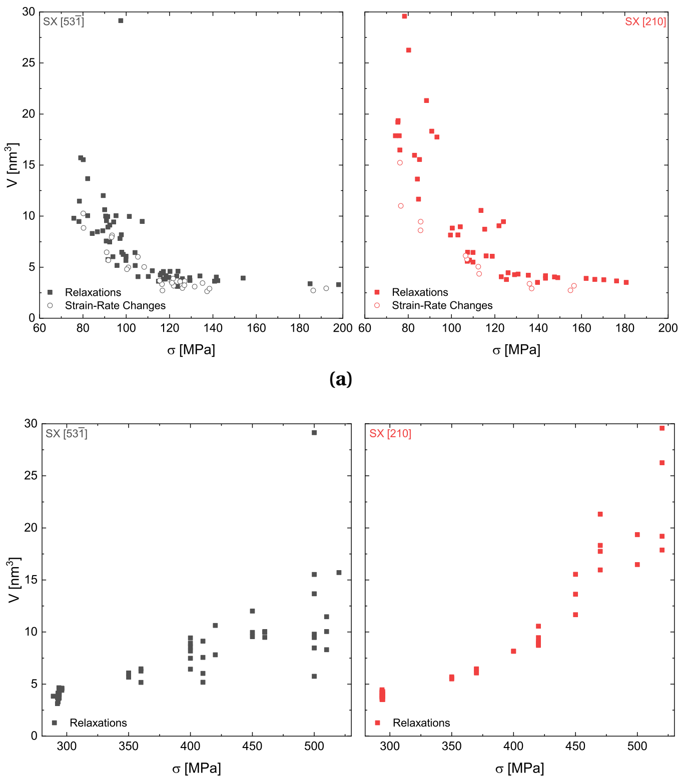

(a)

(b)

Fig. 4.16: *Activation volume of CrMnFeCoNi as a function of stress. Results of stress relaxations and strain-rate changes are shown*

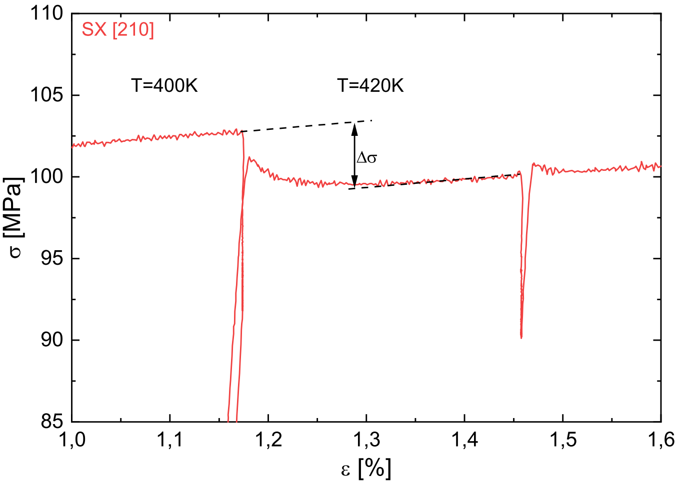

Fig. 4.17: *A temperature change accompanied by a stress relaxation in a [210] specimen. A temperature increase of 20 K results in a stress decrease of* $\Delta\sigma = 4.2$ *MPa*

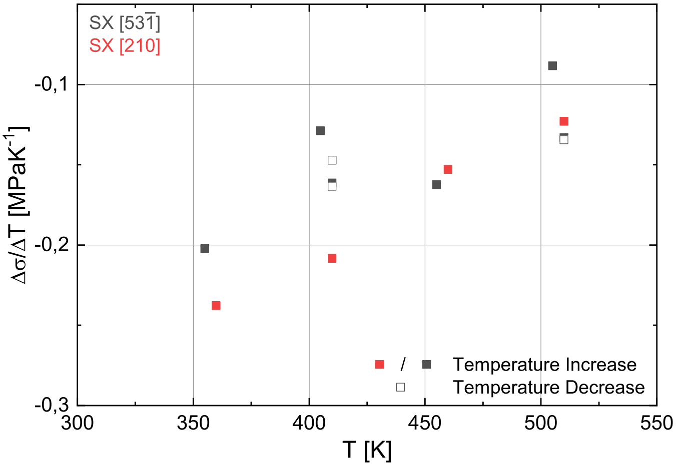

Fig. 4.18: *Results* $\Delta\sigma/\Delta T$ *of the temperature changes for temperature increases and decreases in [53$\bar{1}$] and [210] specimen*

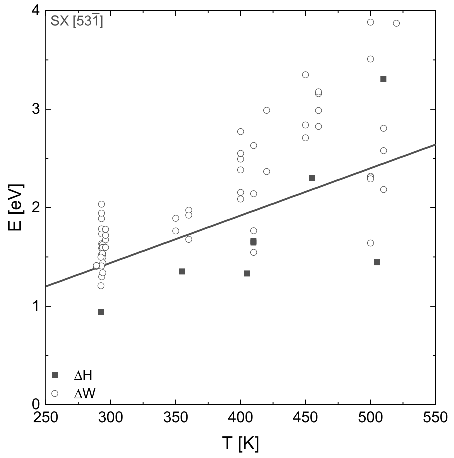

Fig. 4.19: *Temperature dependence of the activation enthalpy ΔH and the work-term ΔW of [53$\bar{1}$] and [210] CrMnFeCoNi specimen*

4.4.2 Deformation of TiVZrNbHf

Stress-Strain-Curves

Deformation experiments were carried out on TiVZrNbHf at temperatures ranging from room temperature to 1150 K, with a standard strain rate of $10^{-4}\,\mathrm{s}^{-1}$. Figure 4.20(a) displays three characteristic stress-strain-curves of fine grained TiVZrNbHf that were measured in the examined temperature range. The stress-strain curves for TiVZrNbHf alloy exhibit a smooth transition between the elastic and plastic regions, with no significant work-hardening observed during plastic deformation up to a strain of 4.5 %. The stress-strain-curve depicted

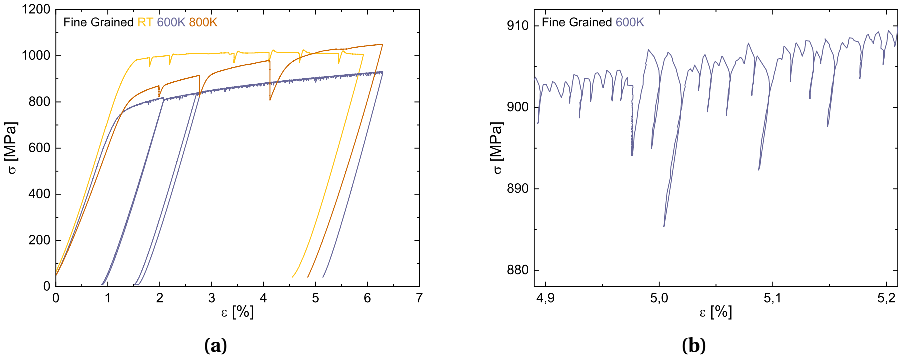

(a) **(b)**

Fig. 4.20: *Characteristic stress-strain curves of fine grained TiVZrNbHf (a) deformed at room temperature, 600 K and 800 K and (b) detail of the deformation curve of the 600 K specimen*

in figure 4.20(a) exhibits stress relaxations (stress drops followed by a return to the initial stress level), with a slight stress overshot upon reloading. Strain-rate changes (stress drops or jumps to lower or higher stress levels) performed between 2-3 % strain have minimal effect on the flow stress.

In the intermediate temperature range of 500-750 K, the stress-strain curves exhibit a smooth transition from the elastic to the plastic regime, with a moderate hardening behaviour. Two temperature changes are visible at 1.5 % and 2 % strain, with little influence on the flow stress in this temperature range. Similarly, strain-rate changes have no significant influence on the flow stress. Figure 4.20(b) provides a detailed section of the deformation curve of the 600 K specimen between 4.9 % and 5.2 % strain, revealing stress fluctuations that occur parallel to the elastic loading segment in intervals of approximately 0.03 %. These stress instabilities are present in all specimens deformed in the intermediate temperature regime but absent in the low or high-temperature regime.

At temperatures above 750 K, TiVZrNbHf exhibits a high-temperature behaviour with a smooth transition between the elastic and plastic regimes, as shown in figure 4.20(a) by a specimen deformed at 800 K. The hardening rate is higher compared to the low and intermediate temperature regimes, and stress relaxations result in a considerable reduction of stress. The combined Young's modulus for the TiVZrNbHf specimen and the deformation machine was determined to be approximately 750 GPa based on the unloading curves at the end of each deformation. The stress-strain curves of the fine-grained (grain size 300-500 μm) and coarse-grained (grain size approx. 1 mm) TiVZrNbHf samples were found to be qualitatively and quantitatively similar.

The yield stress as a function of temperature determined between room temperature and 1150 K is depicted in figure 4.21. The yield stress as a function of temperature for the TiVZrNbHf samples was determined to decrease linearly between room temperature and approximately 500 K and above 850 K with a rate of about 1.05 MPa K^{-1} (dashed line). Between 500 K and 800 K, however, the yield stress increased with temperature. The temperature dependence of the yield stress was found to be slightly more pronounced in the coarse-grained material, and at 800 K, the yield stress of the coarse-grained material was approximately 10 % higher than that of the fine-grained material.

Stress Relaxation Experiments

Figure 4.22 illustrates the exemplary stress relaxations for the three characteristic temperature regimes. The stress data is plotted as a function of time and has been scaled to the initial value of each relaxation. In the low temperature regime, represented by a room temperature relaxation, the stress decreases moderately by about 5 % over the whole relaxation

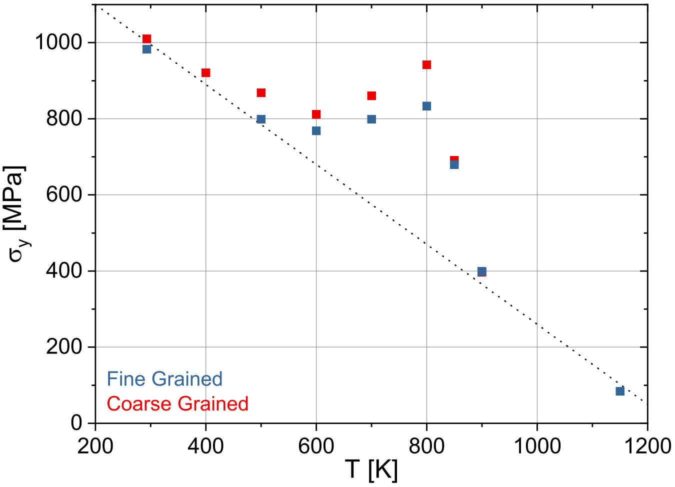

Fig. 4.21: *Yield stress over temperature for fine and coarse grained TiVZrNbHf specimen*

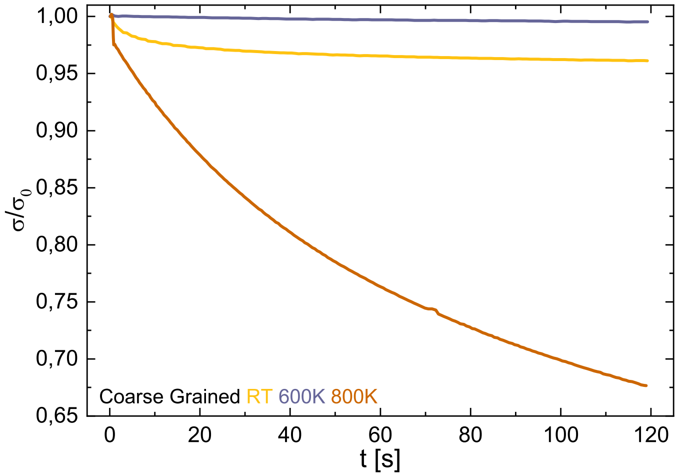

Fig. 4.22: *Stress relaxation curves normalised to the initial stress value of coarse grained TiVZrNbHf at three characteristic temperatures*

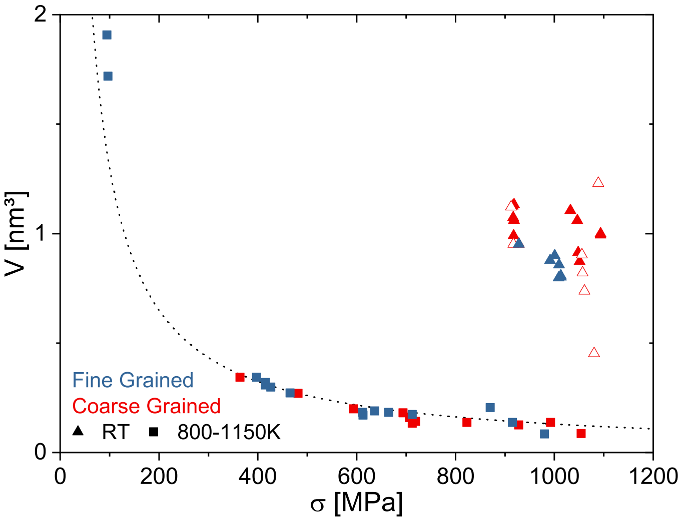

Fig. 4.23: *Stress dependence of the activation volume of fine and coarse grained TiVZrNbHf in the high (squares) and low (triangles) temperature regime. Solid squares and triangles mark stress relaxations, empty triangles strain-rate changes*

time and exhibits a logarithmic behaviour characteristic to metallic materials [143]. In the high temperature regime, represented by an 800 K relaxation, a qualitatively similar time dependence is observed, although the stress decrease amounts to approximately 35 % after 120 s. The relaxation at 600 K, representing the intermediate temperature regime and corresponding to the yield stress anomaly (cf. figure 4.21), exhibits a noticeably different behaviour with the stress remaining essentially constant over the entire relaxation duration. The behaviour of the individual stress relaxations is also reflected directly in the stress-strain curves in figure 4.20(a), where the vertical drop in stress resulting from the relaxations is clearly distinguishable at room temperature and very distinct at high temperature, but hardly recognisable in the intermediate temperature regime, even in the detail plot in figure 4.20(b). Using the procedures described in paragraph 4.3.3 and already applied for the CrMnFeCoNi alloy, the activation volume of the TiVZrNbHf alloy was calculated (cf. also equation 4.41 and Schmid factor m_s=0.49). Figure 4.23 depicts the activation volume of TiVZrNbHf, which was derived from both stress relaxation experiments and strain-rate changes in fine and coarse-grained specimens, respectively. Triangles represent the activation volumes determined in the low temperature regime, while squares indicate results obtained in the high temperature regime. In the high temperature regime, the activation volume was found to be approximately 1.8 nm^3 at low stresses and 0.1-0.4 nm^3 at stresses above 400 MPa. In this temperature range, the activation volume exhibits a hyperbolic dependence on the

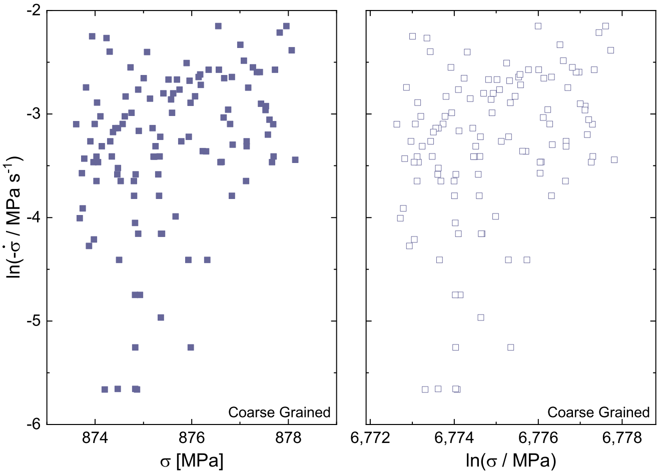

Fig. 4.24: *Depiction of the non-logarithmic behaviour during stress relaxations of TiVZrNbHf in the intermediate temperature regime*

stress (dashed line). No systematic difference between the values obtained for the fine and coarse-grained specimens was observed within the experimental scatter.

In the low temperature regime, the activation volume was measured to be around 1 nm^3. Due to the limited stress range accessible through the experimental setup, only stress values between 900 and 1100 MPa could be investigated, yielding essentially constant activation volumes with a slight tendency to decrease with increasing stress. Once again, no significant difference between fine and coarse grained specimens was observed. The values obtained from strain-rate changes (represented by open triangles) in the low temperature regime are in good agreement with those from stress relaxations.

In the intermediate temperature range, the evaluation of the stress relaxation data is not possible due to the almost non-existent stress drop and the non-logarithmic behaviour of the stress relaxation curve, as shown in figure 4.24. It is evident from the data that the strain-rate sensitivity of the flow stress is exceedingly small. This conclusion is further substantiated by the lack of a discernible change in flow stress despite varying strain-rate conditions in the intermediate temperature range.

The stress exponent was determined from the relaxation experiments, as per equation 4.42. In the high-temperature regime, values of 4.0 to 4.7, with an average of 4.4, were obtained for both fine and coarse-grained specimens. In the low-temperature regime, large values between 90 and 110 were obtained. However, in the intermediate temperature range, no stress exponent could be determined due to the stress drop being almost non-existent and not exhibiting logarithmic behaviour, as observed in figure 4.24.

Temperature Changes

The determination of the activation enthalpy of deformation in TiVZrNbHf was achieved through the measurement of the difference in flow stress before and after an increase in temperature. Figure 4.25 shows the activation enthalpy in the temperature range of 800 K to 900 K, where the temperature change experiments allowed a reasonable interpretation of the data. In this temperature range, absolute values of 0.4-3.1 eV, with an average of 2.0 eV, were obtained for the activation enthalpy. No significant temperature dependence of the activation enthalpy was observed between 800-900 K, and the difference between fine and coarse grained specimens was negligible. However, no values for the activation enthalpy could be determined for the intermediate temperature regime since no activation volume could be obtained from the stress relaxations, and the temperature changes did not result in a significant change in the flow stress (cf. figure 4.20).

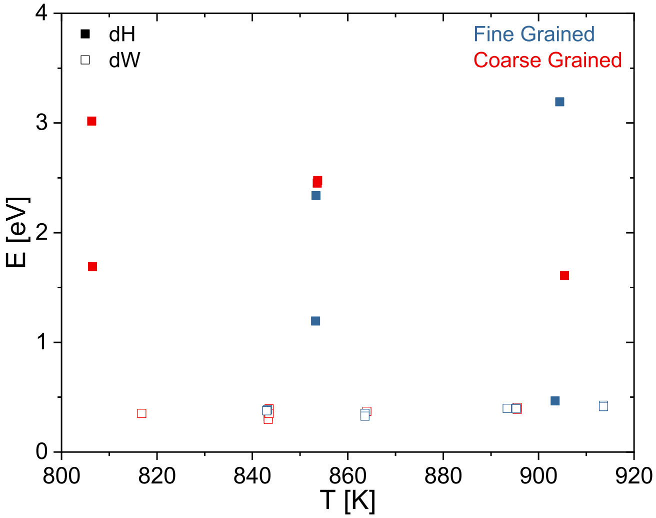

Fig. 4.25: *Temperature dependence of the activation enthalpy* ΔH *and the work-term* ΔW *of TiVZrNbHf*

In addition to the activation enthalpy figure 4.25 displays the work-term (ΔW), which was determined from the stress relaxations between 800-900 K. The work term generally showed values of approximately 0.3-0.5 eV, with no significant temperature dependence or difference between the fine and coarse-grained TiVZrNbHf specimens observed.

4.5 Discussion

The results of the macroscopic deformation of single crystalline CrMnFeCoNi and polycrystalline TiVZrNbHf are evaluated and discussed in this section. The discussion of the outcomes of microscopic investigations of plastically deformed CrMnFeCoNi and TiVZrNbHf can be found in chapter 5.

4.5.1 Deformation of CrMnFeCoNi

The mechanical properties of single-crystalline CrMnFeCoNi were investigated in the temperature range between 293 K and 500 K. With a melting temperature of 1627 K (cf. section 3.2), the high-temperature limit of the investigation corresponds to a homologous temperature of 0.31. Compression tests were conducted up to strains of 5 to 7 % with a focus on thermodynamic activation analysis. The experiments were not designed to determine the ductility limits of the material. The mechanical properties of the material were determined for two distinct crystallographic orientations, i.e. $[53\bar{1}]$ and [210], along which the material was deformed in order to promote single slip or provoke the activation of two slip systems. The yield stress of CrMnFeCoNi, depicted in figure 4.12, was found to depend slightly on the crystal orientation during deformation. The CRSS was calculated using the Schmid factor determined through TEM investigations (cf. chapter 5.2.1 and table 5.3), yielding values between 50 and 55 MPa for samples deformed along $[53\bar{1}]$ and approximately 57 MPa for samples deformed along [210], respectively. These values are considerably close to each other. Previous studies have reported CRSS values of 42-45 MPa [43] and 70 MPa [45], both in compression and 53-60 MPa [44], 80-82 MPa [40, 46] and 44 MPa [47], all in tension, for single crystal deformation of CrMnFeCoNi. The scatter in CRSS values has been attributed to differences from the exact equiatomic composition ([40, 44–46]) or the microstructure ([43]). Kawamura et al. [43] assert that the presence of a dendritic microstructure in a single crystal can significantly increase the CRSS. They speculate that sub-grain boundaries within the dendritic microstructure obstruct dislocation motion, resulting in a scattering of CRSS values. Kawamura et al. [43] observed that by growing single crystals at a withdrawal rate of 40 mm/h and subsequently annealing them at 1473 K for 96 h, they were able to produce crystals without a dendritic microstructure. However, Patriarca et al., Abuzaid et al., Kireeva et al. and Wu et al. [40, 44–46] did not report on the microstructure of the single crystals they deformed. The CRSS values determined by Kawamura et al. [43] are in agreement with estimates from previous studies that used polycrystal [31, 35, 144] and micropillar deformation [39].

The CRSS values determined in this work for CrMnFeCoNi are consistent with those reported by Abuzaid et al. [44] and are reasonably consistent with the values determined by Kawamura et al. [43] and estimates from polycrystal [31, 35, 144] and micropillar deformation [39]. The slight overestimation of the CRSS in this work is consistent with the argument put forth by Kawamura et al. [43] due to the presence of dendrites (cf. figure 3.11) and sub-grain boundaries (cf. figure 3.12) in the as-grown state of the single crystals and their close to equiatomic composition (cf. 3.2.3).

Kawamura et al. [43] showed that the CRSS is independent of the sense of loading (tension or compression), indicating that dislocations in this HEA behave normally, similar to conventional *fcc*-metals and alloys. A comparison of the flow (yield) stress to conventional *fcc*-alloys, such as Cu-2Al [145], Cu-5Al [145], Cu-30Zn [146], reveals that they are quantitatively similar to each other.

Scaled to the Burgers vector the activation volume (cf. figure 4.16) ranges from approximately 200 b^3 at room temperature to 1000 b^3 at 500 K for samples deformed along $[53\bar{1}]$ and from approximately 200 b^3 to 1200 b^3 at 500 K for samples deformed along [210]. The strong temperature dependence of the activation volume can be observed in figure 4.16(b). Considering the role of rate-controlling, localized obstacles, the significant decrease in the activation volume with stress can be explained as follows: With increasing stress, the number of obstacles that the dislocation line touches grows. As a result, the distance between the contact points decreases, leading to a shorter mean length of a dislocation segment relevant for a single thermal activation event [147]. Consequently, the activation volume decreases, as per equation 4.25. Similarly, the increase in the activation volume with temperature, as observed in figure 4.16(b) can be attributed to higher mean thermal energy required to overcome obstacles at higher temperatures. The increasing Δx in equation 4.23 leads to an increase in the activation volume [148]. It is important to note that both representations of the activation volume are intrinsically related [149]. Since the activation volume is related to the area swept by a dislocation during an activation event, as illustrated in figure 4.6 and equation 4.25, it is possible to derive the underlying mechanism of activation from the values of the activation volume. Small values are observed for the kink pair mechanism (extension of the dislocation line across the Peierls maximum), larger ones for dislocation solute interactions (diffusion of solute atoms influencing the stress field of the dislocation), and very large values for the forest mechanism (interaction of stationary and mobile dislocations) [150], without reference to CrMnFeCoNi.

The values for the activation volume determined in this work are consistent with the values reported by Kawamura et al. [43], for room temperature, they report 232.7 b^3. However, at higher temperatures, the values determined in this work are significantly different from those reported by Kawamura et al. [43], who reported an activation volume of approximately 500 b^3 at 500 K. Zhou et al. [47] studied the influence of annealing times and temperatures on the mechanical properties of single-crystalline CrMnFeCoNi and reported an activation volume at room temperature of 202±42 b^3 after annealing for 1 week at 1000 °C and 192±42 b^3 at 1200 °C, respectively. These values are in good agreement with the values determined in this work. Other studies have reported activation volumes at room temperature of 360 b^3 (Laplanche et al. [151]) and 36-87 b^3 (Moon et al. [152]). Laplanche et al. [151] obtained their values from strain-rate jump tests on polycrystalline CrMnFeCoNi and found that the activation volume decreases with increasing strain due to the introduction of forest dislocations. Forest dislocations or a forest of stationary dislocations pose obstacles to mobile dislocations [153]. When cutting through the forest dislocations, the mobile dislocation becomes increasingly jogged, reducing its mobility, increasing the stress, and reducing the activation volume [154]. The decrease can be minimized when performing measurements in the easy glide region (up to approx. 10% strain), as reported by Kawamura et al. [43]. This is only possible when investigating single crystals, as poly-crystals lack a region of easy glide due to hardening starting almost immediately after yielding. The activation volume obtained from samples deformed at room temperature in the present work is relatively strain-independent (in the region between 120 and 200 MPa, cf. figure 4.16), which is consistent with the report by Kawamura et al. [43]. Following their argumentation, it can be assumed that no short-range order is present in the alloy or that a possibly existing short-range order does not significantly affect the flow stress. This line of argumentation is supported by Zhou et al. [47], who showed that the mechanical properties of CrMnFeCoNi single crystals remain essentially constant even after considerable annealing times (1 week at 1200 °C and subsequently 1 week at 1000 or 1200 °C).

The values for the activation enthalpy ΔH and the work term ΔW, as depicted in figure 4.19, are derived from temperature changes and relaxations. It is unusual that both the activation enthalpy and work term have similar values, given that plastic deformation is considered a thermally activated process, as described in previous works [155, 156]. This raises the question of whether the deformation of CrMnFeCoNi is truly a thermally activated process and whether the analysis presented in this work is applicable to this deformation process. To the best of the author's knowledge, this effect has not been previously reported, and further investigation is necessary to fully understand its implications for the deformation characteristics of CrMnFeCoNi.

The present study has comprehensively examined the mechanical properties of single-crystal CrMnFeCoNi at temperatures ranging from room temperature to 500 K. The CRSS and activation parameters for plastic deformation up to 10 % strain have been determined for a single-slip and dual-slip orientation, providing a detailed picture of these values up to intermediate temperatures. This allows for direct comparison between these specific deformation cases and extends beyond previous reports, which only focus on low-index or single-slip orientations. It is noteworthy that similar values for the activation enthalpy and work term have not been observed before, raising the question of whether the deformation processes are thermally activated. Despite the detailed picture provided, the mechanical properties of CrMnFeCoNi show no unique characteristics that differentiate it from simpler *fcc* alloys, given its perfect solid solution microstructure.

4.5.2 Deformation of TiVZrNbHf

The deformation properties of polycrystalline TiVZrNbHf were examined in a temperature range spanning from room temperature to 1150 K. Given the melting point of TiVZrNbHf at 1863 K [61], the high-temperature limit of the tests corresponded to a homologous temperature of 0.62. The experiments were conducted in compression, with a focus on thermodynamic activation analysis, up to strains of 6 to 8 %. The aim was not to determine the ductility limit of the material.

The yield stress of polycrystalline TiVZrNbHf varies from approximately 1 GPa at room temperature to about 90 MPa at 1150 K. The striking characteristic of the plasticity of TiVZrNbHf is the presence of a yield-stress anomaly (YSA) in the temperature range of 500 K to 800 K. In this range, the yield stress increases with increasing deformation temperature, which is considered anomalous behaviour for metallic materials. However, outside this temperature range, a normal decrease in yield stress with increasing deformation temperature is observed. YSAs have previously been reported in several ordered intermetallic alloys such as Ni-Al, Cu-Al, Cu-Zn and Ti-Co, as well as in disordered alloys and pure metals [157]. To the best of the author's knowledge, a yield stress anomaly has not been previously reported for a single-phase HEA.

In the intermediate temperature regime between 500 and 800 K, the stress-strain curves exhibit notable fluctuations in the flow stress, which are absent in the low- and high-temperature ranges where the curves are smooth. This observation suggests the presence of flow-stress instability, leading to serrations in the flow stress within that specific temperature range. Although the feedback loop controlling the flow stress may exhibit noisy behaviour under the given experimental conditions of stress and temperature, it is difficult to make a definitive statement regarding the cause of the observed flow-stress variations. However, the sum of the experimental results suggests that these serrations are an actual effect of deformation rather than a consequence of the feedback loop control.

1. The stress increments remain consistent throughout the deformation and are observed after each regular strain increment.

2. The flow stress decreases in parallel with the elastic unloading curve of the specimen.

3. Stress fluctuations are observed in the same temperature range where an extremely low strain-rate dependence of the flow stress occurs.

4. No stress variations are observed in either the low or high temperature regime despite similar stress values.

As mentioned earlier, this work has identified three distinct temperature regimes that are characteristic to the deformation of poly-crystalline TiVZrNbHf. These temperature regimes are not only evident in the yield stress, but also in the material's response to stress-relaxation, strain-rate, and temperature changes, as well as the smoothness of the stress curve. The following paragraphs will delve into the specific characteristics of each temperature regime in greater detail.

Low-temperature regime

In the low-temperature regime, ranging from 293 K, to 400 K, the yield stress decreases with increasing deformation temperature, which is the regular behaviour for metals and most metallic alloys. Notably, in this temperature range, the difference in yield stress between coarse-grained and fine-grained specimens is almost negligible. In the stress-strain curves of all specimens, coarse and fine grained, deformed in this temperature regime, a characteristic overshoot of the flow stress after each reload from a stress relaxation is observed. During the stress-relaxation experiments, the stress declines in a regular logarithmic fashion. The activation volume in this temperature regime has values of about 1 nm^3, regardless of the grain size of the deformed specimen, with the stress exponent exhibiting values in the order of 100. The material exhibits appreciable stress response upon strain-rate changes, the response corresponding to the activation volume determined by the stress-relaxations. Overall, the stress-strain curves, i.e. the flow stress, appear smooth without artefacts.

Intermediate temperature regime

The intermediate temperature regime, ranging from approx. 400 K to 800 K, exhibits a yield-stress anomaly in which the yield stress remains constant or increases with rising temperature. In this temperature range, the yield stress of coarse-grained specimens tends to be about 10 % higher than that of fine-grained specimens (cf. figure 4.21). The flow stress of TiVZrNbHf specimens deformed within this temperature range remains largely unaffected by changes in strain rate or temperature. Following a brief initial drop resulting from stress relaxations, the flow stress remains essentially constant. Specimens deformed within a narrower temperature range, between 500 K to 700 K, within the intermediate temperature range display a serrated flow stress, in contrast to specimens deformed outside this temperature range.

High-temperature regime

In the high-temperature regime above approximately 800 K, the yield stress decreases with increasing temperature and shows little to no dependence on grain size. During stress relaxations, the stress decreases in a consistent logarithmic manner comparable to the low-temperature regime but with a stronger decline relative to the initial value at the beginning of the relaxation experiment. The activation volume exhibits a hyperbolic behaviour, reaching values of approximately 1.8 nm^3 at 100 MPa and approximately 0.1 nm^3 at 1 GPa. The stress exponent (cf. equation 4.33)has a value of approximately 4.4. In this temperature range, the flow stress displays significant responses to changes in strain rate and temperature. The activation enthalpy is calculated to be around 2.7 eV, with no discernible dependence on the grain size of the deformed specimen. Overall, the stress-strain curves, i.e. the flow stress, appear smooth without any distinct features.

The high-temperature flow stress exhibits a strong temperature dependence, resulting in a broad range of investigable stresses that allow for the determination of the stress dependence of the activation volume. By fitting the activation volume data to a hyperbolic function (dashed line in figure 4.23) using a single parameter, the best fit is obtained at 164 nm^3/MPa. As stress and activation volume are directly related [104], it is possible to convert the fit parameter into a stress exponent, yielding a value of 5.95. This value is in reasonable agreement with the stress exponent determined directly from stress-relaxation experiments in the high-temperature regime (4.4). A hyperbolic function calculated using a stress exponent of 100 produces a curve that is consistent with the activation volume values determined in the low-temperature regime (shown in figure 4.23) despite the much smaller range of stress values available in that regime. This finding supports the consistency of the experimental data and the applied analysis.

The observed stress exponent of 4.4 in the high-temperature regime is consistent with frequently reported values for metallic materials. In contrast, the stress exponent of 100 observed in the low-temperature regime is much larger and suggests that a simple power law description of the deformation behaviour is not appropriate for this temperature range. The limited temperature range and the minimal temperature dependence of the flow stress within the low-temperature regime make it impossible to adequately assess the influence of stress on the activation volume. Due to the constraints of the experimental setup, an extension of the temperature range to lower temperatures was not feasible, and even if it were, it would not have resulted in a reduction of the stress range to lower values.

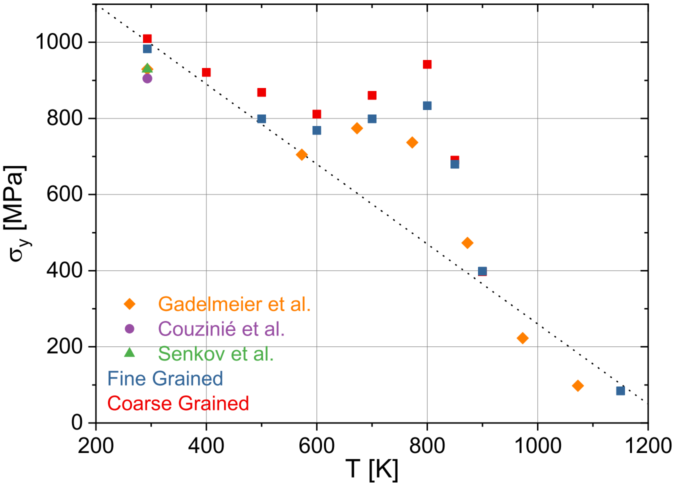

Fig. 4.26: *Yield stress over temperature of TiVZrNbHf as obtained in the present work (squares) compared to data obtained by Gadelmeier et al. [158] (diamonds) and data obtained for TiZrNbHfTa by Couzinié et al. [53] (circle) and Senkov et al. [159] (triangle)*

Previous research on the plasticity of TiVZrNbHf polycrystals was conducted by Fazakas et al. [58], who subjected polycrystalline samples to compression at a strain rate of $5 \times 10^{-4}\,s^{-1}$ at room temperature. They observed high ductility in the material, with up to 40 % strain for specimen heat-treated at 1173 K, and reported a yield stress of 1400 MPa. The yield stress reported by Fazakas et al. is substantially higher than that measured in the present work, which may be attributed to the higher strain rate used in their investigation. Tensile deformation tests conducted by Gadelmeier et al. [158] on as-grown TiVZrNbHf samples are in agreement with the data obtained in the current work and confirm the presence of a YSA within the temperature range of 400 to 800 K. A comparison of the data by Gadelmeier et al. and the present work is depicted in figure 4.26. Previous research has investigated the plastic deformation behaviour of various refractory HEAs, including TiZrNbHfTa. Senkov et al. [159] investigated the deformation behaviour of equiatomic TiZrNbHfTa polycrystals, which is similar to the TiVZrNbHf alloy studied in the present work through the substitution of Ta and V. However, despite this similarity, the plastic properties of the two alloys differ significantly, with the yield stress for TiZrNbHfTa decreasing over the entire investigated temperature range from 293 K to 1473 K, without any indication of a temperature-induced change in the deformation mechanism. Feuerbacher et al. [54] report similar results for the TiZrNbHfTa HEA for a smaller temperature range between 293 and 573 K. They also observed stress overshoots at low temperatures during the reloading of a specimen, which were also observed during low-temperature reloading of TiZrNbVHf in the present work (cf. 4.20). Couzinié et al.

[53] conducted stress-relaxation experiments to determine the activation volume for the room temperature plasticity of the TiZrNbHfTa HEA. They reported a yield stress of 905 MPa and an activation volume of 42 to 48 b^3 for strains between 1 and 3 %, where the activation volume was scaled by the cube of the Burgers vector $b=a/2\langle 111\rangle$. Feuerbacher et al. [54] reported similar values for the activation volume in the range of 40 to 50 b^3. The activation volume values for TiZrNbHfTa at room temperature, as determined by Couzinié et al. [53], are therefore in good agreement with the results of the present work.

Senkov et al. [159] explored two high-melting refractory HEAs, NbMoTaW and VNbMoTaW, and found that the yield stress of these materials does not decrease strictly monotonically with temperature. Instead, there is a slight plateau between 800 and 1300 K, which indicates the presence of a YSA in these materials.

The mechanisms responsible for the YSA in TiVZrNbHf HEA could be different. In conventional intermetallic alloys, Kear-Wilsdorf locks and antiphase-boundaries in ordered phases, as well as dislocation locking mechanisms controlled by a diffusion mechanism, can be responsible for a YSA. The latter mechanism typically involves flow-stress instabilities, which are also observed in the temperature range of the YSA in the TiVZrNbHf HEA. Phase transitions can also lead to YSAs, and it is important to consider these mechanisms in the present material, as previous thermodynamic calculations using CALPHAD suggest the presence of a competing low-temperature phase in the Ti-Zr-Nb-V-Hf alloy system [62]. A detailed discussion of these mechanisms and their potential role in the YSA and plastic deformation behaviour of the TiVZrNbHf HEA can be found in the section 5.3.

The current research has carried out an extensive examination of the mechanical properties of poly-crystal TiVZrNbHf at temperatures ranging from room temperature to 1150 K. The CRSS and activation parameters for plastic deformation up to 10 % strain have been ascertained, delivering a comprehensive picture of these values up to high homologous temperatures that extend beyond previous reports, which have only carried out investigations at room temperature. It is worth noting that the yield stress anomaly has not been previously observed. However, it remains uncertain whether this YSA is a direct result of the solid solution microstructure of TiVZrNbHf based on the mechanical properties determined in this study.

Chapter 5

Microscopic Investigation of plastically deformed High-Entropy Alloys

To comprehensively elucidate the intrinsic mechanisms that govern the plastic deformation of crystalline materials, particularly at the microscopic level, this work conducted mechanical experiments in conjunction with analyses of the microstructure of characteristic deformed specimens of the two HEAs. Parameters at the microscale, including dislocation densities, Burgers vectors, and slip systems, were determined using transmission electron microscopy (TEM).

Most of the fundamental aspects of the plastic deformation theory were already introduced in 4.1. This chapter delves deeper into the subject of diffraction contrast and the examination of dislocations in crystalline materials through the application of transmission electron microscopy.

5.1 Experimental Methods

5.1.1 Sample Preparation

The samples selected for microscopic investigation were prepared in a uniform manner, following identical protocols for each characteristic deformation regime. After reaching approximately 3 % strain, the samples were promptly removed from the deformation machine and quenched on a metal plate to maintain the deformed microstructure. These samples were cut perpendicular to the deformation direction using a wire saw, with a thickness of about 0.7 mm. The samples were taken from the middle region of the deformation specimen. The cut samples were then polished on one side with 1 μm diamond paste and MasterPrep finish and subsequently ground to an approximate thickness of 100 μm using 1200 SiC grinding paper on the opposite side. Extreme care was taken to minimize the force introduced during grinding to avoid any sample deformation effects from the preparation process. The thickness of the samples was further reduced to approximately 20-30 μm on the ground side by dimpling. If necessary, the samples were attached to a copper support ring using a two-component adhesive.

The electron transparent regions in the dimpled samples were prepared using ion beam thinning on a Gatan PIPS II machine. The samples were thinned at 6 keV acceleration voltage, at an angle of ±6° from both sides, until an initial hole was formed. From this point, the thinning angle was reduced to ±4°, and the samples were thinned at 2 keV, 1 keV and 0.5 keV for 15 minutes at each voltage. Throughout the entire thinning procedure, the sample was cooled -50 °C to prevent any heating effects on the microstructure.

5.1.2 Transmission Electron Microscopy

All experiments conducted in this study were carried out using a FEI (Thermo Fisher Scientific) Tecnai F20 TEM at an acceleration voltage of 200 kV [160]. The sample was tilted using a Gatan double-tilt holder, and imaging modes such as bright field and electron diffraction were employed. Moderate magnifications around $7\text{x}10^3$ were mainly used. For a comprehensive understanding of transmission electron microscopy, the reader is directed towards standard literature sources such as [161].

5.1.3 Fundamental Techniques

The present work's microstructural analysis of the HEAs was conducted through the use of diffraction contrast imaging. The imaging of dislocation structures was performed in bright field mode, where the contrast was formed under two-beam conditions.

To fulfil the Bragg condition for only one reciprocal lattice vector $\vec{g}$, a diffraction image was generated containing only the non-diffracted electrons from the direct beam and one diffracted beam. By inserting an objective aperture that allowed only the direct beam to pass through, a bright field image was created in the image plane of the microscope. A dark field image would have been created if only the diffracted beam had been selected.

In a bright field image, areas that locally fulfil the Bragg condition corresponding to the diffracted beam appear dark, as the respective intensity is blanked by the objective aperture. This method allows for the detection of local strain fields, particularly the strain fields of dislocations. If the Bragg condition of a dislocation strain field is fulfilled for a given $\vec{g}$ but not for the surrounding perfect sample volume, the dislocation line will appear as a dark line in the surrounding brightly illuminated image, and vice versa in a dark field image [162].

Using this contrast formation, individual dislocations and dislocation structures can be examined.

Determination of the Dislocation Density

The dislocation density is defined as the amount of dislocation length per unit volume, which is expressed in units of square centimetres $\rho = L/V\,\text{in}\,[\text{cm}^{-2}]$. In this work, the dislocation density was calculated using the random intersection method, as described by [163] and modified by [164]. This method involves randomly placing a circle of radius r on a micrograph and counting the number of intersections, N, with the circle. The dislocation density is then calculated using

$$\rho = \frac{2 \cdot N}{\pi \cdot r \cdot t}, \tag{5.1}$$

where t represents the thickness of the foil at the measurement position. The thickness of the foil was determined using two separate methods.

1. Using the CBED method as described in [161], the thickness is determined by measuring the distance between the Kossel-Möllenstedt fringes $\Delta\theta_i$ and assigning appropriate fringe integers n yields the sample thickness.
2. By measuring the projected length of an individual dislocation under different tilt angles in relation to the line length in a defined state, the thickness can be calculated when the lattice plane on which the dislocation propagates (i.e. the slip plane) is known. The determination of the slip plane is described in the following paragraph.

In general, it may be noted that the exact determination of dislocation density within a specific area is hindered by the uneven distribution of dislocations. Nevertheless, since the order of magnitude of the dislocation density is the only aspect of interest, the associated errors can be deemed acceptable.

Analysis of the Burgers Vectors of Dislocations

The analysis of dislocations in the deformed HEA samples involved investigating a series of two-beam condition images. In an image, if the contrast resulting from the strain field of a dislocation is extinct, the reciprocal lattice vector $\vec{g}$ and the strain field vector $\vec{u}$ are perpendicular. The strain field of the dislocation does not contribute to the phase change of the electrons passing compared to the unstrained area.

If the strain field is characterized by the Burgers vector $\vec{b}$, the extinction relationship is given by

$$\vec{b}\vec{g} = 0. \tag{5.2}$$

By finding at least two extinction conditions with linearly independent $\vec{g}$, the Burgers vector can be calculated as the vector product of the respective $\vec{g}$.

Determination of the Line Direction and slip plane

The direction of the dislocation line may be ascertained through a series of tilting experiments. In any TEM micrograph, the line segment of a dislocation is projected onto a plane perpendicular to the incident electron beam. Consequently, the true line direction lies on the plane spanned by the incident beam direction and the projected line direction. By determining two such planes, one can locate the true line direction of the dislocation at the intersection of the two planes. Selecting incident beam directions of low index, such as {100} or {110}, and utilising the stereographic projection is advantageous for this procedure. To confirm the result, a third redundant image of the projected line direction and the incident beam may be analysed.

5.2 Results

5.2.1 Deformed CrMnFeCoNi Single Crystals

In the following paragraphs, the dislocation structures of CrMnFeCoNi single crystals deformed at characteristic temperatures are described. All samples were deformed and prepared as described in 5.1.1.

Dislocation Density

Figure 5.1 illustrates the microstructures of CrMnFeCoNi single crystals that have been deformed at room temperature, 400 K and 500 K. The samples were deformed along the $[53\bar{1}]$ and [210] directions at identical deformation temperatures. The thickness of the samples, as determined using the CBED method and the projected line length method (cf. chapter 5.1.3), is in good agreement with each other and amounts to 300±100 nm. The dislocation density was measured multiple times at different locations across the samples. Using equation 5.1, the dislocation density for all samples shown here is found to be $5 \cdot 10^{10}\,\mathrm{cm}^{-2}$ within the margin of error ($\pm 5 \cdot 10^{10}\,\mathrm{cm}^{-2}$) and the limitations of the technique described in paragraph 5.1.3.

Overall, the dislocation structure of the deformed CrMnFeCoNi single crystals consists of a mixture of long planar dislocations and dislocations running along stacked bands. This structure can be observed regardless of the deformation direction and temperature. It is worth noting that no stacking faults were detected in the CrMnFeCoNi samples.

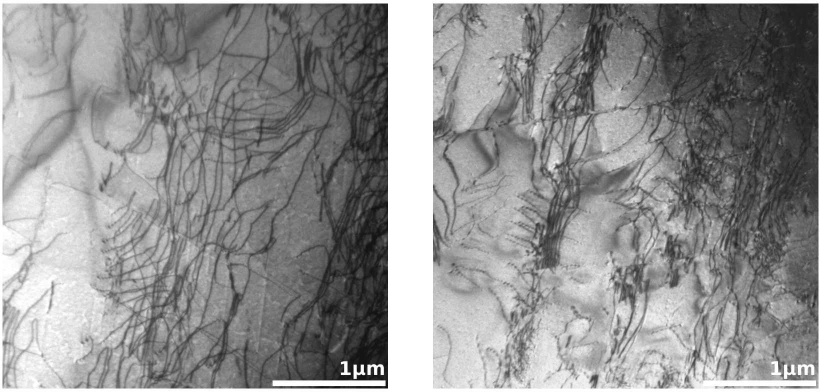

(a) *$[53\bar{1}]$ room temprature* **(b)** *[210] room temperature*

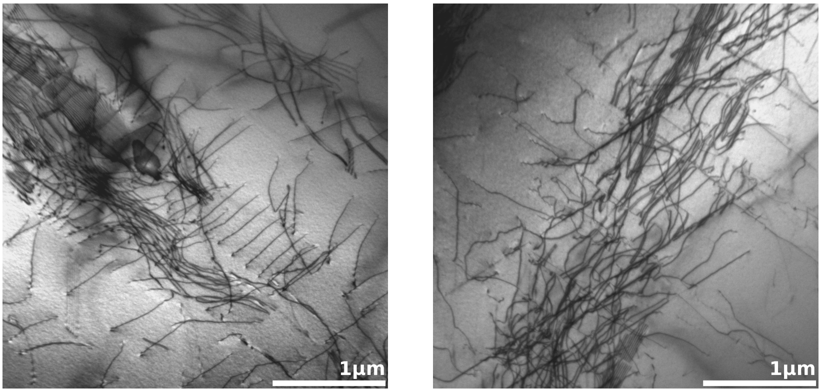

(c) *$[53\bar{1}]$ 400 K* **(d)** *[210] 400 K*

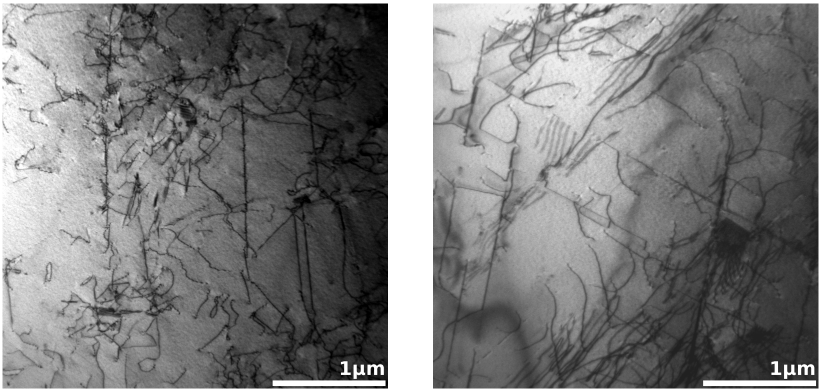

(e) *$[53\bar{1}]$ 500 K* **(f)** *[210] 500 K*

Fig. 5.1: *Comparison of the microstructures of CrMnFeCoNi single crystals deformed along $[53\bar{1}]$ and [210] direction at room temperature, 400 K and 500 K, respectively*

Table 5.1: *Burgers vectors of characteristic dislocations observed in deformed CrMnFeCoNi single crystals with respect to deformation direction and temperature*

	$[53\bar{1}]$	$[210]$
Room Temperature	$\frac{a}{2}[10\bar{1}]$, $\frac{a}{2}[01\bar{1}]$	$\frac{a}{2}[101]$
400 K	$\frac{a}{2}[10\bar{1}]$	$\frac{a}{2}[10\bar{1}]$, $\frac{a}{2}[1\bar{1}0]$
500 K	$\frac{a}{2}[101]$, $\frac{a}{2}[10\bar{1}]$, $\frac{a}{2}[0\bar{1}1]$, $\frac{a}{2}[01\bar{1}]$	$\frac{a}{2}[101]$

Burgers Vectors

The Burgers vectors of the dislocations observed in the TEM micrographs were analyzed using the extinction condition as described in paragraph 5.1.3. The process of determining the Burgers vector of a set of characteristic dislocations is illustrated in figure 5.2. Figure 5.2(a) shows a TEM micrograph near the [110] zone axis, where three distinct types of dislocations were identified in blue, green, and orange. Additional images in figure 5.2(b), 5.2(c) and 5.2(d) display micrographs of the same specimen and the identical specimen location, but tilted in a way that $\vec{g}=[1\bar{1}1]$, $\vec{g}=[020]$ and $\vec{g}=[1\bar{3}1]$, respectively. The contrast of dislocations of type 1 and 2, which is clearly visible in figure 5.2(a), is extinguished in figures 5.2(b), 5.2(c) and 5.2(d). Using equation 5.2, the Burgers vector of the dislocations of type 1 (blue) and 2 (green) was determined to be $\vec{b}=\frac{a}{2}[10\bar{1}]$, and the Burgers vector of the type 3 dislocations was determined to be $\vec{b}=\frac{a}{2}[01\bar{1}]$ from the dislocations being extinguished in figures 5.2(b) and (d). Undertaking an analysis of the Burgers vectors of characteristic dislocations present in CrMnFeCoNi single crystals subjected to deformation along the $[53\bar{1}]$ and [210] direction, it was possible to identify the Burgers vectors for all characteristic dislocations. The Burgers vectors for the characteristic dislocations observed in CrMnFeCoNi single crystals deformed at room temperature, 400 K, and 500 K are summarized in table 5.1.

Slip Planes and Systems

The line directions and the slip planes of the characteristic dislocations in the deformed CrMnFeCoNi single crystals were determined following the procedure described in 5.1.3. This procedure is illustrated in figure 5.3. To determine the projected line direction for each characteristic dislocation, a micrograph of the CrMnFeCoNi sample deformed at room temperature is taken near a low-index zone axis, which is indicated in the respective micrograph by an inset. By aligning the micrograph with the diffraction pattern, the projected line direction can be determined. The slip plane for each characteristic dislocation can then be determined from the intersection of these planes. For all three types, the procedure yields (111) as the slip plane. The Burgers vector and slip plane together determine the slip system

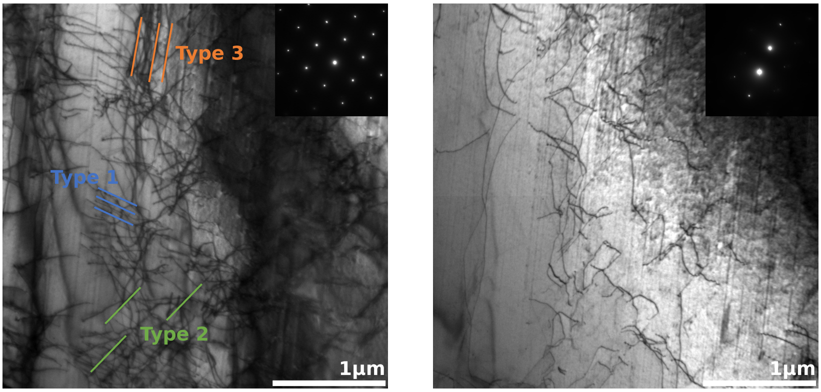

(a) *Micrograph close to the [110] zone axis* **(b)** *Micrograph with* $\vec{\mathbf{g}}$*=[1$\vec{1}$1]*

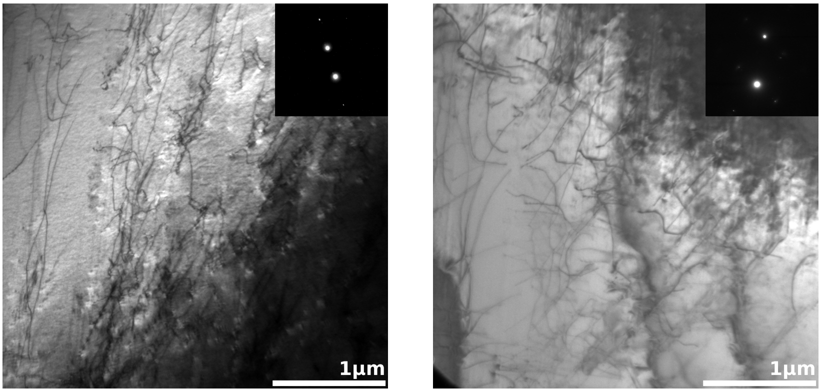

(c) *Micrograph with* $\vec{\mathbf{g}}$*=[020]* **(d)** *Micrograph with* $\vec{\mathbf{g}}$*=[1$\vec{1}$1]*

Fig. 5.2: *Extinction of a set of characteristic dislocations in a [53$\bar{1}$] single crystal deformed at room temperature allowing the determination of their Burgers vector*

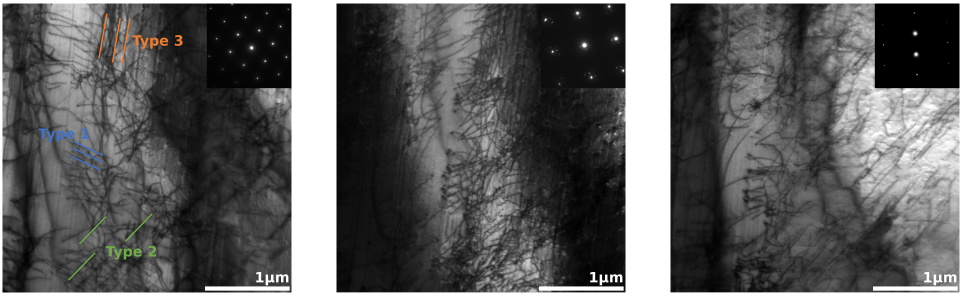

(a) *Micrograph close to the [110] zone axis*

(b) *Micrograph close to the [100] zone axis*

(c) *Micrograph close to the [301] zone axis*

Fig. 5.3: *Exemplary depiction of the determination of the slip planes of the characteristic dislocations in a $[53\bar{1}]$ single crystal deformed at room temperature*

Table 5.2: *Slip systems of characteristic dislocations observed in deformed CrMnFeCoNi single crystals with respect to deformation direction and temperature*

	$[53\bar{1}]$	$[210]$
Room Temperature	$[10\bar{1}](111)$, $[01\bar{1}](111)$	$[101](11\bar{1})$
400 K	$[10\bar{1}](111)$	$[10\bar{1}](111)$, $[1\bar{1}0](111)$
500 K	$[101](\bar{1}11)$, $[10\bar{1}](111)$, $[0\bar{1}1](111)$, $[01\bar{1}](\bar{1}11)$	$[101](\bar{1}11)$, $[101](11\bar{1})$

of the individual characteristic dislocations, which are of mixed edge and screw character. The slip systems of the characteristic dislocations observed in the deformed CrMnFeCoNi single crystals are listed in table 5.2. It is noted that more slip systems appear to be active in the $[53\bar{1}]$-deformed samples, although they are deformed in a crystal direction with lower symmetry than [210]. This discrepancy may be due to the lack of statistical investigations, which could result in an overemphasis on the observed slip systems compared to the active slip systems. The Schmid factor of a slip system was calculated using equation 4.8 and table 5.3 lists the slip system with the highest Schmid factor observed in any deformed CrMn-

Table 5.3: *Slip systems with the highest Schmid factor as observed in deformed CrMnFeCoNi single crystals with respect to deformation direction and temperature*

	$[53\bar{1}]$	m_S	$[210]$	m_S
Room Temperature	$[10\bar{1}](111)$	0.49	$[101](11\bar{1})$	0.49
400 K	$[10\bar{1}](111)$	0.49	$[10\bar{1}](111)$	0.49
500 K	$[10\bar{1}](111)$	0.49	$[101](11\bar{1})$	0.49

FeCoNi single crystal. Regardless of crystal orientation and temperature, all slip systems that were observed, including those with a Schmid factor lower than 0.49, are characteristic for face-centred cubic alloys, where slip occurs on $\{111\}$ planes in $\langle 1\bar{1}0\rangle$ direction. Table 5.3 emphasizes that in any given deformed CrMnFeCoNi single crystal, a slip system with a Schmid factor as high as 0.49 operates, regardless of the crystal's orientation and the deformation temperature.

5.2.2 Deformed polycrystalline TiVZrNbHf

The following paragraphs present a summary of the microscopic analysis outcomes for TiVZrNbHf polycrystals deformed at characteristic temperatures. All specimens underwent deformation and preparation as detailed in paragraph 5.1.1.

Dislocation Density

Figure 5.4 presents micrographs of fine-grained polycrystalline TiVZrNbHf that were deformed at characteristic temperatures ranging from room temperature to 850 K. Since the samples were polycrystalline, the image indices differ for each image in figure 5.4, despite all samples being cut perpendicular to the deformation direction. It is important to note that the micrographs depict the dislocation structure within a single grain, as the grain size was within the range of 300-500 μm.

The samples examined were chosen based on the characteristic temperature regimes that were identified during the mechanical characterization. The 600 K sample represents the microstructure of TiVZrNbHf at the onset of the YSA, the 750 K sample is near the maximum yield stress increase, and the 850 K sample is after the yield stress drops considerably (cf. figure 4.21). The dislocation structure of the sample deformed at room temperature in figure 5.4(a) is characterized by densely packed dislocation bands that are oriented in two distinct directions. The samples deformed at 600 K and 750 K have dislocation bands on which dislocations are densely packed, with a few long planar dislocations in between. The 850 K sample shows elongated features of darker contrast (as indicated by a few white arrows in figure 5.4) oriented in two directions, with short planar dislocations in between.

The thickness of the samples was determined according to chapter 5.1.3, with values around 100±50 nm. Using these thickness values, the dislocation density was determined according to the technique described in chapter 5.1.3 for several randomly selected spots across the sample surfaces. The dislocation densities were found to be in the range of 10^{10}-10^{11} cm^{-2} for the deformed TiVZrNbHf samples, regardless of the deformation temperature. The dislocation densities for TiVZrNbHf polycrystals deformed at characteristic temperatures are listed in table 5.4.

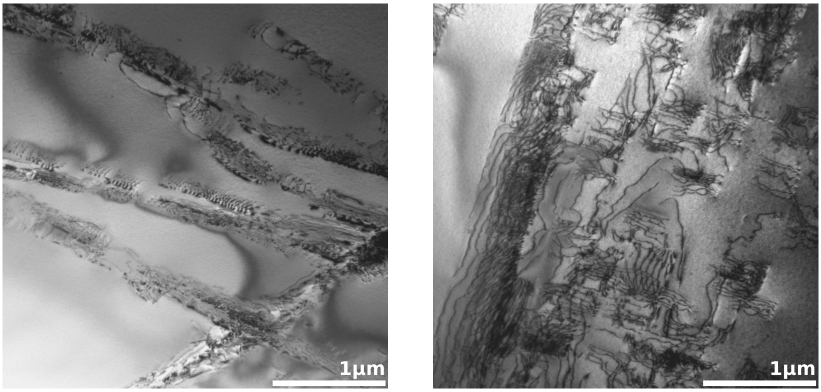

(a) *Room temperature* **(b)** *600 K*

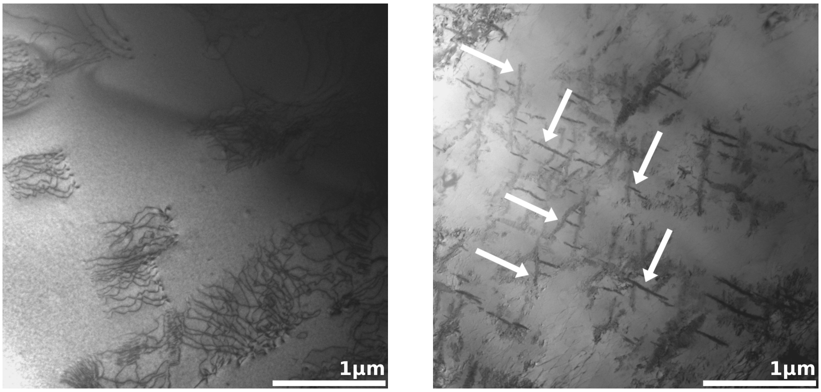

(c) *750 K* **(d)** *850 K*

Fig. 5.4: *Micrographs of polycrystalline ZrTiNbVHf samples deformed at characteristic temperatures. Arrows in* ***(d)*** *indicate the elongated feature.*

Burgers Vectors

The Burgers vectors of the characteristic dislocations observed in the deformed TiVZrNbHf polycrystals were determined using the extinction method in the same manner as for the CrMnFeCoNi single crystals. The procedure is described in chapter 5.1.3 and demonstrated for a deformed TiVZrNbHf sample in figure 5.5. Figure 5.5(a) shows a TEM micrograph of the sample near the $[11\bar{1}]$ zone axis, where four characteristic types of dislocations were identified and labelled in blue, green, orange, and red. Additional images in figure 5.5(b)-(f) show micrographs of the same specimen and the same location but tilted in different directions. The contrast of the dislocations of type 1 and 4 is clearly visible in figure 5.5(a) but is extinct in figures 5.5(c), (d) and (e). Using equation 5.2, the Burgers vector of the

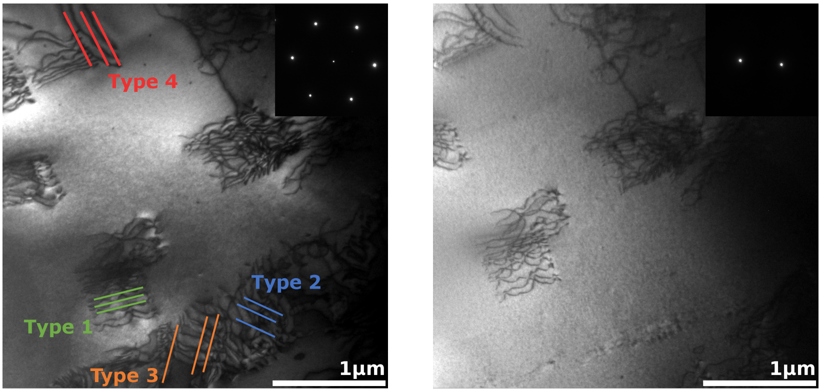

(a) *Micrograph close to the* $[11\bar{1}]$ *zone axis* **(b)** *Micrograph with* $\vec{\mathbf{g}}=[1\bar{1}0]$

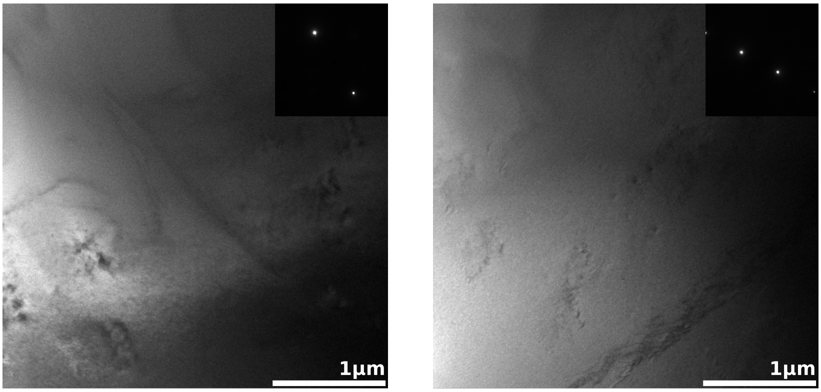

(c) *Micrograph with* $\vec{\mathbf{g}}=[1\bar{1}2]$ **(d)** *Micrograph with* $\vec{\mathbf{g}}=[01\bar{1}]$

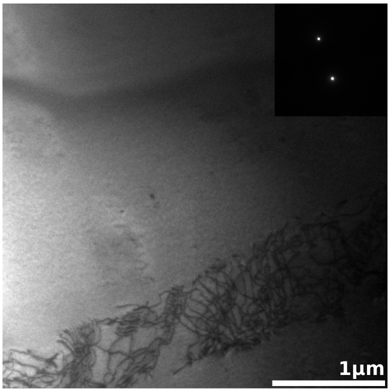

(e) *Micrograph with* $\vec{\mathbf{g}}=[\bar{1}0\bar{1}]$

Fig. 5.5: *Extinction of a set of characteristic dislocations in a TiVZrNbHf polycrystal deformed at 750 K allowing the determination of their Burgers vector*

Table 5.4: *Dislocation densities of ZrTiNbVHf polycrystals deformed at characteristic temperatures*

	ρ [cm^{-2}]
Room Temperature	$5 \cdot 10^{9}$
600 K	$9 \cdot 10^{10}$
750 K	$8 \cdot 10^{10}$
850 K	$7 \cdot 10^{10}$

Table 5.5: *Burgers vectors of characteristic dislocations observed in deformed TiVZrNbHf polycrystals with respect to the deformation temperature*

	Burgers Vectors
Room Temperature	$\frac{a}{2}[11\bar{1}]$
600 K	$\frac{a}{2}[11\bar{1}]$
750 K	$\frac{a}{2}[\bar{1}11]$, $\frac{a}{2}[111]$
850 K	$\frac{a}{2}[11\bar{1}]$

dislocations of type 1 (green) and 4 (red) was determined to be $\vec{b}=\frac{a}{2}[\bar{1}11]$ based on their extinction. Similarly, the Burgers vectors of the type 2 (blue) and 3 (orange) dislocations were determined to be $\vec{b}=\frac{a}{2}[111]$ from their extinction in figures 5.5(b), (d) and (e). Table 5.5 provides an overview of the Burgers vectors of the characteristic dislocations observed in the deformed TiVZrNbHf samples. As depicted in table 5.5, it is evident that only in the specimen deformed at 750 K dislocations with a Burgers vector $[11\bar{1}]$ were detected. However, all observed Burgers vectors in the TiVZrNbHf samples are characteristic of body-centred cubic alloys.

Slip Planes and Systems

The slip plane of the characteristic dislocations in the deformed TiVZrNbHf samples was determined using the procedure outlined in parargraph 5.1.3 and illustrated in figure 5.6. The micrographs of the TiVZrNbHf samples deformed at 750 K were taken near a low-index zone axis, as shown in the insets of each respective micrograph. The projected line direction for each characteristic dislocation was determined by aligning the micrograph and diffraction pattern, and the slip plane was determined by intersecting these planes. The slip plane for each characteristic dislocation was (101) for type 1 (green), $(11\bar{2})$ for type 2 (blue) and type 3 (orange) and $(12\bar{1})$ for type 4 (red). The Burgers vector and slip plane together define the slip system of the individual characteristic dislocations, which are of pure screw and mixed

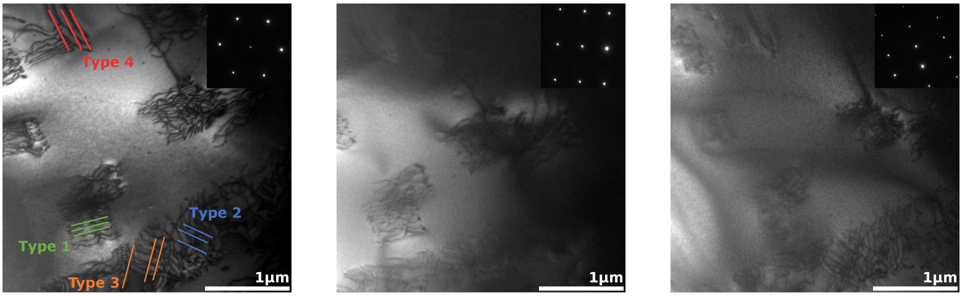

(a) *Micrograph close to the* $[11\bar{1}]$ *zone axis*

(b) *Micrograph close to the [110] zone axis*

(c) *Micrograph close to the* $[10\bar{1}]$ *zone axis*

Fig. 5.6: *Exemplary depiction of the determination of the slip planes of the characteristic dislocations in a TiVZrNbHf polycrystal deformed at 750 K*

Table 5.6: *Slip systems of characteristic dislocations observed in deformed TiVZrNbHf polycrystals with respect to the deformation temperature*

	Slip Systems
Room Temperature	$[11\bar{1}](110)$, $[11\bar{1}](1\bar{1}0)$, $[11\bar{1}](112)$
600 K	$[11\bar{1}](1\bar{1}0)$, $[11\bar{1}](112)$, $[11\bar{1}](011)$
750 K	$[111](11\bar{2})$, $[111](11\bar{2})$, $[\bar{1}11](101)$, $[\bar{1}11](12\bar{1})$
850 K	$[11\bar{1}](1\bar{1}0)$, $[11\bar{1}](1\overline{21})$, $[11\bar{1}](112)$

edge and screw character, respectively. A summary of the slip systems of the characteristic dislocations identified in the deformed TiVZrNbHf sample at the respective characteristic deformation temperatures is provided in table 5.6.

Chemical Analysis of TiVZrNbHf Samples deformed at 750 K and 850 K

The TiVZrNbHf sample deformed at 850 K displays elongated features that were depicted in figure 5.4(d). During the analysis of the sample, these elongated features could not be classified as dislocations. While the dislocations situated in between the elongated features were completely characterised using the extinction method, the features themselves remained uncharacterised. Moreover, the diffraction patterns of the features differed noticeably from those of the surrounding material, exhibiting no clear pattern, which suggests the presence of a secondary, possibly amorphous phase. Consequently, these samples were examined using an FEI Titan G2 80-200 ChemiSTEM equipped with an EDX [165]. The High-Angle Annular Dark-Field (HAADF) image in figure 5.7 displays the TiVZrNbHf sample deformed at 850 K, along with the EDX measurement results of the constituent elements. The HAADF

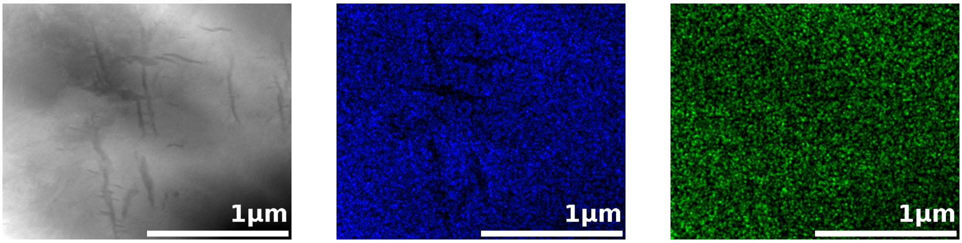

(a) *HAADF* **(b)** *Ti* **(c)** *Zr*

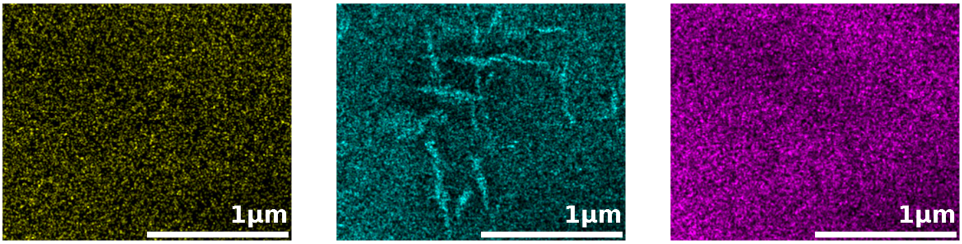

(d) *Nb* **(e)** *V* **(f)** *Hf*

Fig. 5.7: *HAADF image and EDX measurements of a TiVZrNbHf polycrystal deformed at 850 K*

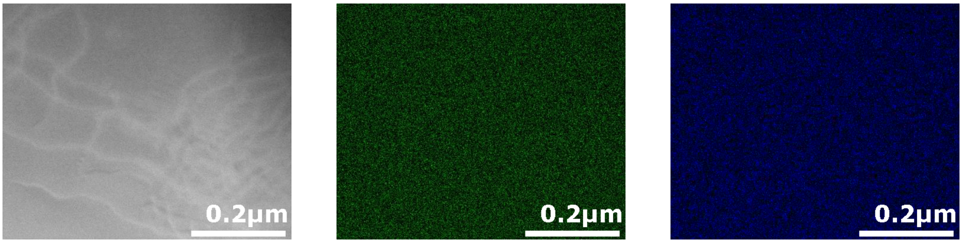

(a) *HAADF* **(b)** *Ti* **(c)** *Zr*

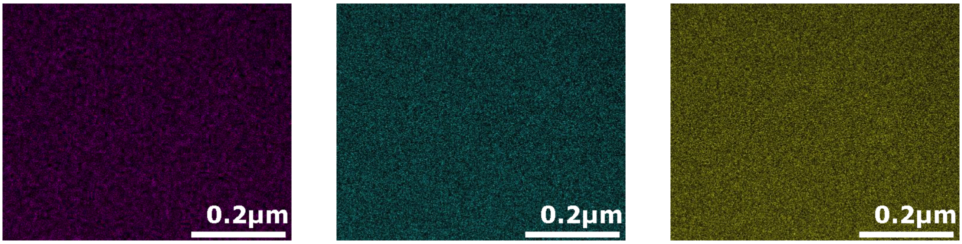

(d) *Nb* **(e)** *V* **(f)** *Hf*

Fig. 5.8: *HAADF image and EDX measurements of a TiVZrNbHf polycrystal deformed at 750 K*

image in figure 5.7(a) clearly shows elongated features that were previously visible in figure 5.4(d). The EDX measurements in figure 5.7(b)-(f) reveal that the elongated features are depleted of Ti and enriched in V, while the other constituent elements are distributed homogeneously throughout the sample's volume.

In order to determine if the V segregation present in the TiVZrNbHf specimen deformed at 850 K is also present in the TiVZrNbHf specimen deformed at 750 K, it was examined using the EDX in a FEI Titan G2 80-200 ChemiSTEM as well. Figure 5.8 shows the HAADF image of the TiVZrNbHf sample deformed at 750 K along with the EDX measurements of the constituent elements. Although the sample is not oriented such that a Bragg condition is fulfilled, the dislocation structure of the specimen is still visible in the HAADF image and resembles the structure depicted in figure 5.4(c). The EDX measurements in figure 5.8(b)-(f) reveal no obvious segregation or phase transformation after the deformation of TiVZrNbHf at 750 K.

5.3 Discussion

Incorporating the findings from the microstructural investigations into the broader discussion of the plastic deformation behaviour of the materials under study necessitates aligning the results of these investigations with the pertinent deformation parameters, such as stress, strain, and deformation temperature of the specimen. To ensure that the observed microstructure accurately reflects the state of deformation of the specimen as intended, it is crucial to preserve the structure as closely as possible during both the termination of the experiment and the preparation of the TEM sample. The impact of the TEM sample preparation on the microstructure of the specimen should be minimal. The decision regarding the termination of the deformation experiment has a much more significant influence on the microstructure of the specimen, particularly on the dislocation density.

The ideal termination condition would be to maintain the specimen under load while it is rapidly cooled. This would result in the dislocations being frozen in their final loading state. However, achieving these ideal conditions is not practical in experimental settings, and an alternative approach must be chosen that is as close to ideal as possible. As previously mentioned, all microstructure investigations of CrMnFeCoNi and TiVZrNbHf were carried out on samples that were deformed to approximately 3 %, unloaded, and quickly removed from the oven and deformation machine before being quenched on a metal plate. This method preserves the dislocation density and avoids recovery processes. However, this approach has a disadvantage in that the stress state changes during unloading, which can result in dislocations relaxing into a stress-free state. This is particularly true for samples deformed at higher temperatures, where mobile dislocations that can glide may change position during unloading, but the overall dislocation structure remains unaffected during

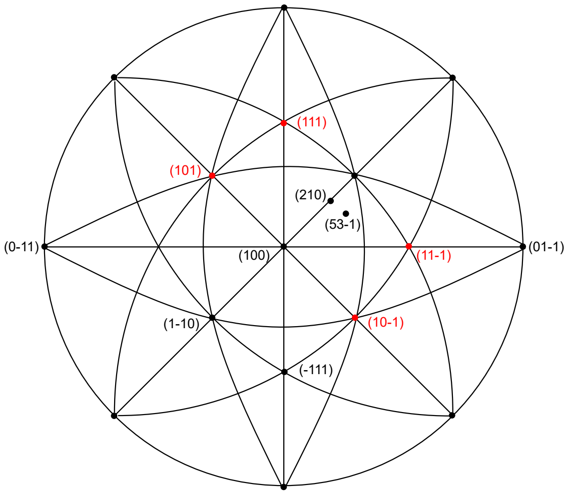

Fig. 5.9: *Stereographic projection of the available slip systems with a high Schmid factor for deformation of single crystals along [53$\bar{1}$] and [210]*

unloading and quenching. The main focus of this work is the analysis of dislocation density, Burgers vector, and slip systems, so the chosen termination conditions should be as close to ideal as possible.

5.3.1 Microstructure of deformed CrMnFeCoNi

The microstructure of the deformed CrMnFeCoNi single crystals was examined using TEM for two different crystal orientations: [53$\bar{1}$] and [210]. The choice of crystal orientation was made to either promote single-slip deformation (crystals deformed along [53$\bar{1}$]) or to trigger a reaction in the material when deformed along a crystal orientation with two favourable slip systems available (crystals deformed along [210]). The stereographic projection of the main axes of a *fcc* crystal in figure 5.9 shows the slip systems with a high Schmid factor for each crystal orientation in red. The dislocation density of CrMnFeCoNi has been investigated at various deformation temperatures and under the two crystal orientations. Regardless of the orientation and temperature, values of approximately $5 \cdot 10^{10}\,\mathrm{cm}^{-2}$ were observed. Considering the limitations of the technique, the deformation stage and flow stress at the termination point, similar dislocation densities are typically seen in other metals [166–169]. The dislocation structure of CrMnFeCoNi under deformation is illustrated in figure 5.1. The dislocations either form long flat planes or are concentrated in bands, regardless of the deformation orientation or temperature. Despite these similarities, samples deformed along the [201] double slip direction may exhibit increased dislocation interaction, leading to higher yield and flow stress (cf. figure 4.11), as well as a slightly greater work hardening rate compared to samples deformed along the $[53\bar{1}]$ direction. However, due to the limited sample size, this behaviour was not observed, and only the slip systems listed in table 5.2 were identified for the respective deformation directions. Further microstructure analysis may be necessary to elucidate this issue.

The analysis of the dislocations depicted in figure 5.1 was carried out to identify their Burgers vectors and the active slip systems during the deformation of CrMnFeCoNi single crystals at various temperatures. As shown in table 5.1, the dislocations observed in the deformed CrMnFeCoNi single crystals possess a Burgers vector of the $\frac{a}{2}\langle 110\rangle$-type, regardless of the crystal orientation. Additionally, the deformation is characterized by the slip of dislocations on $\{111\}\langle 110\rangle$-type slip systems, independent of orientation. The Burgers vectors of the dislocations and the slip systems they move on, in both $[53\bar{1}]$- and $[210]$-deformed samples, are characteristic of *fcc* materials [94]. The crystal orientations chosen were designed to promote single slip in the $[53\bar{1}]$ orientation or to provoke a reaction in the material by selecting the $[210]$ orientation, which has two favourable slip systems available. In the $[53\bar{1}]$-oriented samples, slip should occur on the $(111)[10\bar{1}]$ slip system, which has the highest Schmid factor of 0.49 for deformation along $[53\bar{1}]$. Deformation along the $[210]$ orientation provides two slip systems with a high Schmid factor of 0.49, $(111)[10\bar{1}]$ and $(11\bar{1})[101]$ (cf. figure 5.9). Based on the information presented in table 5.3, it is evident that the slip systems with the highest Schmid factors are activated in both the $[53\bar{1}]$- and $[210]$-deformed CrMnFeCoNi single crystals. However, it is not unexpected that other active slip systems have been identified in either orientation, as deformation occurs on multiple slip systems simultaneously, with only the slip system with the highest Schmid factor making a significant contribution to the overall deformation. It is not possible to draw a conclusion on whether only one slip system was activated in the $[53\bar{1}]$-oriented samples compared to possibly two slip systems in the $[210]$-oriented samples based on the available information. The differences observed in the macroscopic and microscopic investigations, as documented in figures 4.10, 4.12 and 5.1, respectively, may not only be a result of the different orientation, but could also be attributed to factors such as imprecise orientation, microstructure differences, or local variations in composition, which warrant further investigation. It is important to note that no dissociation of dislocations or other dislocation reactions were observed at any of the deformation temperatures or with regard to the crystal orientations that were investigated.

Previous research on the deformation structure of CrMnFeCoNi has focused on both single and polycrystals. These studies examined several aspects, including the mechanisms of plastic deformation from cryogenic to elevated temperatures and the determination of orientation- and temperature-dependent critical slip and twinning stresses for samples deformed in compression and tension. Kireeva et al. [40–42] conducted a series of studies to investigate the deformation behaviour of single-crystalline CrMnFeCoNi with respect to crystal orientation. Their findings indicate that different dislocation structures and twinning were observed depending on the orientation of the crystal, the deformation temperature, and strain. In crystals oriented along $[\bar{1}11]$, twinning was observed at room temperature at strains larger than 5 % [41], while in crystals oriented along $[\bar{1}23]$, winning was observed at room temperature only at strains larger than 27 %, with a critical twinning stress of $\tau_{CR}^{tw} = 140 \pm 10\text{MPa}$ [40]. No evidence of twinning was found in deformed [001]-oriented crystals [42]. In crystals oriented along $[\bar{1}11]$, dislocations formed tangles [40], similar to crystals oriented along [001], which also exhibited dislocation pile-ups at strains beyond 2.5% [42]. In crystals oriented along $[\bar{1}23]$, which is an orientation where single slip should take place, dislocations dissociated into partials forming stacking faults at strains above 10 % [40]. The findings of Kireeva et al. are consistent with the results of the present work, particularly with respect to the $[\bar{1}23]$-oriented crystals, which compare well to the single slip-oriented $[53\bar{1}]$ samples of the present work, where no twinning or dissociation of dislocations was observed at room temperature at strains as low as 3 %. Additionally, the dislocation structure observed by Kireeva et al. [40] in the $[\bar{1}23]$-oriented crystals resembles closely the dislocation structure of extensive planar dislocations forming pile-ups in one slip system, as observed in the $[53\bar{1}]$-deformed samples of the present work.

In a study conducted by Abuzaid et al. [44], the deformation behaviour of single-crystalline CrMnFeCoNi was investigated at various temperatures and crystal orientations. The authors observed that in orientations along [111] and [149] at room temperature, dislocation slip was the dominant deformation mechanism. In contrast, no twinning was observed in these orientations at room temperature, and the authors suggest that it is not expected in the [122]- and [123]-oriented crystals either. These findings are consistent with the results of the present work and the reports by Kireeva et al. [40–42], which also did not observe twinning at room temperature. Abuzaid et al. [44] further report that dislocation slip is the governing deformation mechanism in the [111]- and [149]-oriented crystals at room temperature, with single-slip occurring on either $(\bar{1}11)[11\bar{1}]$ or $(\bar{1}11)[0\bar{1}1]$ in the [111]-oriented crystal and on two systems, $(111)[\bar{1}01]$ and $(\bar{1}11)[\bar{1}0\bar{1}]$ in the [149] crystal. These findings are similar to those of Moon et al. [152], who refer to dislocation slip as the commonly accepted deformation mechanism at room temperature in *fcc* materials.

In a study conducted by Patriarca et al. [45], the slip nucleation in CrMnFeCoNi single crystals oriented along $[5\bar{9}1]$ at 77 K and room temperature was investigated. The authors reported that in the predominantly single slip orientation $[5\bar{9}1]$, dislocation slip was observed on two slip systems $[01\bar{1}](\bar{1}11)$ with a Schmid factor of 0.5 and $[0\bar{1}\bar{1}](1\bar{1}1)$ with a Schmid factor of 0.44 at room temperature. These findings are consistent with the results of the present work, where dislocations primarily moved on a high Schmid factor slip system in a single-slip oriented crystal, i.e. the $[53\overline{1}]$ orientation, while secondary slip systems were also detected.

In a comprehensive study, Kawamura et al. [43] investigated the deformation behaviour of single-crystalline CrMnFeCoNi over a broad temperature range from 10 to 1273 K in both tension and compression and assessed its dependence on crystal orientation. They focused on single crystals oriented along $[\overline{1}23]$, $[\overline{1}26]$ and $[\overline{3}\ 9\ 11]$, which are selected to promote single-slip. The authors discovered that deformation at room temperature is primarily governed by slip of dislocations for strains of up to 10%. Furthermore, they observed planar arrays of dislocations throughout most of the investigated temperatures, with dislocations beginning to climb out of their original slip plane at 1273 K. The presence of these extensive planar dislocation arrays is attributed to the low stacking fault energy of the CrMnFeCoNi HEA. Over a broad temperature range from 77 K to 1073 K, the dislocations, characterized by a Burgers vector typical for *fcc* materials with $b=1/2\langle 110\rangle$, were widely dissociated into partials separated by stacking faults. Kawamura et al. estimated the stacking fault energy to be $30 \pm 5\ \mathrm{mJ/m^2}$, which is consistent with the report by Okamoto et al. [39]. Kawamura et al. found that twinning only occurs in samples deformed at 77 K and is absent in all strains at room temperature, which is different from previous observations by Kireeva et al. [40] for the $[\overline{1}23]$ orientation, where twinning was observed at strains above 27%. The results of the present work are comparable to those of Kawamura et al. in the sense that both studies show that dislocations form planar arrays and exhibit *fcc*-typical Burgers vectors. However, unlike Kawamura et al., no dissociation of dislocations was observed in the present work, and the reason for this is currently unclear. Additionally, twinning was not observed at any temperature in the present study, which is similar to the findings of Kawamura et al., who attributed the lack of twinning at room and elevated temperatures to the high true stress of 890 MPa required for the onset of twinning, which they determined from tensile tests on $[\overline{1}23]$-oriented specimens.

The present study has comprehensively examined the microstructure of single-crystal CrMnFeCoNi at temperatures ranging from room temperature to 500 K. Dislocation density, slip systems and dislocation interactions for plastic deformation up to 10 % strain have been determined for a single-slip and dual-slip orientation, providing a detailed picture of these characteristics up to intermediate temperatures. This allows for direct comparison between these specific deformation cases and, in its entirety, extends beyond previous reports, which only focus on low-index or single-slip orientations. It is noteworthy that despite the difference in orientation in both $[53\overline{1}]$ and [210] oriented CrMnFeCoNi, similar slip systems are activated during deformation. Despite the detailed picture provided, the microscopic investigation of CrMnFeCoNi shows no unique characteristics that differentiate it from simpler *fcc* alloys, given its perfect solid solution microstructure.

5.3.2 Microstructure of deformed TiVZrNbHf

Table 5.4 contains the dislocation densities of TiVZrNbHf specimens deformed at characteristic temperatures. It is important to note that all dislocation densities fall within the range of 10^{10} cm^{-2}, regardless of the deformation temperature. This result should be considered in light of the limitations of the measurement technique and the margin of error. The dislocation density of deformed TiVZrNbHf compares favourably to other metals when considering the deformation stage and the flow stress at the point of termination, where similar values for the dislocation density are typically observed [166–169]. Additionally, it is interesting to note that the dislocation density of the specimen deformed in the temperature range of the YSA is similar to those samples deformed outside the YSA temperature range. This suggests that the YSA is not a result of increased nucleation of dislocations during deformation, which could have led to an increased yield stress.

Previously, the mechanical properties of TiVZrNbHf have been studied, as detailed in paragraph 4.5.2. However, the dislocation structure following deformation at different temperatures has not been extensively studied in any previous research, except in this work. To date, the governing deformation mechanisms in refractory HEAs have been investigated exclusively on the Senkov-alloy TiZrNbHfTa and only on samples deformed at room temperature. This was achieved through a combination of mechanical testing and nanoscale analysis [51, 53, 55–57, 159]. One notable exception is a study that investigated the flow-stress dependence on strain rate and temperature at elevated temperatures, along with SEM observations of the deformed TiZrNbHfTa samples [159].

In a study by Couzinié et al. [53] on as-cast TiZrNbHfTa, it was determined that the deformation of this material was governed by screw dislocations with $b = a/2\,\langle 111\rangle$ and the formation of dislocation bands occurring at an early stage of the deformation. These findings were later confirmed by Lilensten et al. [57] in their investigation of the room temperature deformation mechanisms of homogenized TiZrNbHfTa under tension. Their deformation experiments were conducted on cold-rolled and subsequently annealed sheets with a mean grain size of approximately 30 to 65 μm. The deformation in these samples was governed by the slip of screw dislocations, which were found to be rectilinear and have low mobility. This, combined with the determined activation volume, suggested high Peierls stresses in TiZrNbHfTa. Short-distance solid solution-related obstacles were proposed as the reason for the high yield stress of this particular alloy. Increasing dislocation density and the formation of a band structure were responsible for the strain hardening in TiZrNbHfTa, as reported by Lilensten et al. [57]. This conclusion was also reached in a study by Dirras et al. [55]. The findings of atomistic calculations conducted by Rao et al. [170] on dislocation configurations and mobility in a *bcc* multi-component concentrated solid solution indicate that short-range obstacles may be linked to local concentration fluctuations, which influence the dislocation core configuration and mobility. As reported by Rao et al. [170], the critical resolved shear stress for edge dislocations in refractory complex concentrated alloys may be comparable to that for screw dislocations, contrary to classical *bcc* metals. In addition, Senkov et al. [159] suggested that solute drag can serve as a strengthening mechanism in TiZrNbHfTa at elevated temperatures.

Similar to the findings of Couzinié et al. [53] and Lilensten et al. [57] for TiZrNbHfTa, the deformation of the TiVZrNbHf samples, as investigated in this work, is governed by slip of screw or mixed dislocations with a Burgers vector of the $b = a/2\langle 111\rangle$ type. The observed Burgers vectors are characteristic of the deformation of *bcc* materials [94]. Considering the slip planes of the governing dislocations, as listed in table 5.6, it is evident that dislocations in TiVZrNbHf predominantly move on slip systems of the $\langle 111\rangle\{110\}$- and $\langle 111\rangle\{112\}$-type (either pure screw or mixed character), which are characteristic of the deformation of bcc materials [94]. The dislocation structure of TiVZrNbHf samples deformed at characteristic temperatures is depicted in figure 5.4. At room temperature, dislocations are tightly packed into long, narrow bands running along two distinct directions. Although the bandwidth varies, affected by the different orientations of the image plane, a similar dislocation structure is observed in samples deformed at 600 K and 750 K. At both temperatures, dislocations are tightly packed into bands running along two distinct directions. From the selected areas, it may seem that the sample deformed at 600 K exhibits a far higher dislocation density than the samples deformed at room temperature and 750 K, respectively. However, measurements reveal that this is not the case (cf. table 5.4). The dislocation structure of the sample deformed at 850 K differs from the previous temperatures in that dislocations are not confined to bands but are instead randomly distributed throughout the sample. The dislocation structure observed in TiVZrNbHf at room temperature is similar to that of TiZrNbHfTa, as reported by Couzinié et al. [53]. Their study found the formation of dislocation bands at plastic strains above 0.85 %, which is consistent with the results obtained for TiVZrNbHf. Moreover, the densely packed dislocation bands observed in TiZrNbHfTa at plastic strains of 2.3 % are similar to those observed in TiVZrNbHf at 3 % plastic strain. The study by Lilensten et al. [57] of TiZrNbHfTa also showed similar results for the dislocation structure at strains of 2.89 %, with dislocations located in densely packed bands with two distinct directions, moving primarily on $\langle 111\rangle\{110\}$ and $\langle 111\rangle\{112\}$ systems.

A comparison of the dislocation structures of TiVZrNbHf that has been deformed at elevated temperatures cannot be made with TiZrNbHfTa, as temperature-dependent TEM investigations have not been reported for TiVZrNbHf. Although both TiVZrNbHf and TiZrNbHfTa exhibit similar deformation mechanisms at room temperature, TiZrNbHfTa does not display a YSA at elevated temperatures. It is important to examine the micro- and dislocation structures of the specimen deformed in the vicinity of the YSA maximum, at 750 K and 850 K, respectively, to understand the origin of the YSA. The formation of Kear Wilsdorf locks and anti-phase boundaries would require an ordered crystal structure, which is not present in TiVZrNbHf. Moreover, the identical dislocation structure and identified slip systems of the sample deformed at 750 K, close to the YSA maximum, compared to the sample deformed at 600 K, right at the onset of the YSA, suggest that the activation of secondary slip systems is not responsible for the YSA.

The YSA of TiZrNbVHf could have been caused by a diffusion-controlled mechanism other than Kear Wilsdorf locks, resulting in dislocation locking or phase transitions. Figures 5.7 and 5.8 show the EDX measurements of samples deformed at 750 K and 850 K, respectively. Figure 5.7 reveals that the 850K deformed sample exhibits elongated features, which are V-enriched and Ti-depleted segregations. These segregations are only visible in the sample deformed at 850 K and not in the sample deformed at 750 K, close to the maximum of the YSA. However, the EDX measurements do not allow for the exclusion of diffusion-based mechanisms being responsible for the YSA. As suggested by Rao et al. [170], short-distance obstacles and local dislocation fluctuations could be responsible for limited dislocation mobility, ultimately leading to the YSA. This effect could wear off, though, as soon as the local concentration fluctuations become large-scale precipitations, as observed in the TiVZrNbHf samples deformed at 850 K. The increased temperature could also enable the activation of secondary and ternary slip systems, suggesting that the diffusion coefficient for Vanadium in TiZrNbHf is extremely low. To better understand the mechanism behind the YSA, detailed investigations of the strain-rate dependency of the material combined with microstructure investigations at characteristic temperatures could be performed. These experiments would also provide insight into the origin of the serrations observed in TiZrNbVHf in the intermediate temperature regime (cf. figure 4.20).

The present study has comprehensively examined the microstructure of poly-crystal TiVZrNbHf at temperatures ranging from room temperature to 850 K. Dislocation density, slip systems and dislocation interactions for plastic deformation up to 10 % strain have been determined, providing a detailed picture of these characteristics up to high homologous temperatures that extends beyond previous reports, where microstructure investigations have only been carried out on samples deformed at room temperature. The YSA observed in the macroscopic investigation could not be tied definitively to specific changes in the dislocation characteristics at the microscopic level. The appearance of a secondary phase may indicate a diffusion-based mechanism as a reason for the YSA. Despite the detailed picture provided, further investigation of the microstructure is necessary to reveal the true nature of the YSA in TiVZrNbHf between 500 and 750 K.

Chapter 6

Conclusion and Outlook

6.1 Conclusion

In the present work, the deformation behaviour of two HEAs with distinct crystal structures, one *fcc* and one *bcc*, was examined. The *fcc*-HEA CrMnFeCoNi single crystals were studied in single-slip and dual-slip orientation. The mechanical properties of the *bcc*-HEA TiVZrNbHf were studied over an extended temperature range, revealing the presence of a yield strength anomaly at elevated temperatures that has not been reported in HEAs previously. The deformation properties and characteristics of both HEAs, determined through mechanical spectroscopy and TEM analysis, are discussed in chapter 4 and 5 in relation to the existing literature. This conclusion presents a few points for further investigation and highlights open questions.

1. The mechanical and microstructural characteristics of CrMnFeCoNi that have been observed in this study are consistent with existing data, thereby reinforcing the current hypothesis that CrMnFeCoNi is a conventional *fcc* alloy with exceptional strength. It is suggested that any potential short-range order does not have a significant impact on the material's mechanical properties, a proposition that is supported by the room temperature activation volume, which is essentially insensitive to strain as illustrated in figure 4.16 over the range of 120 to 200 MPa.

2. It is widely acknowledged that CrMnFeCoNi exhibits low stacking fault energy. However, only one study [43] has reported the dissociation of dislocations at low strains in single-slip oriented single crystals deformed at room and elevated temperatures. The existing literature is, therefore, inconclusive regarding the conditions that lead to the dissociation of dislocations in CrMnFeCoNi at room temperature and above. As no dissociation of dislocations was observed in the present work, further investiga-

tions focusing on the microstructure, specifically dendritic versus non-dendritic, may provide a clearer understanding of the phenomenon.

3. The need for further investigation into the dissimilarity in dislocation structure and activated slip systems between [$53\bar{1}$] and [210]-deformed CrMnFeCoNi is warranted in order to elucidate whether double slip is truly activated in samples oriented along [210] (cf. figure 5.9).

4. The present work has revealed substantial differences in the thermodynamic activation properties, particularly the activation volume, of CrMnFeCoNi at elevated temperatures compared to previous investigations [43]. The reason for this discrepancy remains unclear, but the differences are substantial, with a factor of almost 2 distinguishing the current findings from previous research.

5. The mechanical properties and dislocation structure of TiVZrNbHf, examined in this work, exhibit a striking resemblance to those of TiZrNbHfTa, likely attributable to the close similarity between the two alloys, arising from the interchange of Ta for V. The observed dislocations are characteristic of the deformation of *bcc* alloys, with regard to their Burgers vector and the active slip systems.

6. The YSA observed in TiVZrNbHf in the present work is unprecedented for HEAs. The low strain-rate sensitivity of the material and the flow stress instabilities observed in the corresponding temperature range suggest that the YSA may be a true feature of the plastic deformation rather than an artefact. The independent observation of the YSA by Gadelmeier et al. [158] further supports this conclusion (cf. figure 4.26). It is worth noting that the strain-rate sensitivity of the material should be negative in the YSA temperature range and that further investigations should focus on the relationship between the serrations observed in the YSA regime and the strain-rate sensitivity of the material. Such investigations will require specific experimental techniques.

7. Based on the microstructure investigations conducted on TiVZrNbHf in the present study, it is not possible to draw a definitive conclusion regarding the origin of the YSA. However, the observation of V-rich segregations above 800 K suggests that diffusion-controlled mechanisms may play a role in the formation of the YSA. Further investigations using high-resolution TEM, potentially conducted in situ, would be beneficial in deepening our understanding of the YSA's origin.

6.2 Outlook

Following the conclusions and open questions of this work, as summarized above, this section outlines future experimental approaches to improve the understanding of the structure-property relationships in the CrMnFeCoNi and TiVZrNbHf high-entropy alloys. These approaches will mostly be conducted at the Ernst Ruska-Centre (ER-C) and the future infrastructure ER-C 2.0 at Forschungszentrum Jülich. The proposed experiments will utilize the newly developed TOMO TEM, which integrates atom probe tomography (APT) [171], to further investigate the microstructure of these alloys.

6.2.1 CrMnFeCoNi

As previously mentioned, CrMnFeCoNi is presently considered a conventional *fcc* alloy with remarkable strength. However, the genuine impact of the five-component high-entropy alloy remains ambiguous, particularly with regard to potential short-range orders that may form in the alloy and the influence these (non-)orders have on dislocation movement. To enhance comprehension of the dislocation movement in CrMnFeCoNi regarding possible existing short-range orders and the random distribution of the constituent elements on the lattice, high-resolution in-situ TEM examinations may be useful. Additionally, the use of a TOMO microscope could shed light on the controversial question of whether short-range orders exist in CrMnFeCoNi by combining diffraction analysis and APT. In order to establish a more comprehensive understanding and model for the deformation mechanisms in fcc high-entropy alloys (HEAs), the in-situ high-resolution investigation of the dislocation movement could be repeated and compared to other five-component solid-solution HEAs or neighbouring alloys of CrMnFeCoNi where only one element is replaced while the alloy remains equiatomic and a solid solution. In this light, it is essential to reconsider and modify the production route for CrMnFeCoNi to ensure the production of high-quality single crystals that accommodate changes in the composition. Additionally, this optimization should include investigating the impact of a dendritic microstructure on dislocation movement at the atomic level. Kawamura et al. [43] posited that a dendritic microstructure leads to an overestimation of the CRSS, which remains to be confirmed at the microstructure level. Furthermore, it is necessary to explore the stacking fault energy and the dissociation of dislocations in CrMnFeCoNi. Statistically relevant measurements of the stacking fault energy are needed, as well as further investigation into the conditions under which dislocation dissociation occurs in this material. On the macroscopic level, it is important to conduct additional statistically relevant measurements of the activation parameters of CrMnFeCoNi at all temperatures to elucidate the differences between this study and other reports, particularly at elevated temperatures.

6.2.2 TiVZrNbHf

The primary observation of this work is the existence of a YSA in TiVZrNbHf at intermediate temperatures. The source of this YSA remains unconfirmed, and further research should concentrate on elucidating the mechanisms responsible for it. To accomplish this, a more stringent temperature grid should be used during mechanical testing to pinpoint the YSA's maximum and onset. This tighter grid would also enable a more precise examination of the material's strain-rate sensitivity, which would offer a clearer understanding of the YSA's underlying mechanisms. Developing a growth method to produce single crystals of TiVZrNbHf and analysing the mechanical properties of specific crystallographic orientations would provide detailed information about the activation parameters. Additionally, microtesting existing TiVZrNbHf poly-crystals could offer similar insights, as these samples contain large enough grains to be analysed using TEM for in-situ mechanical analysis at the microscale. These tests could follow similar paths as described for CrMnFeCoNi by focusing on short-range order detection, dislocation-solute interaction at different temperatures, and microstructure development across characteristic temperature regimes. Specifically, in-situ deformation within the TOMO microscope near the maximum of the YSA could provide valuable insights to deepen the understanding of the YSA. It would also showcase whether diffusion processes play a detrimental role in the YSA, as they might occur only on an atomic level. Utilising the TOMO would provide a deeper understanding of the cigar-shaped feature observed in the material after deformation at 850 K, where the TOMO could provide a combination of diffraction analysis and APT. By understanding the mechanism behind the YSA in TiVZrNbHf, future experiments could provide insights into whether the YSA could be harnessed for practical applications of *bcc* alloys in intermediate temperature regimes.

Acknowledgements

Without the help and support of many people, this work would never have been written and I would like to use these lines to express my sincere gratitude to them.

I am grateful for the support and guidance of Prof. Rafal Dunin-Borkowski and Prof. Joachim Mayer, who allowed me to prepare this work at the Ernst Ruska-Centre. I am incredibly grateful for the mentorship of my day-to-day supervisor, Mick Feuerbacher. He has provided invaluable support, encouragement, and guidance throughout the research and writing process.

I would like to express my sincere gratitude to the following individuals who have played a significant role in this endeavour. Carsten for your motivation in and out of the laboratory, all the coffee, and numerous rounds of boules. Marc Heggen and András Kovács for their encouragement, kindness, and listening. Theresa, Patrick, Paul, Jan, and Florian my fellow doctoral researchers for their camaraderie, willingness to share knowledge, and the leisure activities we shared. Marta, Lidia, and Max for all the laughter we shared in the office and the generous support when help was needed and time was short. Luyan for helping with the final TEM investigations. Werner Pieper, Wilma Sybertz, Eva Wirtz, and Martina Luysberg for their technical support, and Marie Göcking for the administrative and emotional support. Our project partners at the University of Bayreuth Prof. Uwe Glatzel, Sebastian Haas, and especially Christian Gadelmeier for their passionate work and dedication to our collaboration.

Finally to the people in my personal life: I would like to express my deepest gratitude to my parents, for their support, advice and love. To Bettina, I am grateful for her unwavering love, encouragement, sacrifices, belief in my abilities, and the wonderful moments we share with Jona.

Bibliography

[1] Joseph R. Davis, editor. *Metals Handbook Desk Edition*. ASM International, December 1998.

[2] Jerzy Piaskowski and Cyril Stanley Smith. Four outstanding researches in metallurgical history. 1966.

[3] Cyril Stanley Smith. *A history of metallography*. MIT Press, 1988.

[4] H. Okamoto, M.E. Schlesinger, and E.M. Mueller, editors. *Alloy Phase Diagrams*. ASM International, apr 2016.

[5] R. Abbaschian. *Physical metallurgy principles*. Cengage Learning, 2009.

[6] V. Raghavan. Al-cu-zn (aluminum-copper-zinc). *Journal of Phase Equilibria and Diffusion*, 28(2):183–188, apr 2007.

[7] J.-W. Yeh, S.-K. Chen, S.-J. Lin, J.-Y. Gan, T.-S. Chin, T.-T. Shun, C.-H. Tsau, and S.-Y. Chang. Nanostructured high-entropy alloys with multiple principal elements: Novel alloy design concepts and outcomes. *Advanced Engineering Materials*, 6(5):299–303, may 2004.

[8] B. Cantor, I.T.H. Chang, P. Knight, and A.J.B. Vincent. Microstructural development in equiatomic multicomponent alloys. *Materials Science and Engineering: A*, 375-377:213–218, jul 2004.

[9] Easo P. George, Dierk Raabe, and Robert O. Ritchie. High-entropy alloys. *Nature Reviews Materials*, 4(8):515–534, jun 2019.

[10] B. S. Murty, Jien-Wei Yeh, S. Ranganathan, and P. P. Bhattacharjee. *High-Entropy Alloys*. Elsevier, 2019.

[11] Y.F. Ye, Q. Wang, J. Lu, C.T. Liu, and Y. Yang. High-entropy alloy: challenges and prospects. *Materials Today*, 19(6):349–362, jul 2016.

[12] R.E. Smallman and A.H.W. Ngan. Chapter 2 - phase diagrams and alloy theory. In R.E. Smallman and A.H.W. Ngan, editors, *Modern Physical Metallurgy (Eighth Edition)*, pages 43 – 91. Butterworth-Heinemann, Oxford, eighth edition edition, 2014.

[13] B. Predel. Al-cu (aluminum - copper): Datasheet from landolt-börnstein - group iv physical chemistry · volume 12a: “ac-ag ... au-zr” in springermaterials (https://doi.org/10.1007/10793176_86). Copyright 2006 Springer-Verlag Berlin Heidelberg.

[14] B. Predel. Cu-zn (copper-zinc): Datasheet from landolt-börnstein - group iv physical chemistry · volume 5d: “cr-cs – cu-zr” in springermaterials (https://doi.org/10.1007/10086090_1134). Copyright 1994 Springer-Verlag Berlin Heidelberg.

[15] Ernö Keszei. *Chemical Thermodynamics*. Springer Berlin Heidelberg, 2012.

[16] A.R. Miedema, P.F. de Châtel, and F.R. de Boer. Cohesion in alloys — fundamentals of a semi-empirical model. *Physica B+C*, 100(1):1–28, apr 1980.

[17] Akihisa Inoue, Akira Takeuchi, and Baolong Shen. Formation and functional properties of fe-based bulk glassy alloys. *MATERIALS TRANSACTIONS*, 42(6):970–978, 2001.

[18] Y. Zhang, Y. J. Zhou, J. P. Lin, G. L. Chen, and P. K. Liaw. Solid-solution phase formation rules for multi-component alloys. *Advanced Engineering Materials*, 10(6):534–538, jun 2008.

[19] Shoushi Fang, Xueshan Xiao, Lei Xia, Weihuo Li, and Yuanda Dong. Relationship between the widths of supercooled liquid regions and bond parameters of mg-based bulk metallic glasses. *Journal of Non-Crystalline Solids*, 321(1-2):120–125, jun 2003.

[20] Y. Zhang, Z.P. Lu, S.G. Ma, P.K. Liaw, Z. Tang, Y.Q. Cheng, and M.C. Gao. Guidelines in predicting phase formation of high-entropy alloys. *MRS Communications*, 4(2):57–62, 2014.

[21] F. Otto, Y. Yang, H. Bei, and E.P. George. Relative effects of enthalpy and entropy on the phase stability of equiatomic high-entropy alloys. *Acta Materialia*, 61(7):2628–2638, apr 2013.

[22] Michael C. Gao, Jien-Wei Yeh, Peter K. Liaw, and Yong Zhang, editors. *High-Entropy Alloys*. Springer International Publishing, 2016.

[23] Ming-Hung Tsai and Jien-Wei Yeh. High-entropy alloys: A critical review. *Materials Research Letters*, 2(3):107–123, apr 2014.

[24] D.B. Miracle and O.N. Senkov. A critical review of high entropy alloys and related concepts. *Acta Materialia*, 122:448–511, jan 2017.

[25] Oleg N. Senkov, Daniel B. Miracle, Kevin J. Chaput, and Jean-Philippe Couzinie. Development and exploration of refractory high entropy alloys—a review. *Journal of Materials Research*, 33(19):3092–3128, jun 2018.

[26] F. Otto, A. Dlouhý, K.G. Pradeep, M. Kuběnová, D. Raabe, G. Eggeler, and E.P. George. Decomposition of the single-phase high-entropy alloy CrMnFeCoNi after prolonged anneals at intermediate temperatures. *Acta Materialia*, 112:40–52, jun 2016.

[27] B. Schuh, F. Mendez-Martin, B. Völker, E.P. George, H. Clemens, R. Pippan, and A. Hohenwarter. Mechanical properties, microstructure and thermal stability of a nanocrystalline CoCrFeMnNi high-entropy alloy after severe plastic deformation. *Acta Materialia*, 96:258–268, sep 2015.

[28] E.J. Pickering, R. Muñoz-Moreno, H.J. Stone, and N.G. Jones. Precipitation in the equiatomic high-entropy alloy CrMnFeCoNi. *Scripta Materialia*, 113:106–109, mar 2016.

[29] G. Laplanche, S. Berglund, C. Reinhart, A. Kostka, F. Fox, and E.P. George. Phase stability and kinetics of σ-phase precipitation in CrMnFeCoNi high-entropy alloys. *Acta Materialia*, 161:338–351, dec 2018.

[30] P.P. Bhattacharjee, G.D. Sathiaraj, M. Zaid, J.R. Gatti, Chi Lee, Che-Wei Tsai, and Jien-Wei Yeh. Microstructure and texture evolution during annealing of equiatomic CoCrFeMnNi high-entropy alloy. *Journal of Alloys and Compounds*, 587:544–552, feb 2014.

[31] A. Gali and E.P. George. Tensile properties of high- and medium-entropy alloys. *Intermetallics*, 39:74–78, aug 2013.

[32] G.A. Salishchev, M.A. Tikhonovsky, D.G. Shaysultanov, N.D. Stepanov, A.V. Kuznetsov, I.V. Kolodiy, A.S. Tortika, and O.N. Senkov. Effect of mn and v on structure and mechanical properties of high-entropy alloys based on CoCrFeNi system. *Journal of Alloys and Compounds*, 591:11–21, apr 2014.

[33] G. Laplanche, O. Horst, F. Otto, G. Eggeler, and E.P. George. Microstructural evolution of a CoCrFeMnNi high-entropy alloy after swaging and annealing. *Journal of Alloys and Compounds*, 647:548–557, oct 2015.

[34] F. Otto, N.L. Hanold, and E.P. George. Microstructural evolution after thermomechanical processing in an equiatomic, single-phase CoCrFeMnNi high-entropy alloy with special focus on twin boundaries. *Intermetallics*, 54:39–48, nov 2014.

[35] F. Otto, A. Dlouhý, Ch. Somsen, H. Bei, G. Eggeler, and E.P. George. The influences of temperature and microstructure on the tensile properties of a CoCrFeMnNi high-entropy alloy. *Acta Materialia*, 61(15):5743–5755, sep 2013.

[36] Mathilde Laurent-Brocq, Alfiya Akhatova, Loïc Perrière, Siham Chebini, Xavier Sauvage, Eric Leroy, and Yannick Champion. Insights into the phase diagram of the CrMnFeCoNi high entropy alloy. *Acta Materialia*, 88:355–365, apr 2015.

[37] Jun Ding, Qin Yu, Mark Asta, and Robert O. Ritchie. Tunable stacking fault energies by tailoring local chemical order in CrCoNi medium-entropy alloys. *Proceedings of the National Academy of Sciences*, 115(36):8919–8924, aug 2018.

[38] G. Laplanche, A. Kostka, O.M. Horst, G. Eggeler, and E.P. George. Microstructure evolution and critical stress for twinning in the CrMnFeCoNi high-entropy alloy. *Acta Materialia*, 118:152–163, oct 2016.

[39] Norihiko L. Okamoto, Shu Fujimoto, Yuki Kambara, Marino Kawamura, Zhenghao M. T. Chen, Hirotaka Matsunoshita, Katsushi Tanaka, Haruyuki Inui, and Easo P. George. Size effect, critical resolved shear stress, stacking fault energy, and solid solution strengthening in the CrMnFeCoNi high-entropy alloy. *Scientific Reports*, 6(1), oct 2016.

[40] I.V. Kireeva, Yu.I. Chumlyakov, Z.V. Pobedennaya, I.V. Kuksgausen, and I. Karaman. Orientation dependence of twinning in single crystalline CoCrFeMnNi high-entropy alloy. *Materials Science and Engineering: A*, 705:176–181, sep 2017.

[41] Irina Kireeva, Yurii Chumlyakov, Zinaida Pobedennaya, Dmitrii Kuksgauzen, Ibrahim Karaman, and Huseyin Sehitoglu. Mechanisms of plastic deformation in [1¯11]-oriented single crystals of FeNiMnCrCo high entropy alloy. Author(s), 2016.

[42] I.V. Kireeva, Yu.I. Chumlyakov, Z.V. Pobedennaya, A.V. Vyrodova, and I. Karaman. Twinning in [001]-oriented single crystals of CoCrFeMnNi high-entropy alloy at tensile deformation. *Materials Science and Engineering: A*, 713:253–259, jan 2018.

[43] Marino Kawamura, Makoto Asakura, Norihiko L. Okamoto, Kyosuke Kishida, Haruyuki Inui, and Easo P. George. Plastic deformation of single crystals of the equiatomic cr-mn-fe-co-ni high-entropy alloy in tension and compression from 10 k to 1273 k. *Acta Materialia*, 203:116454, jan 2021.

[44] Wael Abuzaid and Huseyin Sehitoglu. Critical resolved shear stress for slip and twin nucleation in single crystalline FeNiCoCrMn high entropy alloy. *Materials Characterization*, 129:288–299, jul 2017.

[45] L. Patriarca, A. Ojha, H. Sehitoglu, and Y.I. Chumlyakov. Slip nucleation in single crystal FeNiCoCrMn high entropy alloy. *Scripta Materialia*, 112:54–57, feb 2016.

[46] Y. Wu, M. Bönisch, S. Alkan, W. Abuzaid, and H. Sehitoglu. Experimental determination of latent hardening coefficients in FeMnNiCoCr. *International Journal of Plasticity*, 105:239–260, jun 2018.

[47] Dengshan Zhou, Zhenghao Chen, Kazuki Ehara, Kodai Nitsu, Katsushi Tanaka, and Haruyuki Inui. Effects of annealing on hardness, yield strength and dislocation structure in single crystals of the equiatomic cr-mn-fe-co-ni high entropy alloy. *Scripta Materialia*, 191:173–178, jan 2021.

[48] I.V. Kireeva, Yu.I. Chumlyakov, A.V. Vyrodova, Z.V. Pobedennaya, and I. Karaman. Effect of twinning on the orientation dependence of mechanical behaviour and fracture in single crystals of the equiatomic CoCrFeMnNi high-entropy alloy at 77k. *Materials Science and Engineering: A*, 784:139315, may 2020.

[49] O.N. Senkov, G.B. Wilks, D.B. Miracle, C.P. Chuang, and P.K. Liaw. Refractory high-entropy alloys. *Intermetallics*, 18(9):1758–1765, sep 2010.

[50] O.N. Senkov, G.B. Wilks, J.M. Scott, and D.B. Miracle. Mechanical properties of nb25mo25ta25w25 and v20nb20mo20ta20w20 refractory high entropy alloys. *Intermetallics*, 19(5):698–706, may 2011.

[51] O.N. Senkov, J.M. Scott, S.V. Senkova, D.B. Miracle, and C.F. Woodward. Microstructure and room temperature properties of a high-entropy TaNbHfZrTi alloy. *Journal of Alloys and Compounds*, 509(20):6043–6048, may 2011.

[52] Chun-Ming Lin, Chien-Chang Juan, Chia-Hsiu Chang, Che-Wei Tsai, and Jien-Wei Yeh. Effect of al addition on mechanical properties and microstructure of refractory AlxHfNbTaTiZr alloys. *Journal of Alloys and Compounds*, 624:100–107, mar 2015.

[53] J.-Ph. Couzinié, L. Lilensten, Y. Champion, G. Dirras, L. Perrière, and I. Guillot. On the room temperature deformation mechanisms of a TiZrHfNbTa refractory high-entropy alloy. *Materials Science and Engineering: A*, 645:255–263, oct 2015.

[54] M. Feuerbacher, M. Heidelmann, and C. Thomas. Plastic deformation properties of zr–nb–ti–ta–hf high-entropy alloys. *Philosophical Magazine*, 95(11):1221–1232, mar 2015.

[55] G. Dirras, L. Lilensten, P. Djemia, M. Laurent-Brocq, D. Tingaud, J.-P. Couzinié, L. Perrière, T. Chauveau, and I. Guillot. Elastic and plastic properties of as-cast equimolar TiHfZrTaNb high-entropy alloy. *Materials Science and Engineering: A*, 654:30–38, jan 2016.

[56] G. Dirras, J. Gubicza, A. Heczel, L. Lilensten, J.-P. Couzinié, L. Perrière, I. Guillot, and A. Hocini. Microstructural investigation of plastically deformed ti20zr20hf20nb20ta20 high entropy alloy by x-ray diffraction and transmission electron microscopy. *Materials Characterization*, 108:1–7, oct 2015.

[57] L. Lilensten, J.-P. Couzinié, L. Perrière, A. Hocini, C. Keller, G. Dirras, and I. Guillot. Study of a bcc multi-principal element alloy: Tensile and simple shear properties and underlying deformation mechanisms. *Acta Materialia*, 142:131–141, jan 2018.

[58] É. Fazakas, V. Zadorozhnyy, L.K. Varga, A. Inoue, D.V. Louzguine-Luzgin, Fuyang Tian, and L. Vitos. Experimental and theoretical study of ti20zr20hf20nb20x20 (x = v or cr) refractory high-entropy alloys. *International Journal of Refractory Metals and Hard Materials*, 47:131–138, nov 2014.

[59] Xiaoqing Li, Fuyang Tian, Stephan Schönecker, Jijun Zhao, and Levente Vitos. Ab initio-predicted micro-mechanical performance of refractory high-entropy alloys. *Scientific Reports*, 5(1), jul 2015.

[60] M. C. Gao, B. Zhang, S. Yang, and S. M. Guo. Senary refractory high-entropy alloy HfNbTaTiVZr. *Metallurgical and Materials Transactions A*, 47(7):3333–3345, sep 2015.

[61] M. Feuerbacher, T. Lienig, and C. Thomas. A single-phase bcc high-entropy alloy in the refractory zr-nb-ti-v-hf system. *Scripta Materialia*, 152:40–43, jul 2018.

[62] Victor Pacheco, Greta Lindwall, Dennis Karlsson, Johan Cedervall, Stefan Fritze, Gustav Ek, Pedro Berastegui, Martin Sahlberg, and Ulf Jansson. Thermal stability of the HfNbTiVZr high-entropy alloy. *Inorganic Chemistry*, 58(1):811–820, dec 2018.

[63] David A. Porter, Kenneth E. Easterling, and Mohamed Y. Sherif. *Phase Transformations in Metals and Alloys*. CRC Press, sep 2021.

[64] C.D. BRANDLE. Crystal pulling. In *Crystal Growth*, pages 275–300. Elsevier, 1980.

[65] J.S. SHAH. Chapter 8 - zone refining and its applications. In BRIAN R. PAMPLIN, editor, *Crystal Growth (Second Edition)*, volume 16 of *International Series in the Science of the Solid State*, pages 301 – 355. Pergamon, second edition edition, 1980.

[66] Setaram. Setaram setsys evolution tga sta ega for evolved gas analysis.

[67] P. W. Bridgman. On the effect of general mechanical stress on the temperature of transition of two phases, with a discussion of plasticity. *Physical Review*, 7(2):215–223, feb 1916.

[68] Michael Gao and David Alman. Searching for next single-phase high-entropy alloy compositions. *Entropy*, 15(12):4504–4519, oct 2013.

[69] Song-Mao Liang and Rainer Schmid-Fetzer. Evaluation of calphad approach and empirical rules on the phase stability of multi-principal element alloys. *Journal of Phase Equilibria and Diffusion*, 38(4):369–381, jul 2017.

[70] Nokeun Park, Byeong-Joo Lee, and Nobuhiro Tsuji. The phase stability of equiatomic CoCrFeMnNi high-entropy alloy: Comparison between experiment and calculation results. *Journal of Alloys and Compounds*, 719:189–193, sep 2017.

[71] L. Vegard. Die konstitution der mischkristalle und die raumfüllung der atome. *Zeitschrift für Physik*, 5(1):17–26, jan 1921.

[72] Jerome Mertz. *Introduction to Optical Microscopy*. Cambridge University Press, 2 edition, 2019.

[73] JD Hunt. Solidification and casting of metals. *The Metal Society, London*, 3, 1979.

[74] M.H. Burden and J.D. Hunt. Cellular and dendritic growth. II. *Journal of Crystal Growth*, 22(2):109–116, apr 1974.

[75] R. Trivedi. Interdendritic spacing: Part II. a comparison of theory and experiment. *Metallurgical and Materials Transactions A*, 15(6):977–982, jun 1984.

[76] W. Kurz and D.J. Fisher. Dendrite growth at the limit of stability: tip radius and spacing. *Acta Metallurgica*, 29(1):11–20, jan 1981.

[77] C. L. Brundidge, J. D. Miller, and T. M. Pollock. Development of dendritic structure in the liquid-metal-cooled, directional-solidification process. *Metallurgical and Materials Transactions A*, 42(9):2723–2732, apr 2011.

[78] Maodong Kang, Junwei Yu, Jun Wang, and Baode Sun. Influence of drawing velocity on the inner quality of single-crystal superalloy. *Journal of Materials Engineering and Performance*, 29(5):2816–2826, apr 2020.

[79] Fazlollah Sadeghi, Ahmad Kermanpur, Davoud Heydari, and Majid Bahmani. Effect of withdrawal rate transition on microstructural features of a single crystal ni-based superalloy. *Crystal Research and Technology*, 52(6):1700012, may 2017.

[80] G. Sifeng, L. Lin, X. Yiku, Y Chubin, Z. Jun, and F. Hengzhi. Influences of processing parameters on microstructure during investment casting of nickel-base single crystal superalloy dd3. *China Foundry*, 9(2), 2012.

[81] Duane C. Wallace, editor. *Thermodynamics of crystals*. Wiley, New York, 1972. englisch.

[82] B.C. Wilson, E.R. Cutler, and G.E. Fuchs. Effect of solidification parameters on the microstructures and properties of CMSX-10. *Materials Science and Engineering: A*, 479(1-2):356–364, apr 2008.

[83] Hong Bao Cui, Hai Yan Wang, Jin Yong Wang, and Heng Zhi Fu. Microstructure and microsegregation in directionally solidified FeCoNiCrAl high entropy alloy. *Advanced Materials Research*, 189-193:3840–3843, feb 2011.

[84] Gang Liu, Lin Liu, Xinwang Liu, Zhijun Wang, Zhenhua Han, Guojun Zhang, and A. Kostka. Microstructure and mechanical properties of al0.7cocrfeni high-entropy-alloy prepared by directional solidification. *Intermetallics*, 93:93–100, feb 2018.

[85] M. Feuerbacher, E. Würtz, A. Kovács, and C. Thomas. Single-crystal growth of a FeCoCrMnAl high-entropy alloy. *Materials Research Letters*, 5(2):128–134, sep 2016.

[86] Hiroyuki Y. Yasuda, Kyosuke Shigeno, and Takeshi Nagase. Dynamic strain aging of al 0.3 CoCrFeNi high entropy alloy single crystals. *Scripta Materialia*, 108:80–83, nov 2015.

[87] Bruce L. Bramfitt and Arlan O. Benscoter. Chapter 8 - the art of revealing microstructure. In *Metallographer's Guide*, pages 215–244. ASM International, 2002.

[88] Günter Gottstein. Atomic structure of solids. In *Physical Foundations of Materials Science*, pages 13–62. Springer Berlin Heidelberg, 2004.

[89] Joseph I. Goldstein, Dale E. Newbury, Joseph R. Michael, Nicholas W. M. Ritchie, John Henry J. Scott, and David C. Joy. Energy dispersive x-ray spectrometry: Physical principles and user-selected parameters. In *Scanning Electron Microscopy and X-Ray Microanalysis*, pages 209–234. Springer New York, nov 2017.

[90] C.G. Darwin. XCII. the reflexion of x-rays from imperfect crystals. *The London, Edinburgh, and Dublin Philosophical Magazine and Journal of Science*, 43(257):800–829, may 1922.

[91] Daniel Bellet. *Etude des textures des superalliages monocristallins par diffraction et diffusion des rayonnements: X,[gamma] et neutrons*. PhD thesis, Grenoble 1, 1990.

[92] Philipp Hallensleben, Felicitas Scholz, Pascal Thome, Helge Schaar, Ingo Steinbach, Gunther Eggeler, and Jan Frenzel. On crystal mosaicity in single crystal ni-based superalloys. *Crystals*, 9(3):149, mar 2019.

[93] Günter Bauer, Volker Güther, Hans Hess, Andreas Otto, Oskar Roidl, Heinz Roller, and Siegfried Sattelberger. Vanadium and vanadium compounds, jun 2000.

[94] Günter Gottstein. Mechanical properties. In *Physical Foundations of Materials Science*, pages 197–302. Springer Berlin Heidelberg, 2004.

[95] D. Hull and D.J. Bacon. Chapter 1 - defects in crystals. In D. Hull and D.J. Bacon, editors, *Introduction to Dislocations (Fifth Edition)*, pages 1–20. Butterworth-Heinemann, Oxford, fifth edition edition, 2011.

[96] G. B. Gibbs. The thermodynamics of creep deformation. *physica status solidi (b)*, 5(3):693–696, 1964.

[97] G. Schoeck. The activation energy of dislocation movement. *physica status solidi (b)*, 8(2):499–507, 1965.

[98] George H. Vineyard. Frequency factors and isotope effects in solid state rate processes. *Journal of Physics and Chemistry of Solids*, 3(1-2):121–127, jan 1957.

[99] A. V. Granato, K. Lücke, J. Schlipf, and L. J. Teutonico. Entropy factors for thermally activated unpinning of dislocations. *Journal of Applied Physics*, 35(9):2732–2745, sep 1964.

[100] Gerhard Adam and Otto Hittmair. *Wärmetheorie*. Vieweg+Teubner Verlag, 1988.

[101] G. B. Gibbs. The thermodynamics of thermally-activated dislocation glide. *physica status solidi (b)*, 10(2):507–512, 1965.

[102] G. Schoeck. Thermal activation in plastic deformation. In *Multiscale Phenomena in Plasticity: From Experiments to Phenomenology, Modelling and Materials Engineering*, pages 33–56. Springer Netherlands, 2000.

[103] KOCKS UF; ARGON AS; ASHBY MF. Thermodynamics and kinetics of slip. *PROGR. MATER. SCI.; G.B.; DA. 1975; VOL. 19; PP. (308 P.); BIBL. 5 P.; ISBN 0080179649*, 1975.

[104] A. G. Evans and R. D. Rawlings. The thermally activated deformation of crystalline materials. *physica status solidi (b)*, 34(1):9–31, 1969.

[105] J. P. Hirth and W. D. Nix. An analysis of the thermodynamics of dislocation glide. *physica status solidi (b)*, 35(1):177–188, 1969.

[106] A. S. Krausz and Henry. Eyring, editors. *Deformation kinetics*. Wiley, New York, 1975. "A Wiley-Interscience publication.".

[107] Bernhard Ilschner. *Hochtemperatur-Plastizität*. Springer Berlin Heidelberg, 1973.

[108] Jean-Paul Poirier. *Creep of Crystals*. Cambridge University Press, feb 1985.

[109] R.E. Smallman and A.H.W. Ngan. *Modern Physical Metallurgy*. Elsevier, 2014.

[110] P Rodriguez. Serrated plastic flow. *Bulletin of Materials Science*, 6(4):653–663, sep 1984.

[111] G. A. Malygin. Dynamic interaction of impurity atmospheres with moving dislocations during serrated flow. *Physica Status Solidi (a)*, 15(1):51–60, jan 1973.

[112] P.G. McCormick. Serrated yielding and the occurrence of strain gradients in an al-cu alloy. *Scripta Metallurgica*, 6(12):1133–1138, dec 1972.

[113] AW Sleeswijk. Dynamic strain ageing of alloys. *Acta metall*, 6:548, 1958.

[114] A. van den Beukel. Theory of the effect of dynamic strain aging on mechanical properties. *Physica Status Solidi (a)*, 30(1):197–206, jul 1975.

[115] S. L. Mannan and P. Rodriguez. Strain-ageing in disordered CuAu. *Philosophical Magazine*, 25(3):673–686, mar 1972.

[116] Samuel and Rodriguez. *Trans. Indian Inst. Metals*, 33:285, 1980.

[117] Samuel and Rodriguez. *Trans. Indian Inst. Metals*, 28:323, 1975.

[118] G.F Bolling and R.H Richman. Continual mechanical twinning: Part i: Formal description. *Acta Metallurgica*, 13(7):709–722, 1965.

[119] G.F. Bolling and R.H. Richman. Continual mechanical twinning: Part ii : Standard experiments. *Acta Metallurgica*, 13(7):723–743, 1965.

[120] G.F Bolling and R.H Richman. Continual mechanical twinning: Part iii: Nucleation and dislocation production part iv: Cyclic twinning in fe3be single crystals. *Acta Metallurgica*, 13(7):745–757, 1965.

[121] Ramachandran. Deformation - all aspects. In *Int. Conf. on Metal Sci., ICMS*, 1983.

[122] Ramachandran, Baldwin, and Reed-Hill. *Metallurgical Transactions*, 1:3011, jan 1970.

[123] L.P. Kubin, Ph. Spiesser, and Y. Estrin. Computer simulation of the low temperature instability of plastic flow. *Acta Metallurgica*, 30(2):385–394, feb 1982.

[124] V Seetharaman. Deformation and martensitic transformation. *Bulletin of Materials Science*, 6(4):703–716, sep 1984.

[125] J. Weertman. THEORY OF INFINITESIMAL DISLOCATIONS DISTRIBUTED ON a PLANE APPLIED TO DISCONTINUOUS YIELD PHENOMENA. *Canadian Journal of Physics*, 45(2):797–807, feb 1967.

[126] Y Estrin and LP Kubin. Collective dislocation behaviour in dilute alloys and the portevin—le chatelier effect. *Journal of the Mechanical Behavior of Materials*, 2(3-4):255–292, 1989.

[127] Sinisa Dj. Mesarovic. Dynamic strain aging and plastic instabilities. *Journal of the Mechanics and Physics of Solids*, 43(5):671–700, may 1995.

[128] P Penning. Mathematics of the portevin-le chatelier effect. *Acta Metallurgica*, 20(10):1169–1175, oct 1972.

[129] Egidio Rizzi and Peter Hähner. On the portevin–le chatelier effect. *International Journal of Plasticity*, 20(1):121–165, jan 2004.

[130] S. Tamimi, A. Andrade-Campos, and J. Pinho da Cruz. Modelling the portevin-le chatelier effects in aluminium alloys: a review. *Journal of the Mechanical Behavior of Materials*, 24(3-4):67–78, aug 2015.

[131] H. Ait-Amokhtar, P. Vacher, and S. Boudrahem. Kinematics fields and spatial activity of portevin–le chatelier bands using the digital image correlation method. *Acta Materialia*, 54(16):4365–4371, sep 2006.

[132] K. Chihab, Y. Estrin, L.P. Kubin, and J. Vergnol. The kinetics of the portevin-le chatelier bands in an al-5at%mg alloy. *Scripta Metallurgica*, 21(2):203–208, feb 1987.

[133] L.J Cuddy and W.C Leslie. Some aspects of serrated yielding in substitutional solid solutions of iron. *Acta Metallurgica*, 20(10):1157–1167, oct 1972.

[134] Yu Estrin and LP Kubin. Spatial coupling and propagative plastic instabilities. In *Continuum models for materials with microstructure*, pages 395–450. John Wiley & Sons, 1995.

[135] Huifeng Jiang, Qingchuan Zhang, Xuedong Chen, Zhongjia Chen, Zhenyu Jiang, Xiaoping Wu, and Jinghong Fan. Three types of portevin–le chatelier effects: Experiment and modelling. *Acta Materialia*, 55(7):2219–2228, apr 2007.

[136] M.A. Lebyodkin, N.P. Kobelev, Y. Bougherira, D. Entemeyer, C. Fressengeas, V.S. Gornakov, T.A. Lebedkina, and I.V. Shashkov. On the similarity of plastic flow processes during smooth and jerky flow: Statistical analysis. *Acta Materialia*, 60(9):3729–3740, may 2012.

[137] J. M. Robinson and M. P. Shaw. Microstructural and mechanical influences on dynamic strain aging phenomena. *International Materials Reviews*, 39(3):113–122, jan 1994.

[138] Ahmet Yilmaz. The portevin–le chatelier effect: a review of experimental findings. *Science and Technology of Advanced Materials*, 12(6):063001, dec 2011.

[139] D. A. Zhemchuzhnikova. *Influence of the extreme grain size reduction on plastic deformation instability in an AlMg and AlMgScZr alloys*. Theses, Université de Lorraine, December 2018.

[140] Youcef Bougherira, Denis Entemeyer, Claude Fressengeas, LEBEDKINA Tania, and Mikhail Lebyodkin. Caractérisation multi-échelles de l'hétérogénéité spatio-temporelle de l'effet portevin-le chatelier. 08 2009.

[141] M. A. Lebyodkin and T. A. Lebedkina. Multifractality and randomness in the unstable plastic flow near the lower strain-rate boundary of instability. *Physical Review E*, 77(2):026111, feb 2008.

[142] M. Feuerbacher. Private communication. 2019.

[143] R.W. Rohde and T.V. Nordstrom. On stress relaxation experiments. *Scripta Metallurgica*, 7(3):317–322, mar 1973.

[144] Z. Wu, H. Bei, G.M. Pharr, and E.P. George. Temperature dependence of the mechanical properties of equiatomic solid solution alloys with face-centered cubic crystal structures. *Acta Materialia*, 81:428–441, dec 2014.

[145] Hisashi Suzuki and Eiichi Kuramoto. Thermally activated glide in face-centered cubic alloys,. *Transactions of the Japan Institute of Metals*, 9:697–702, 1968.

[146] H. Traub, H. Neuhäuser, and Ch. Schwink. Investigations of the yield region of concentrated cu-ge and cu-zn single crystals—i. critical resolved shear stress, slip line formation and the true strain rate. *Acta Metallurgica*, 25(4):437–446, apr 1977.

[147] J. Friedel. *Dislocations*. Elsevier, 1964.

[148] R. J. Arsenault and S. Li. Computer simulation of thermally activated dislocation motion: Part III. in fcc solid solutions. *Metallurgical Transactions A*, 20(8):1429–1437, aug 1989.

[149] Z.S. Basinski, R.A. Foxall, and R. Pascual. Stress equivalence of solution hardening. *Scripta Metallurgica*, 6(9):807–814, sep 1972.

[150] Daniel Caillard. *Thermally Activated Mechanisms in Crystal Plasticity (Pergamon Materials Series)*. Elsevier Science, 2003.

[151] G. Laplanche, J. Bonneville, C. Varvenne, W.A. Curtin, and E.P. George. Thermal activation parameters of plastic flow reveal deformation mechanisms in the CrMnFeCoNi high-entropy alloy. *Acta Materialia*, 143:257–264, jan 2018.

[152] Jongun Moon, Sun Ig Hong, Jae Wung Bae, Min Ji Jang, Dami Yim, and Hyoung Seop Kim. On the strain rate-dependent deformation mechanism of CoCrFeMnNi high-entropy alloy at liquid nitrogen temperature. *Materials Research Letters*, 5(7):472–477, may 2017.

[153] Bruce Chalmers. *Physical Metallurgy*. John Wiley & Sons, Inc., 1959.

[154] J.P. HIRTH. DISLOCATIONS. In *Physical Metallurgy*, pages 1831–1875. Elsevier, 1996.

[155] Michael Feuerbacher. Mechanische Eigenschaften von ikosaedrischen Al-Pd-Mn-Quasikristallen. Technical Report Juel-3300, Jülich, 1996.

[156] Stefan Roitsch. Microstructural and macroscopic aspects of the plasticity of complex metallic alloys. 4281. Technical Report Juel-4281, Jülich, 2008. Record converted from JUWEL: 18.07.2013; Zugl.: Diss., RWTH Aachen, 2008.

[157] Daniel Caillard. Yield-stress anomalies and high-temperature mechanical properties of intermetallics and disordered alloys. *Materials Science and Engineering: A*, 319–321:74–83, December 2001.

[158] C. Gadelmeier, S. Haas, and U. Glatzel. Private communication. 2019.

[159] O. N. Senkov, J. M. Scott, S. V. Senkova, F. Meisenkothen, D. B. Miracle, and C. F. Woodward. Microstructure and elevated temperature properties of a refractory TaNbHfZrTi alloy. *Journal of Materials Science*, 47(9):4062–4074, jan 2012.

[160] Martina Luysberg, Marc Heggen, and Karsten Tillmann. FEI tecnai g2 f20. *Journal of large-scale research facilities JLSRF*, 2, jun 2016.

[161] David B. Williams and C. Barry Carter. *Transmission Electron Microscopy*. Springer US, 2009.

[162] D. Hull and D.J. Bacon. Chapter 2 - observation of dislocations. In D. Hull and D.J. Bacon, editors, *Introduction to Dislocations (Fifth Edition)*, pages 21–41. Butterworth-Heinemann, Oxford, fifth edition edition, 2011.

[163] R. K. Ham and N. G. Sharpe. A systematic error in the determination of dislocation densities in thin films. *Philosophical Magazine*, 6(69):1193–1194, sep 1961.

[164] S. Thoma and H. Cerva. The influence of non-linear interference processes on the HREM contrast of AlGaAs in ⟨100⟩ projection. *Ultramicroscopy*, 35(2):77–97, feb 1991.

[165] András Kovács, Roland Schierholz, and Karsten Tillmann. FEI titan g2 80-200 CREWLEY. *Journal of large-scale research facilities JLSRF*, 2, feb 2016.

[166] J.D Livingston. The density and distribution of dislocations in deformed copper crystals. *Acta Metallurgica*, 10(3):229–239, 1962.

[167] Peter P. Gillis and John J. Gilman. Dynamical dislocation theory of crystal plasticity. i. the yield stress. *Journal of Applied Physics*, 36(11):3370–3380, nov 1965.

[168] Peter P. Gillis and John J. Gilman. Dynamical dislocation theory of crystal plasticity. II. easy glide and strain hardening. *Journal of Applied Physics*, 36(11):3380–3386, nov 1965.

[169] Milton Ohring. 7 - mechanical behavior of solids. In Milton Ohring, editor, *Engineering Materials Science*, pages 299–V. Academic Press, San Diego, 1995.

[170] S.I. Rao, C. Varvenne, C. Woodward, T.A. Parthasarathy, D. Miracle, O.N. Senkov, and W.A. Curtin. Atomistic simulations of dislocations in a model BCC multicomponent concentrated solid solution alloy. *Acta Materialia*, 125:311–320, feb 2017.

[171] Baptiste Gault, Ann Chiaramonti, Oana Cojocaru-Mirédin, Patrick Stender, Renelle Dubosq, Christoph Freysoldt, Surendra Kumar Makineni, Tong Li, Michael Moody, and Julie M. Cairney. Atom probe tomography. *Nature Reviews Methods Primers*, 1(1), July 2021.

List of figures

List of tables

Schriften des Forschungszentrums Jülich
Reihe Information

Band / Volume 97
Hafnium oxide based memristive devices as functional elements of neuromorphic circuits
F. J. Cüppers (2023), vi, ii, 214 pp
ISBN: 978-3-95806-702-8

Band / Volume 98
Simulation and theory of large-scale cortical networks
A. van Meegen (2023), ca. 250 pp
ISBN: 978-3-95806-708-0

Band / Volume 99
Structure of two-dimensional multilayers and topological superconductors: surfactant mediated growth, intercalation, and doping
Y.-R. Lin (2023), x, 111 pp
ISBN: 978-3-95806-716-5

Band / Volume 100
Frequency mixing magnetic detection for characterization and multiplex detection of superparamagnetic nanoparticles
A. M. Pourshahidi (2023), X, 149 pp
ISBN: 978-3-95806-727-1

Band / Volume 101
Unveiling the relaxation dynamics of Ag/HfO2 based diffusive memristors for use in neuromorphic computing
S. A. Chekol (2023), x, 185 pp
ISBN: 978-3-95806-729-5

Band / Volume 102
Analysis and quantitative comparison of neural network dynamics on a neuron-wise and population level
R. Gutzen (2024), xii, 252 pp
ISBN: 978-3-95806-738-7

Band / Volume 103
3D Scaffolds with Integrated Electrodes for Neuronal Cell Culture
J. Abu Shihada (2024), vii, 163 pp
ISBN: 978-3-95806-756-1

Band / Volume 104
Advances in Photoemission Orbital Tomography
A. Haags (2024), ix, 254 pp
ISBN: 978-3-95806-766-0

Schriften des Forschungszentrums Jülich
Reihe Information

Band / Volume 105
Quantitative investigation of point defects and their dynamics in focused ion beam-prepared group III-nitride lamellas by off-axis electron holography
K. Ji (2024), 164 pp
ISBN: 978-3-95806-782-0

Band / Volume 106
NeuCoNS and Stacked-Net: Facilitating the Communication for Accelerated Neuroscientific Simulations
R. Kleijnen (2024), xx, 110, xxi-xxxiv pp
ISBN: 978-3-95806-788-2

Band / Volume 107
Construction of a Spiking Network Model of Macaque Primary Visual Cortex: Towards Digital Twins
A. Kurth (2024), xvi, 207 pp
ISBN: 978-3-95806-800-1

Band / Volume 108
Spin selectivity of chiral molecules on surfaces
M.R. Safari (2025), xiv, 165 pp
ISBN: 978-3-95806-810-0

Band / Volume 109
Redox-based Random Access Memory Arrays for Computing-In-Memory and Neuromorphic Computing
H. Chen (2025), x, 154 pp
ISBN: 978-3-95806-814-8

Band / Volume 110
Mechanics of deep neural networks beyond the Gaussian limit
K. Fischer (2025), xvi, 138 pp
ISBN: 978-3-95806-815-5

Band / Volume 111
Characteristics of plastically deformed *fcc* and *bcc* High-Entropy Alloys
T. Meenen (2025), x, 115 pp
ISBN: 978-3-95806-820-9

Weitere ***Schriften des Verlags im Forschungszentrum Jülich*** unter
http://wwwzb1.fz-juelich.de/verlagextern1/index.asp

Information
Band / Volume 111
ISBN 978-3-95806-820-9

Mitglied der Helmholtz-Gemeinschaft

JÜLICH
Forschungszentrum